Dissertation submitted to the

Combined Faculties of the Natural Sciences and Mathematics

of the Ruperto-Carola-University of Heidelberg. Germany

for the degree of

Doctor of Natural Sciences

Put forward by

Alexander Gelsin

born in: Rostov on Don, Russia

Oral examination: 10 June 2015

GALAXY CLUSTER DETECTION USING OPTIMAL MATCHED FILTERING IN OPTICAL BANDS

Referees:

Prof. Dr. Matthias Bartelmann

Prof. Dr. Joachim Wambsganß

ABSTRACT

The detection of galaxy clusters needs to be reliable and transparent in order to be relevant for cosmological purposes. In this work, a detection algorithm based on the optimal matched filtering technique is introduced and tested. For each of seven combinations of optical observables a filter type is constructed. Based on these filters signal-to-noise maps are computed on a redshift-mass grid. Given some signal-to-noise thresholds the expected detection completeness rates are computed for each filter type. It is concluded that the combination of all observables performs best. The completeness prediction for this filter choice is tested against numerical simulations. Because in this simulation field and cluster galaxies are produced separately also the contamination rate below 2 per square degree could be estimated. Completeness and purity rates for the detections are measured by relating detections to simulated clusters. The measured rates give insights into complications that can be within simulations and in the choice of limits and convolution scale of the filter. Lastly, the filter is applied to the W1m0p1 field from CARS. Resulting detections are reduced to 31 by merging. 15 Detections can be related to detections from literature. It can hence be concluded that the filter may be applied to data.

ZUSAMMENFASSUNG

Um kosmologischen Ansprüchen zu genügen, müssen Detektionen von Galaxienhaufen zuverlässig und durchsichtig sein. In dieser Arbeit wird ein Detektionsverfahren vorgestellt und getestet, das auf optimal angepasster Filtertechnik basiert. Für sieben Kombinationen aus optischen Beobachtungsgrößen werden sieben Filter konstruiert. Basierend auf diesen Filtern werden auf einem Rotverschiebungs- und Massegitter erwartete Signal-zu-Rauschen Verhältnisse berechnet. Anhand von gegebenen Signal-zu- Rauschen Verhältnisgrenzen werden erwartete Vollständigkeitsraten der Detektionen für alle Filtertypen berechnet. Es wird gefolgert, dass die Kombination aus allen Beobachtungsgrößen die beste Wahl ist. Die Vorhersage der Vollständigkeitsrate für diesen Filtertyp wird anhand von synthetischen Daten getestet. Weil bei der Herstellung der synthetischen Daten Feld- und Haufengalaxien separiert produziert werden, kann auch die Verschmutzungsrate, die unter 2 pro Quadratgrad liegt, abgeschätzt werden. Indem Detektionen und Galaxienhaufen in Verbindung gebracht werden, werden die Vollständigkeits- und Reinheitsraten der Detektionen gemessen. Die gemessenen Raten liefern Einblicke in die Komplikationen, die in den synthetischen Daten und in den Begrenzungen und Faltungsskalen des gewählten Filters liegen können. Letztlich wird der Filter auf den W1m0p1 Ausschnitt von CARS angewandt. Die resultierenden Detektionen werden durch Verschmelzung zu 31 reduziert. 15 Detektionen kÃ¶nnen in Verbindung mit Detektionen in der Literatur gebracht werden. Daraus wird gefolgert, dass der Filter auf Daten angewandt werden kann.

CONTENTS

LIST OF FIGURES

LIST OF TABLES

INTRODUCTION

MODERN COSMOLOGY

The beginning of modern cosmology is commonly dated back to the 1920th, when Slipher (1927) and Hubble (1929) discovered that and Lemaître (1927) explained why the escape velocity of galaxies increases with distance. Due to Lemaître, the idea of an initial state of the Universe, today known as the Big Bang from which it started expanding was born. Einsteins general theory of relativity (Einstein, 1916) was essential to relate the observation to the explanation by Lemaitre.

Only few years later another striking discovery, namely that of dark matter (Zwicky, 1933) entered modern cosmology. The missing mass problem in the context of galaxy movement in virialized clusters was confirmed also from the rotational curve of the Andromeda galaxy in Babcock (1939). The mass–to–light ratio in the Universe today is known to be larger than unity. Since then, one of many quests in cosmology is to find and explain dark matter.

These and more informations helped to create a standard model in cosmology, named ΛCDM. The most important features thereof are noted in Chapter 1. A strong confirmation for this model is the existence of the cosmic microwave background (Penzias and Wilson, 1965). With a black body spectrum of 2.72548 ± 0.00057 K (Fixsen, 2009) and is nearly uniform. It was also predicted in Gamow (1952) who also made strong contributions to the understanding of the primordial nucleosynthesis. Today, the baryonic matter contribution to energy density in the Universe is mostly understood.

Since the accelerated expansion of the Universe was confirmed by Riess et al. (1998) an energy density that does not correspond to matter nor curvature raised attention. This energy density was named dark energy and the most prominent theories consider it to be either the cosmological constant Λ or a space–time dependent scalar field (see Peebles and Ratra, 2003).

Stronger restrictions on theories can be put by measurements of the energy densities in form of cosmological parameters. An important role hereby play clusters of galaxies. These objects host the most mass in the Universe and their number counts can be related to cosmological models (see also Sec. 1.2). Surveys such as CFHTLS[1], Dark Energy Survey[2] (DES) and Euclid[3] have been and will be started to further investigate dark energy. These surveys are related to observations of the Universe in the optical bands and hence enable detections of galaxy clusters in the observed data. In principle, clusters of galaxies can also be searched for in X-ray and microwave data as explained in Section 1.4. In this work, however, the focus will be on optical data.

OBJECT DETECTION

The idea of finding objects in data (that also contains noise) is closely related to filtering. The variety of sought objects requires filters that are broad enough to capture the majority of these objects. At the same time, broad filters also increase the amount of spurious

---

[1] http://www.cfht.hawaii.edu/Science/CFHTLS/

[2] http://www.darkenergysurvey.org/

[3] http://www.euclid-ec.org/

detections. If the filter is narrowed down, however, not only the contamination but also the completeness decrease.

- Completeness (in %) answers the question of how many of all real objects in the defined survey limits can be associated with detections. This definition implies that one detection can in principle cover several objects.
- Purity (in %) answers the question of how many of all candidate detections can be associated with real objects. Hereby, the possibility of many detections be associated with the same real object is not excluded. As consequence, contamination is purity subtracted from 100%.

For cosmological interpretations, high completeness and low contamination are both needed. High completeness can be achieved by matching the filtering function to average properties of sought objects. To reduce false–positive detections the filter can be constructed to down weight data points that follow the statistics of the noise. Such a filter is can be found in Maturi et al. (2005).

As this work focuses on detections of galaxy clusters in optical bands, the optical optimal matched filter for clusters of galaxies is constructed to fit into the framework of Maturi et al. (2005), Pace et al. (2008), Bellagamba et al. (2011), Gelsin (2011). Some detection algorithms that work on optical data are gathered in Section 1.5.

AIMS WITHIN THIS THESIS

- A filter function in optical bands that has a clear connection to mass and redshift of the hosting halo shall be defined.
- Its functionality in terms of the weighting function shall be investigated.
- Theoretical predictions for signal-to-noise maps shall be made.
- These predictions need to be tested against numerical simulations.
- As a first test on real data, it shall be applied to the W1m0p1 field from CARS.

STRUCTURE OF THE THESIS

In Chapter 1 the standard cosmological model is introduced and briefly explained. Distance measurements (Sec. 1.1), the idea of the mass–function (Sec. 1.2) and galaxy clusters (Sec.1.4) are premises for the construction of the filter and theoretical predictions thereof. Some existent detection algorithms are gathered in Section 1.5. In Chapter 2 the data that is used throughout this thesis is introduced. Chapter 3 deals with the construction of the galaxy number density model in clusters of galaxies. Of particular importance are the distribution functions in Sections 3.4, 3.5, 3.6 and 3.7. The noise enters the filter function through the field number density introduced in Chapter 4. Two approaches for the field galaxy distribution model are followed in this thesis. The first (Sec. 4.1), assumes an a priori number density model that serves the purpose to understand filter properties. The second model is directly estimated from the data (Sec. 4.2). The goodness of the second is assessed in Section 4.3. The optimal matched filter is introduced in Chapter 5. Technical details such as numerical stability and volume limits of the filter can be found in Sections 5.5 and 5.3 respectively. Thereafter, in Section 5.6 seven example filters are constructed and their weighting functions reviewed. The filter is tested against numerical simulations in Chapter 8. Therefor synthetic data is constructed in Chapter 6. Cluster galaxies and field galaxies are created according to Sections 6.2 and 6.3 respectively. Section 6.1 addresses creation of dark matter halos. In Chapter 7, signal to noise maps are predicted for a Gaussian distribution of field galaxies (in the optical observables) in Section 7.1 and for the estimated field galaxy distribution from the selected CARS catalog in Section 7.2. The most promising filter is then applied to simulations (Ch. 8) and to the selected CARS catalog (Ch. 9). A summary and conclusion can then be found the last part iii.

1

COSMOLOGICAL AND ASTROPHYSICAL CONTEXT

This Chapter discusses aspects closely related to the detection algorithm for galaxy clusters. These aspects are the standard model of cosmology on which the distance measurements and structure formation depend. The theory of structure formation itself impacts the cluster model and the mass–function which will be used to perform simulations and predict detections.

1.1 COSMOLOGY AND DISTANCE DEFINITIONS

The standard model of modern cosmology assumes spatial *isotropy* and *homogeneity* in the universe, when averaged over scales of larger than 100 Mpc. These assumptions constitute the so called *cosmological principle*. The first assumption states, that no direction in the universe is preferred. This has been confirmed through measurements of the spatial galaxy distribution as described in Hogg et al. (2005), Scrimgeour et al. (2012) and of the cosmic microwave background radiation (CMB) measured by the Planck Collaboration et al. (2014) (and references therein). Homogeneity is prevailed if no position in the universe is preferred to others. Testing it requires three dimensional data that is valid for a particular time. As stated in Redlich et al. (2014) and references therein, is the confirmation of spatial homogeneity is therefore difficult to be achieved. A metric that combined these two assumptions has been proposed by Friedmann (1922, 1924). Together with the independent work on expanding or contracting universe models of Lemaître (1927), Robertson (1935) and Walker (1937) it led to the FLRW-metric:

$$ds^2 = c^2\,dt^2 - a^2(t)\left[d\omega^2 + f_K^2(\omega)d\Omega^2\right]. \tag{1}$$

Here $a(t)$ is the scale parameter that scales space with time, ω is the radial coordinate and $d\Omega$ the differential solid angle. The scaling of the differential solid angle depends on a function $f_K^2(\omega)$ which depends on the curvature of space K. Three cases can be distinguished, as spatial curvature can be positive (closed universe), zero (flat universe) or negative (open universe):

$$f_K(\omega) = \begin{cases} K^{-1/2}\sin\left(K^{1/2}\omega\right) & (K > 1) \\ \omega & (K = 0) \\ |K|^{-1/2}\sinh\left(|K|^{1/2}\omega\right) & (K < 1). \end{cases} \tag{2}$$

The FLRW–metric together with an ideal fluid energy–momentum tensor can be inserted into the Einsteins field equations,

$$R_{\mu\nu} - g_{\mu\nu}\frac{R}{2} + g_{\mu\nu}\Lambda = \frac{8\pi G}{c^4}T_{\mu\nu} \tag{3}$$

which yield the Friedmann equations describing the dynamics of the universe in terms of the scale parameter:

$$\left(\frac{\dot{a}}{a}\right)^2 = \frac{8\pi G}{3}\rho - \frac{Kc^2}{a^2} + \frac{\Lambda}{3} \tag{4}$$

$$\frac{\ddot{a}}{a} = -\frac{4\pi G}{3}\left(\rho - \frac{3p}{c^2}\right) + \frac{\Lambda}{3} \tag{5}$$

Two contributions to energy–density can be distinguished relativistic (radiation) and non–relativistic (matter) particles. These contributions can be evaluated through the second Friedmann equation these contributions can be evaluated: $\rho_r \sim a^{-4}$ and $\rho_m \sim a^{-3}$, implying different behavior for different epochs. For convenience the Friedmann Equation can be re parametrized yielding the Hubble function:

$$H^2(t) = H_0^2\left(\Omega_r a^{-4} + \Omega_m a^{-3} + \Omega_K a^{-2} + \Omega_\Lambda\right). \tag{6}$$

The parameters $\Omega_m = \frac{\rho_m^0}{\rho_{cr}}$, $\Omega_r = \frac{\rho_r^0}{\rho_{cr}}$, $\Omega_K = \frac{Kc^2}{H_0^2}$ and $\Omega_\Lambda = \frac{\Lambda}{3H_0^2}$. Are the dimensionless radiation, matter, curvature and cosmological constant energy–densities at present date, where $\rho_{cr} = \frac{8\pi G}{3H_0^2}$. The Hubble constant H_0 is for convenience converted into the Hubble parameter h, following the relation $H_0 = h \cdot 100\,\mathrm{km\,s^{-1}\,Mpc^{-1}}$.

Distances

The Hubble function describes the dynamics of the universe in terms of the scale parameter. Distances, on large scales will be affected by the Hubble flow, as space might stretch or contract with time. The distance covered by a photon emitted and observed at times t_e and t_o, respectively is related to scale parameters $a(t_e)$ and $a(t_o)$ and therefore to the redshifts z_e and z_o, respectively. For observations, three distance measures are of particular relevance:

- *Proper distance;* D_{prop} : it is defined as the photons traveled distance from emission to observation points, equivalently during the redshift change from z_e to z_o:

$$D_{prop}(z_o, z_e) = c\int_{t_e}^{t_o} dt = c\int_{a(z_e)}^{a(z_o)} \frac{da}{\dot{a}} = c\int_{a_e}^{a_o} \frac{da}{aH(a)} \tag{7}$$

- *Comoving distance;* $\omega(z_e, z_o)$: it is the distance between the source and observer in comoving coordinates. Meaning, that the distance is rescaled by the scale parameter, such that world lines of the emission and of an observer are (co–) moving with the cosmic flow:

$$\omega(z_o, z_e) = c\int_{t_e}^{t_o} \frac{dt}{a} = \frac{c}{H_0}\int_{a(z_e)}^{a(z_o)} \frac{da}{a^2 E(a)}. \tag{8}$$

- *Angular diameter distance;* D_A: it relates the observed angular sizes of one object to its distance from the observer. As in Euclidean flat space, it is related to the differential solid angle $\delta\Omega$ measured for the observed surface area δA. Here the relation is given by the metric in terms of:

$$D_A(z_o, z_e) = \sqrt{\frac{\delta A}{\delta\Omega}} = \frac{a_e}{a_o} f_K(\omega(z_o, z_e)). \tag{9}$$

- *Luminosity distance;* D_L: it is based on the relation between intrinsic and observed luminosity of an object. Taking into account the redshift of photons, the relative stretching of space and the dilution of luminosity in the surface area, an additional factor of $\left(\frac{a_e}{a_o}\right)^4$ enters the luminosity–flux relation and hence the D_L–D_A relation, such that

$$D_L(z_o, z_e) = \left(\frac{a(z_e)}{a(z_o)}\right)^2 D_A(z_o, z_e) \tag{10}$$

Particularly *angular diameter distance* and *luminosity distance* are of significant importance, when dealing with distant, extended and light emitting sources such as galaxy clusters.

1.2 STRUCTURE FORMATION AND MASS-FUNCTION

The cosmological principle holds for large scales. On smaller scales however, structures such as clusters of galaxies, galaxies, stars, planets etc. break the homogeneity. These structures span roughly 30 orders of magnitude in size. It is generally believed that each structure in the universe originates from initial energy–density fluctuations, that must have existed as the universe started expanding. During expansion, dark–matter which only interacts through gravity gravitationally clumped around these fluctuations forming over densities which then evolved to the cosmic web. This web hosts and connects the afore mentioned structures like galaxies and clusters of galaxies. A rigorous treatment of inhomogeneities requires the framework of general relativity, but the problem can be simplified by using Newtonian gravity to describe the matter density on top of an expanding universe described by the Friedmann equations. The quantity investigated with this approach is the matter density contrast δ. It describes the matter density fluctuations of dark– and baryonic–matter witch respect to the mean matter–density of the universe. The statistical properties of the density contrast are, in the linear regime captured by the power spectrum $P(k)$ which is defined by the following relation:

$$\langle\hat{\delta}(k)\hat{\delta}^{\dagger}(k')\rangle = (2\pi)^3\,\delta^D(k-k')\,P(k). \tag{11}$$

The variance of the density contrast filtered on a specific scale R is given by:

$$\sigma_R^2 = 4\pi \int \frac{k^2\,dk}{(2\pi)^3} P(k)\hat{W}_R^2(k), \tag{12}$$

here $\hat{W}$ is the Fourier transformed window function that allows the contributions to the density contrast that are within a radius R. The scale that is commonly used for this filtering is $R = 8$ Mpc h^{-1}. The standard deviation σ_8 thus contains information about the amplitude of the power spectrum. In particular it sets the normalization of the power spectrum and is therefore of big importance for cosmological considerations.

The density contrast undergoes both linear and non linear growth during the evolution of the universe. As δ reaches unity, the linear perturbation theory breaks down and another approach has to be used.

Mass–Function

It is possible to use the collapse model to describe describe what happens to regions where the density contrast exceeds a certain threshold. This collapse model describes how an over density embedded into a homogeneous but expanding background universe collapses to highly non–linear structures that are called halos. Usually the spherical collapse model where all axis are equal, can be used. The main quantities characterizing this model are the critical linear density contrast $\delta_c = 1.69$ and the virialized over density $\Delta_v \sim 178$. These values only weakly depend on cosmology and set the density contrast for which the halos can be regarded as collapsed and virialized. Angrick and Bartelmann (2010) adopt the triaxial model, where the axis collapse at different times for the virialization. The deviation of δ_c and Δ_v from those in the spherical collapse model is on $20-50$ % level, this is also due to higher mass and redshift dependence. For each mass of a halo with a fixed density ρ_{fix}, it can be assigned a radius that defines the volume hosting the homogeneously distributed mass. The mass dependent scale R(M) can now be used for the density contrast computations. In particular the variance of the underlying Gaussian matter density field filtered on the scale R(M) is also mass dependent. The scaling of linear power spectrum P(k) with redshift allows to separate $\sigma_{R(M)}(z)$ into the standard deviation today ($\sigma_{R(M)}$), measured on the scale R times the linear growth function $D_+(z)$. In the Press and Schechter (1974) formalism, the finding of collapsed halo with $\delta > \delta_c$ for the Gaussian random field δ is given by the complementary error function:

$$P(\delta > \delta_c, z) = \int_{\delta_c}^{\infty} p(\delta(z)) d\delta = \frac{1}{2} \operatorname{erfc}\left(\frac{\delta_c}{\sqrt{2}\sigma_{R(M)}(z)}\right) \tag{13}$$

with $p(\delta(z)) = \frac{1}{\sqrt{2\pi\sigma^2_{R(M)}(z)}} \exp\left(-\frac{\delta(z)^2}{2\sigma^2_{R(M)}(z)}\right)$, being the probability to find a halo with density contrast $\delta(z)$ convolved on the scale R. This equation implies a mass dependency through R(M) such that the differential comoving number density of halos exceeding the mass M at the redshift z is given as:

$$n(M,z) = \frac{1}{V_M} \frac{d\sigma_{R(M)}}{dM} \frac{\partial P(\delta > \delta_c, z)}{\partial \sigma_{R(M)}} \tag{14}$$

$$= \sqrt{\frac{2}{\pi}} \frac{\rho_{cr}}{M} \frac{\delta_c(z)}{D_+(z)\sigma_{R(M)}} \frac{d\sigma_{R(M)}}{dM} \exp\left(-\frac{\delta_c^2}{2\sigma^2_{R(M)}(z)}\right). \tag{15}$$

The mass–function is a powerful tool to probe cosmology by investigating the predicted and measured halo number counts, and has been widely discussed and investigated in the literature Sheth and Tormen (1999), Angrick and Bartelmann (2010), Jenkins et al. (2001), Tinker et al. (2008).

1.3 ADOPTED COSMOLOGICAL PARAMETERS

The most recent cosmological parameters measured by WMAP and PLACK satellites, combined with other studies such as BAOs, weak gravitational lensing etc., are shown in Table 1. The constraints underlying the determination of these parameters can be found in Komatsu et al. (2011), Hinshaw et al. (2013) and Planck Collaboration et al. (2014), in order of their appearance in the table. In this thesis the older parameters by Komatsu et al. (2011) are used for cosmological computations, to allow for comparisons with older work.

Table 1: Summary of most recent parameter constraints from WMAP7, WMAP9 and PLANCK data. The values are taken from Komatsu et al. (2011) Table 1, Hinshaw et al. (2013) Table 9 and Planck Collaboration et al. (2014) Table 2.

Parameter	WMAP7	WMAP9	PLANCK
h	$0.700^{+0.040}_{-0.030}$	0.690 ± 0.010	0.673 ± 0.012
Ω_m	0.300 ± 0.040	0.290 ± 0.010	0.315 ± 0.016
Ω_B	0.047 ± 0.006	0.046 ± 0.001	0.048 ± 0.000
Ω_Λ	0.700 ± 0.040	0.717 ± 0.001	0.685 ± 0.002
σ_8	0.816 ± 0.024	0.770 ± 0.038	0.829 ± 0.012

1.4 GALAXY CLUSTERS

As explained in previous Sections (dark–) matter halos are identified with collapsed over density peaks. Galaxy clusters are the largest of those. To some degree clusters of galaxies are described as virialized structures, because their over density is assumed to be larger than Δ_v i. e. the scale for which collapsed objects are in virial equilibrium. Assuming the over density of exactly 200 times the critical density in the cluster, the virial radius r_{vir} can simply be relabeled as R_{200}. Virial mass and radius follow the relation:

$$R_{200} = \left(\frac{G\, M_{200}}{100\, H^2(z)} \right)^{\frac{1}{3}}, \tag{16}$$

with $H(z)$ being the Hubble function, describing the evolution of the expansion rate in a FLRW–cosmology. Further assertion of the virial equilibrium yields the relation between velocity dispersion which is the observed peculiar motion of galaxies in a cluster, the virial mass and the redshift of the collapsed object:

$$\sigma_v = \sqrt{\frac{G\, M_{200}}{3\, R_{200}}} \tag{17}$$

The characteristic velocity dispersion inside a cluster imposes a shift in the frequency spectrum of the light emitting galaxies. This redshift can be used as an initial guess for the internal width of a galaxy cluster in redshift. Historically, galaxy clusters are what their name suggests, not only matter but also galaxy over densities of the mean field. Their galactic content is only one feature. Today, their intra cluster hot gas and gravitational potential are used to detect and characterize them. A large range of wavelength connects observables to physical properties within these huge objects. X-rays reveal bremsstrahlung from cluster cores and therefore inter cluster physics. Microwaves carry cluster information imprinted on the temperature fluctuations as introduced in Sunyaev and Zeldovich (1981) and can also be used for detection. In the optical bands it is possible to take advantage of weak gravitational lensing, visible as the distortion of background sources by a foreground gravitational potential, strong gravitational lensing which creates highly distorted images around the Einstein radius associated with the gravitational potential of clusters. Also color and luminosity signatures of the characteristic galaxy populations in the cluster can be used to characterize them. These information do not only allow and help to detect clusters but also provide important probes for astrophysics and cosmology. In this thesis, the focus is on the detection of galaxy clusters and on definition of a clear selection function to allow cosmological studies.

1.5 EXISTING GALAXY CLUSTER DETECTION ALGORITHMS IN OPTICAL BANDS

By means of a selected list of existent methods to detect cluster of galaxies some informations regarding common aspects of cluster detection are gathered and briefly presented. By no means is the list of methods meant to be complete, nor is a rigorous summary of the selected articles given. It rather serves as a starting point for those who are interested in cluster detection via galaxy over densities. For a historical context of optical cluster detections, the interested reader is referred to Gal (2008). For a more recent overview over the de projection methods in optical cluster detections, the reader is referred to Hao et al. (2010) and Hao (2009).

The first detections of nearby galaxy clusters were made by studying photographic plates. Present day surveys perform multi band observations of the sky. Therefore information different bands, colors and photometric redshift can be provided by these surveys. Detection algorithms have different ways to use some or all of these information in the data to make detections. In Figure 1 an overview over the selected articles and their relation to observables that are used is given. Mostly magnitude information is considered. Magnitude filters have already been used by Abell et al. (1989) to define the richness. There, the filter is a simple Heaviside–step function that cut off all galaxies above a certain magnitude.

Using photometric redshift information in addition to the angular distribution of galaxies around a center would make a three dimensional filter. Redshift serves as the powerful de projection tool which enables to distinct galaxies clustered along the line of sight. However, it is a very powerful tool only, as long as the redshift data is reliable, which is true for spectroscopic measurements. Typical 1–σ errors on photometric redshift are of order $0.05(1+z)$. Precise measurements are therefore not possible in this case. Nevertheless, are photometric redshift filters used in literature. For example are Eisenhardt et al. (2008) using redshift probability distributions (based on photometric redshift estimation) for each galaxy to weight redshift slices on which galaxy cluster are sought after convolving the galaxy map with a smoothing kernel.

Color filters are becoming more common for de projection of galaxy clusters along the line of sight. As will be explained in Chapter 3, Section 3.1 this is because clusters are observed to have a red color sequence which is characteristic for the clusters redshift. To observe the red color sequence proper bands to cover the specific redshift ranges need to be considered (.see also Sec. 3.1).

The most recent and progressive optical galaxy cluster finders in the literature are listed chronologically.

a) Postman et al. (1996)
b) Gladders and Yee (2000)
c) Goto et al. (2002) – CE
d) Mazure et al. (2007)
e) Koester et al. (2007b) – maxBCG
f) Dong et al. (2008)
g) Eisenhardt et al. (2008)
h) Rozo et al. (2009)
i) Hao et al. (2010) – GMBCG
j) Rykoff et al. (2012)
k) Bellagamba et al. (2011)
l) Ascaso et al. (2012)
m) Rykoff et al. (2014) – RedMaPPer
n) Oguri (2014) – CAMIRA

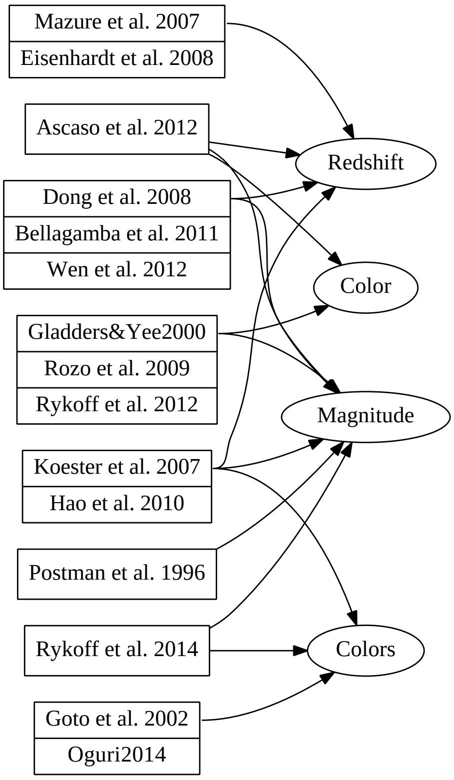

Figure 1: Optical observables used in literature.

The cluster detection in optical bands can therefore be separated into two tasks. Both the de projection along the line of sight and identification of clustered regions in this plane are very important. The algorithms have in common that either galaxies or cells in the field are weighted. The complexity of weighting differs from simple Heaviside to complex likelihood like functions.

Optical galaxy cluster detections are usually quantified by the richness of the detection. This richness is not always equal to the number of galaxies in a certain volume but can be the sum of non trivial weights. In Rykoff et al. (2014) a list of requirements has been proposed that each galaxy cluster finder must fulfill in order to be useful for cosmological purposes. Amongst these, the scatter in the richness–mass relation needs to be minimal. A good estimation of richness scatter and clear connection to mass are therefore desirable.

The significance of detections has also to be estimated in a clear way. This allows to comprehend the selection that shall be made for specific research purposes.

2

DATA FROM THE CFHT: CARS

The following is a summary of the CFHTLS- Archive Research Survey (hereafter CARS, see Erben et al. (2009) & Hildebrandt et al. (2012)). The Canadian French Hawaii Telescope Legacy Survey [1] (CFHTLS) is a survey covering 172 deg^2 of the sky. The aim of CARS is to provide astronomers with reliable multi-color catalogs for 37 deg^2 extracted from images taken with the Megaprime instrument [2] and make it publically accessible through the Canadian Astronomy Data Centre (CADC [3]). With reliable photometry, redshift can be estimated using the Bayesian Photometric Redshifts method Benítez (2000). The fact that some of the CARS patches overlap with other surveys (VVDS, DEEP2 and SDSS) with spectroscopic information allows to train the parameters for the spectral energy distribution fitting the observed magnitudes. Using one field to calibrate the photo-z measurements allows the measurements of photo-z's on the other fields. Erben et al. (2009) finds that the photometric redshifts are biased in the redshift range from zero to unity. This is further investigated in Hildebrandt et al. (2012). The CARS survey consists of three (W1,W3,W4) patches of 21, 5 and 11 deg^2 fields, respectively. Each patch is split into one deg^2 fields which are labeled after the main patch and the one degree shifts within right ascension and declination with respect to the center of the main patch. For example, W1m0p1 means that its centered on the W1 patch (RA = 34.5 deg, DEC = -7 deg) minus 0 deg in RA and plus 1 deg in DEC. For this work, the W1m0p1 field is randomly selected to provide a distribution of field galaxies and test the filter that which is going to be introduced in the following Chapters. The related catalog contains 171277 objects prior the selection that has been performed as follows. First, objects which are most likely to be galaxies, CLASS_STAR $<$ 0.95 are kept. This reduces the number of objects down to 164064. All objects that lie in masked regions, MASK = 1 are removed in a subsequent step. This leaves 132924 unmasked galaxies in the catalog. The most crucial step is to remove galaxies with unreliable photometric redshifts, with ODDS $\geqslant$ 0.9. The ODDS parameter gives the probability for the object's redshift to fall within a previously defined interval and quantifies the characteristic concentration of each galaxy's redshift probability distribution. This steps leaves 57159 unmasked galaxies with reliable photometric redshifts in the catalog. Although the suggested redshift range in Erben et al. (2009) is $0 \leqslant z \leqslant 1.4$, the last cut of the catalog is performed for the redshifts above 2. No specific reason is behind this selection, but the cut at 1.4 would remove only 100 more galaxies. Hence, the final catalog contains 51237 galaxies. For this W1m0p1 catalog, the

---

[1] Based on observations obtained with MegaPrime/MegaCam, a joint project of CFHT and CEA/IRFU, at the Canada-France-Hawaii Telescope (CFHT) which is operated by the National Research Council (NRC) of Canada, the Institut National des Science de l'Univers of the Centre National de la Recherche Scientifique (CNRS) of France, and the University of Hawaii. This work is based in part on data products produced at Terapix available at the Canadian Astronomy Data Centre as part of the Canada-France-Hawaii Telescope Legacy Survey, a collaborative project of NRC and CNRS.

[2] The Megaprime instrument uses 4×9 CCDs, covering 2048×4096 pixel each. The combined resolution correponds to an approximate 1×1 deg^2 field of view (fov)

[3] http://www4.cadc-ccda.hia-iha.nrc-cnrc.gc.ca/

Table 2: Mean values for redshift, magnitudes m_g, m_r, m_i and m_z and the related colors c_{g-r}, c_{r-i} and c_{i-z}.in the CARS W1mop1 patch data.

$\bar{z}$	$\bar{m}_g$	$\bar{m}_r$	$\bar{m}_i$	$\bar{m}_z$	$\bar{c}_{g-r}$	$\bar{c}_{r-i}$	$\bar{c}_{i-z}$
0.6508	24.2989	23.6488	22.9583	22.7807	0.6501	0.6904	0.1776

means and covariances of the observables are computed and shown in Tables 2 and 3 respectively. Lastly, the photometric redshift error is classified, as it enters the filter function. For this purpose, the $1-\sigma$ interval of the photo-z distributions is averaged over all galaxies, dividing out their estimated redshift. $\sigma_z = \frac{1}{N}\sum_{i=0}^{N} \frac{\sigma_{z,i}}{(1+z_{\text{est},i})} = 0.076.$

Table 3: Covariances in the CARS W1mop1 selection data. Using redshift, magnitudes m_g, m_r, m_i and m_z and the related colors c_{g-r}, c_{r-i} and c_{i-z}.

	z	m_g	m_r	m_i	m_z	c_{g-r}	c_{r-i}	c_{i-z}
z	0.0372	0.1126	0.1411	0.1107	0.0919	-0.0285	0.0304	0.0187
g		1.6032	1.6560	1.5332	1.5673	-0.0528	0.1228	-0.0340
r			1.8565	1.7328	1.7874	-0.2005	0.1237	-0.0546
i				1.7034	1.7706	-0.1995	0.02934	-0.0672
z					1.9676	-0.2201	0.0167	-0.1969
c_{g-r}						0.1477	-0.0093	0.0205
c_{r-i}							0.0944	0.0125
c_{i-z}								0.1297

The distributions in magnitudes and redshifts for the CARS selection are shown in Figures 2 and 3 respectively.

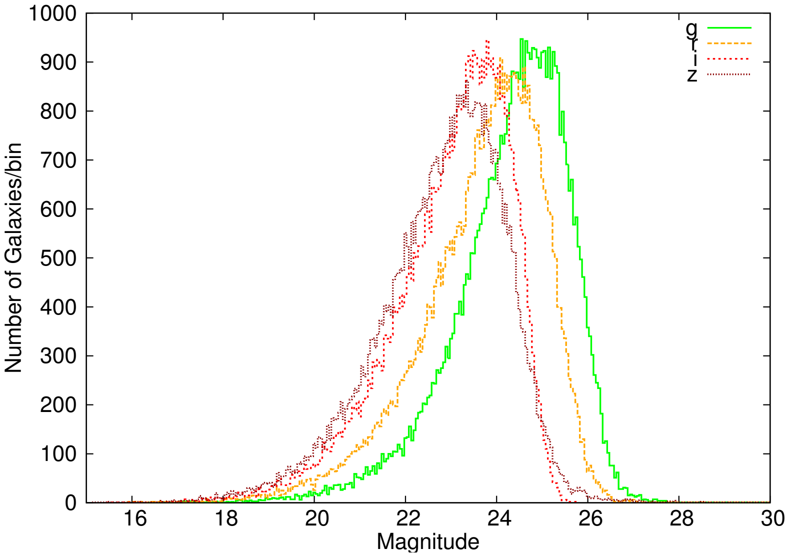

Figure 2: Magnitude distributions in g,r,i and z bands for the selection (see text) from W1m0p1 CARS field.

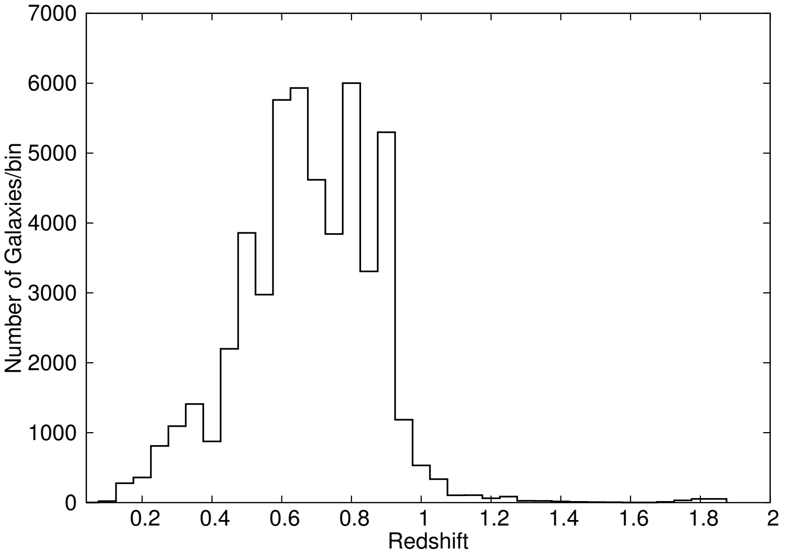

Figure 3: Redshift distribution of the selected galaxies (see text) from W1m0p1 CARS field.

Part I

CONSTRUCTION OF THE FILTER

3

MODEL FOR CLUSTER GALAXIES IN OPTICAL BANDS

In this Chapter the model developed in Bellagamba (2012) and Gelsin (2011) is refined in terms of normalizations, accuracy and numerical implementation. Also explanations justifying the model are provided within this thesis. Therefore, the cluster characteristics used in other studies are addressed. They build the ground for the model. Then, distribution functions based on these characteristics are created and finally combined into a number density function that enters the filter function introduced in Chapter 5. Limits and therefore the normalization of the distribution functions are explicitly addressed.

3.1 COLOR BI–MODALITY AND RED SEQUENCE

Color bi–modality can rather be interpreted as bi–modality of galaxy types within galaxy clusters. Butcher and Oemler (1978) first discovered that the fraction of spiral (blue) galaxies in clusters increases with redshift. In other words, at low redshifts there are mostly ellipticals in galaxy clusters. The color bi–modality itself is described in Balogh et al. (2004). These findings support the split into two types of galaxies based on their star–formation, which is most likely represented by the color of galaxies. Red are early–type galaxies. They can be found in lower redshift i. e. old galaxy clusters, as they undergo only passive star–formation and evolution. Blue are late–type galaxies, that undergo active and sometimes violent star formation and are most likely found in the mean field or in very young (high redshift) clusters. It is a very important information that helps to guess the redshift and with it the age and the distance of a galaxy cluster. The relation between morphological galaxy types and environment has been initially investigated in Dressler (1980) and yet it is not fully explored. In general, red galaxies seem to be mostly found in the densest regions of the universe. Such regions are identified with most massive and oldest galaxy clusters. To recover the relation between age of an elliptical or S0 galaxy and its color Bruzual and Charlot (2003) constructed a synthetic model that describes the relationship quite well. The clustering of galaxies in color around a characteristic color sequence, which lastly can be identified with a clustering in space is called red–sequence. It has been used extensively to identify galaxy clusters, as can be seen in Section 1.5. In the following, some recent studies are used to quantify the previous qualitative findings in terms of numeric scaling relations.

Color Sequence

To receive characteristic colors for blue and red galaxies one needs to construct their spectral energy densities (SED). In Figure 4 from Loh et al. (2008), who investigated a synthetic red sequence model for moderate redshifts, the red and blue spectral types are shown. They are enclosed by four SED templates (E–Ellipticals, Sab–Spiral, Sbc–Barred Spiral and Im–Irregular) from Coleman et al. (1980), Kinney et al. (1996). By interpolating between these four templates and applying the appropriate weights in redshift, it becomes possible to extract SED templates for red and blue galaxy types at a broad range of redshifts. These templates enable us to convert magnitudes from one band pass filter to another, k–correct for the redshift and estimate the characteristic color values for red and blue sequence respectively. A color c^t_{12} between bands 1 and 2 for type t is therefore the weighted sum over all four templates j, where the 'cluster' redshift weight $w^t_j(z_c)$ for the type t of template j is applied to the rest frame color $c_{12,j}(0)$ plus the k–Correction $kC_{12,j}(z_c)$ of the j–template.

$$c^t_{12} = \sum_{j=1}^{4} w^t_j(z_c) \cdot \left(c_{12,j}(0) + kC_{12,j}(z_c)\right) . \tag{18}$$

The weights are taken to reproduce the synthetic red sequence from Loh et al. (2008). Specifically red galaxies gain more weight from elliptical and Sab galaxies, while blue galaxies receive a small weight from Sab but more from Sbc and Im. The color evolution of red and blue galaxies, is shown in Figure 4.

According to Hao et al. (2010) different colors must be taken for different redshift bins if they do not cover the 4000 Å break for the redshift range considered. The colors c_{g-r}, c_{r-i} and c_{i-z} enable us to measure the 4000 Å break over the redshift range from 0.1 to 1. The agreement of the synthetic red and blue color templates with predictions of Hao et al. (2010) and Rykoff et al. (2014) becomes visible in Figure 4. The colors for the redshift range 0.1 to 1 and the ranges in agreement with Table 2 of Hao et al. (2010) are summarized in Table 4.

Table 4: Suggested optimal redshift ranges from Hao et al. (2010)

redshift	color
$0.10 - 0.43$	c_{g-r}
$0.43 - 0.70$	c_{r-i}
$0.70 - 1.10$	c_{i-z}

Spatial Sequence

The spatial distribution of red and blue galaxies in the cluster model is determined by a red–fraction function and a shared radial profile. The shared profile can be the projected (Bartelmann, 1996) NFW– (Navarro et al., 1996), Plummer– Plummer (1911) or any other profile. The red–fraction function multiplied with the shared profile defines the profile of red galaxies. The red–fraction in this model is fully specified by the cluster redshift z_c and its characteristic scale M_{200}. The red–fraction in the cluster center is supposed to decrease in high redshift clusters, as can be seen in Figure 6 of Loh et al. (2008). The dependence of the redshift and the cluster-centric distance on the red fraction is thus modeled as rest-frame part

$$f^{red}_0(r) = \min\left(0.9 | \max\left(0.9 \cdot \left(\frac{r}{0.2\,R_{200}}\right)^{-0.148} | 0.57\right)\right) , \tag{19}$$

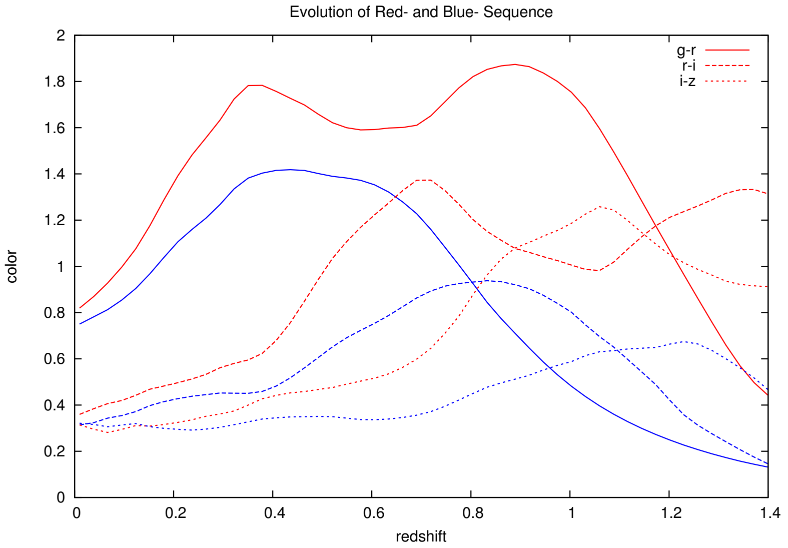

Figure 4: Evolution of c_{g-r}, c_{r-i} and c_{i-z} colors for both red and blue galaxies. Red and blue type SEDs are herby interpolations, based on the study by Loh et al. (2008).

times the rough estimate of redshift dependence $(1 - 0.2\,z_c)$, which has been inspired by Figure 6 in Loh et al. (2008). The final red fraction as function of cluster redshift and distance to the cluster center is expressed by

$$f^{\text{red}}(r, z_c) = f_0^{\text{red}}(r) \cdot (1 - 0.2\,z_c) = f^{\text{red}}(r). \qquad (20)$$

It is necessary to stress that in the analysis of Loh et al. (2008), no clusters with redshifts below 0.3 have been included. Aiming at the redshift range from 0.1 to 1 in this study, it appears bold to simply connect low and high redshift surveys, still a uniform transition does not exist yet.

3.2 RICHNESS OF GALAXY CLUSTERS

Galaxy clusters are defined to be richer in galaxies than their environment. Nowadays, richness is not only a measure of galaxy content of a cluster, but it is also meant to be a proxy for other attributes, such as X-ray luminosity see Rozo et al. (2011) or (more frequently used for cosmological purposes) mass. The definition of richness (N_{200}) varies throughout the literature see e. g. Abell et al. (1989), Postman et al. (1996), Koester et al. (2007b) and more. All definitions share the same principle of confining a hyper volume in which galaxies are found.

A big data set of galaxy clusters became available in the SDSS data with Koester et al. (2007a) maxBCG catalog, which is limited up to $z \simeq 0.3$. In Hansen et al. (2009) average properties of the maxBCG selected clusters (up to redshift 0.3) have been investigated.

Amongst other useful relations from this study, a radius–richness relation is presented. It is very important for two reasons. First, using this relation presumes a richness definition, namely the number of red–sequence galaxies that are brighter than $0.4\,L_\star$ within R_{200}. $L_\star$ is the characteristic cluster luminosity for describing the luminosity distribution of galaxies within a cluster. The relation between radius and richness is given by

$R_{200} = 0.182\,h^{-1}\,\mathrm{Mpc}\,N_{200}^{0.42}$. The second reason is that this relation enables us to relate richness to mass, by relating the scale radius to mass as shown in Equation 16. The final mass–richness relation can then be expressed by:

$$M_{200} = 1.4 \times 10^{12}\,h^{-1}\,M_{\odot}\,N_{200}^{1.26}\,H^2(z). \tag{21}$$

Having this relation at hand, the normalization of the model within the survey limits is fixed.

3.3 BRIGHTEST CLUSTER GALAXY (BCG)

The brightest cluster galaxy (BCG) is believed to be a very special galaxy in the cluster. Not only is it most likely a red–galaxy and by definition very bright but also located in the center of the cluster. Also the gap between the BCG and the next luminous satellite galaxy seems to be characteristic as proposed by Hearin et al. (2013). Another finding of Hansen et al. (2009) is the relation between the BCG luminosity measured in the i–band and the richness. It can be expressed as:

$$L_{\mathrm{BCG}}^{0.25\,i} = 2.16 \times 10^{10}\,N_{200}^{0.38} h^{-2} L_{\odot}. \tag{22}$$

This luminosity–richness dependence is translated into a luminosity–mass dependence through Equation 21.

3.4 RADIAL DISTRIBUTION OF GALAXIES IN A CLUSTER

Because of the uniqueness of the BCG, the model cluster distribution can be considered to have three different types of galaxies: red, blue and BCG. While the normalizations of the red and BCG are straightforward from the mass–richness relation in Equation 21 combined with the red–fraction from Equation 20:

$$N_{200} - 1 = N^{\mathrm{red}} \int_0^{R_{200}} 2\pi r\,dr\,p^{\mathrm{red}}(r) \tag{23}$$

$$1 = N^{\mathrm{BCG}} \int_0^{R_{200}} 2\pi r\,dr\,p^{\mathrm{BCG}}(r), \tag{24}$$

the normalization for the blue galaxies is implied by the relation $p^{\mathrm{blue}}(r) = p^{\mathrm{red}}(r)\frac{1-f^{\mathrm{red}}(r)}{f^{\mathrm{red}}(r)}$. For convenience the profiles are renamed as normalized profiles $N^{\mathrm{red}}\,p^{\mathrm{red}}(r) \to p^{\mathrm{red}}(r)$ and $N^{\mathrm{BCG}}\,p^{\mathrm{BCG}}(r) \to p^{\mathrm{BCG}}(r)$. Two profile types are implemented already, one is extracted from Figure 8 from Sheldon et al. (2009). There the same data as in Hansen et al. (2009) have been evaluated using weak lensing analysis to construct stacked radial profiles for red cluster galaxies. In the original article, these have been plotted for bins of clusters with different richnesses. The second type is the so called Plummer–profile, see Plummer (1911) with a cutoff:

$$P(r) = \frac{1}{\sqrt{1+\left(\frac{r}{r_c}\right)^2}} - \frac{1}{\sqrt{1+\left(\frac{r_{co}}{r_c}\right)^2}}, \tag{25}$$

the two characterizing radii are the cutoff radius r_{co}, which is chosen to be $5 \times R_{200}$ and the fixed core radius $r_c = 0.13$.

The BCG is usually identified with the cluster center, therefore its radial profile can be assumed to be Gaussian around the core, with a narrow width of $\sigma_{\mathrm{rad,BCG}} = 0.2$.

3.5 Distribution of cluster galaxies in magnitude

As fit by Hansen et al. (2009), the luminosity distributions in the analysis by Hansen et al. (2009) of stacked galaxy clusters have been fit to Schechter–luminosity functions, see Schechter (1976):

$$\phi^t(m) = \phi_0^t \, 10^{-0.4(m-m_\star^t)(\alpha^t+1)} \times \exp\left(-10^{-0.4(m-m_\star^t)}\right) \tag{26}$$

To fix the characteristic luminosity $L^\star$, a fixed absolute value for both, red and blue galaxies is chosen to be $1.4 \times 10^{10}\, h^{-2}\, L_\odot$. The corrections from the SED–templates however are then applied according to the considered type. The procedure is as follows. First, the luminosity is converted into an apparent magnitude in the i–band with

$$m^i = m^i_\odot - 2.5 \cdot \log\left(\frac{L^i}{L^i_\odot}\right), \tag{27}$$

afterwards, the correction for the redshift and galaxy type is applied. The exponents for red and blue galaxies are $\alpha^{\mathrm{red}} = -0.53$ and $\alpha^{\mathrm{blue}} = -1$ respectively. The BCG is supposed to have the characteristic luminosity that is related to the cluster richness by Equation 22. Therefore a Gaussian is chosen to represent the probability distribution for the BCG to be at L_{BCG}. For converting luminosity into magnitude, the procedure is as described above, the type correction for the BCG must be that for a red galaxy:

$$\phi^{\mathrm{BCG}}(m) = \phi_0^{\mathrm{BCG}} \frac{1}{\sqrt{2\pi}\sigma_{m,\mathrm{BCG}}} \exp\left(-\frac{\left(m - m^{\mathrm{BCG}}\right)^2}{2\sigma^2_{r,\mathrm{BCG}}}\right). \tag{28}$$

Normalizations are taken such that, integrated up to the survey limit in Sheldon et al. (2009), Hansen et al. (2009), the magnitude distributions result in one, such that only the radial–profile carries the richness information.

3.6 Color distribution of galaxies in a cluster

Given the expectation values for red and blue SED–template colors, the sequences are fixed up to a width. In order to avoid hard cuts, the color distributions are chosen to be Gaussian. The motivation for this is the study by Hao et al. (2010), who developed a classifier of the red sequence based on a Gaussian mixture and error corrected Gaussian mixture models.

The width for the color distributions are taken to be the intrinsic standard deviations for red $\sigma_c^{\mathrm{red}} = 0.05$ and blue $\sigma_c^{\mathrm{blue}} = 0.35$ galaxy types respectively, as measured by Hao et al. (2010). The measurement errors for both types are $\sigma_{\text{measure}} \approx 0.1$ and are just added to the intrinsic ones.

$$G_c^t(c) = \frac{1}{\sqrt{2\pi}\sigma_{c,t}} \exp\left(-\frac{\left(c - c^t\right)^2}{2\sigma_{c,t}^2}\right). \tag{29}$$

The BCG is assumed to be a red galaxy and thus follows the color distribution of red galaxy.

3.7 REDSHIFT DISTRIBUTION OF GALAXIES IN A CLUSTER

The redshift distribution of the cluster is assumed to be equal for all galaxy types. Further, a Gaussian distribution with width determined by the velocity dispersion $\sigma_{z,in} = \sigma_v/c$ is adopted in the first step:

$$\omega(z) = \frac{1}{\sqrt{2\pi}\sigma_z} \exp\left(-\frac{(z_c - z)^2}{2\sigma_z^2}\right). \tag{30}$$

Lastly, as the redshift distribution of galaxies is expected to be smeared by uncertainties in the photometric redshift measure, an external standard deviation is added to the intrinsic dispersion. The squared sum, that is $\sigma_z^2 = \sigma_{z,in}^2 + \sigma_{z,ext}^2$ is the characteristic cluster width in redshift. It is individual for each data set and thus has to be determined from it.

3.8 THE FINAL NUMBER DENSITY MODEL

Regarding all components that have been introduced in the last sections, the number density model for a galaxy cluster, which is primarily described by the mass and redshift and secondarily by the chosen bands and limits can be introduced as:

$$n_{\text{cl}}(r, z, m, \vec{c}) = \omega(z) \sum_{t=\text{red}}^{\text{BCG}} \left(p^t(r)\, \varphi^t(m) \prod_{i=1}^{N_{\text{bands}}-1} G^t(c_i) \right). \tag{31}$$

There are no correlations assumed between different bands, only the radial distribution reflects the population type at a certain cluster redshift. This means, that all components can be removed in order to construct a filter that does not take the whole model into account as presented, but rather parts of it. Some cuts in two dimensions are shown in Section 5.6.

The normalization of the number density is chosen such that integrating over the whole color, redshift and magnitude space within R_{200} yields the combination of N_{200} and the amount of blue galaxies $N_{200,blue}$. The magnitude space is limited by construction to $m_{Sheldon}$, the limit of the survey investigating magnitude distributions.

4

MODEL FOR FIELD GALAXIES IN OPTICAL BANDS

The optimal filter contrasts the signal shape against average properties of the field. These average properties can either be modeled a priori, which needs a justification or estimate from the data itself. Under the assumption that galaxies are isotropically on the sky, the density estimation reduces to the dimension of observables. This Chapter is devoted to the construction of two field galaxy distributions. The first is a Multi–Variate Gaussian (MVG) that is fed with means and covariances from the data. It has a very practical meaning, namely to study how well the density in the data can be estimated and also by how much the filter might be affected by this estimated density. Also generating random data from the MVG is computationally cheap and easy. The second is a density–estimator that uses information from the data composed of several observables. It is a very practical tool, because models for the underlying data do not always exist.

4.1 MULTI–VARIATE GAUSSIAN DENSITY

The Multi–Variate Gaussian is one of the mostly known density distributions among data analysts. It is fully characterized by the means and covariances between the observables. For any amount and combination of observables, the data allows to estimate the mean and covariance therein. These statistical quantities combined with normalization by the angular field of view for the data comprise the density model.

For any combination of these observables, the tables provide the characteristic values for the MVG. Together with a field size of 1 deg^2 and a fixed angular number density therein, the field density can be computed.

4.2 DENSITY ESTIMATION FROM DATA

Different approaches can be gone to estimate the density at a certain location. Density estimation itself is very scale dependent. Averaging over too small scales results in an incoherent density space, while averaging over too large scales may lead to a constant density function. Two distinct approaches with their downsides are: Either fixing a number of objects and increasing the volume until this exact number is reached, or fix a volume and finding out how many objects are within. The question in both approaches remains: How to fix the scale? For the fixed volume approach, an Ansatz could be the optimal binning by Hogg (2008) or the interquartile range (IQR). In general one has to decide for each problem individually.

For the purpose of a contrast for the signal for example, the smoothing can happen on large scales, as more signal will be smoothed out. The only qualitative hint is to choose the scale large enough such that cluster information is removed from the data but small enough such that the distribution does not become constant. In any case, the scale shall not become too small because this would increase the error per cell. Therefore taking larger scales for density estimation is preferable. It reduces the error per cell and smooth out cluster information.

The density estimator in this work is a simple equidistant cell cube. The number of cells in each dimension depends on the dimension and data size. As long as there is enough data, such as ≈ 60k objects in a patch of CARS W1m0p1, the choice is set to 30 cells per dimension.

The amount of objects within each cell is normalized by the cell volume and by the angular field of view for the data. Additionally, a linear interpolation between cells neighboring the addressed position is performed, to assess the true value.

To verify the choices made above, a known density model for the distribution of field galaxies is made and the density–estimation routine tested in two steps. First, justifying the ≈ 30 cells, by comparing distributions from the former to the latter method. The second approach will be to evaluate and compare the filter output for both, semi–analytic MVG input and to purely numerically estimate a density from the simulated MVG catalog.

4.3 COMPARISON OF MULTI–VARIATE GAUSSIAN AND ESTIMATED DENSITIES

To test how well the density estimation routine performs on data, three data sets according to Section 6.3 are drawn from a MVG, using the observables, redshift, m_r and c_{g-r}. The sets contain half, the exact– and ten times– the amount of the objects (n_g) that remain in the W1m0p1 data after cleaning the catalog, see Section 2. The density is estimated for each of the three data sets in the defined volume. This volume is divided into N^3 cells with N= 20 on which the χ^2 test is performed. This implies that there are $N^3 - 1$ degrees of freedom. Because each data set contains another normalization ($0.5 \cdot n_g$, n_g & $10 \cdot n_g$), the impact of the normalization on the χ^2 computation must be accounted for. This is done by dividing out the factor (0.5, 1 & 10) from the χ^2. Table 6 shows the number of objects after three dimensional integration for the semi–analytic and estimated models and the reduced χ^2. As the next to last test in this context, an example

Table 5: Bias and variance of a filter associated with the semi–analytic MVG and estimated density model, for the σ_n^2 term are shown from top to bottom. The number of galaxies in the field is increasing from left to right. n_g is hereby the proper normalization of galaxies.

	$0.5 \cdot n_g$	n_g	$10 \cdot_g$
B_{EST}	0.99	1.82	11.36
B_{MVG}	0.98	1.62	9.89
$\sigma^2_{n,EST}$	2.17	2.95	12.40
$\sigma^2_{n,MVG}$	2.14	2.75	10.92

Table 6: The number of objects after three dimensional integration for the semi–analytic MVG and estimated density model, and the reduced χ^2 are shown.

	$0.5 \cdot N$	N	$10 \cdot N$
semi–analytic N_{int}	62043	62047	61375
density–estimation N_{int}	61716	62339	61616
reduced χ^2	3.39	1.43	0.69

filter described in Section 5.6 is initiated with the semi–analytical MVG and with the estimated density from the simulations (see Section 6.3) as explained above. There are two quantities that have been enforced by the filter in order to be optimally matched, namely the Bias B and the variance σ_Λ^2. In Table 5, these quantities are computed and shown for a RedMagCol–filter that uses a cluster template with mass $M = 5 \times 10^{14} M_\odot$ and redshift $z_c = 0.3$ suited for application in the (r,g) bands i. e. using the observables redshift, m_r and c_{g-r}. It might be not representative but serves as a good guess for whether the estimated quantities are in principle right or not. In contrast to the χ^2 statistics the increased number does not lead to a better match between the density–estimator and MVG density approaches.

5

OPTIMAL MATCHED FILTER

Any data set $d(\vec{\theta},\vec{y})$ can be decomposed into two parts, $d(\vec{\theta},\vec{y}) = s(\vec{\theta},\vec{y}) + n(\vec{\theta},\vec{y})$. The signal $s(\vec{\theta},\vec{y}) = \Lambda\,\tau(\vec{\theta},\vec{y})$ and the noise $n(\vec{\theta},\vec{y})$. Suppose one knows the mean properties of the data. Namely, if no signal is present in the data, the mean noise component can be modeled as $\langle n\rangle = n_m(\vec{\theta},\vec{y})$. The task is to construct a filtering or weighting function, that responds if the data contains signal of a certain strength (in best case it also measures the strength) and does not respond if no signal is present. On average this function shall reproduce the unbiased signal strength **if applied to data containing exactly that signal**. Following linear filtering theory Williams (1995), the signal strength estimate

$$\Lambda_{est}(\vec{\theta}_0,\vec{y}_0) = \int \Phi(\vec{\theta}_0-\vec{\theta},\vec{y}_0-\vec{y})\, d(\vec{\theta},\vec{y})\, d\vec{\theta}\, d\vec{y} \tag{32}$$

is introduced as a convolution of the data with the sought weighting function Φ. Coordinates $(\vec{\theta}_0,\vec{y}_0)$ stand for the characteristic location in the parameter space. For convenience they will be omitted in the further notation. The spatial coordinates (projected angle) are hereby represented by θ, whereas $\vec{y}$ contains all other relevant parameters (as redshift, magnitude and colors). On average the estimate of the signal strength is unbiased in the above sense as long as the filter works on a zero mean noise field $n_m = 0$. A zero mean noise can be easily constructed by substituting $n - n_m$ for n, such that $n^\star_m = \langle n^\star\rangle = 0$. The variance of $n^\star$ remains the same as for n, namely $\sigma^2_n = \sigma^2_{n^\star}$. The unbiased estimate can now be written as:

$$\begin{aligned}
\langle\Lambda_{est}\rangle &= \int \Phi(\vec{\theta},\vec{y})\, \langle d^\star\rangle(\vec{\theta},\vec{y}) = \langle\Lambda^b_{est}\rangle - \bar{B} && (33)\\
&= \Lambda \int \Phi(\vec{\theta},\vec{y})\, \langle\tau\rangle(\vec{\theta},\vec{y})\, d\vec{\theta}\, d\vec{y} + \int \Phi(\vec{\theta},\vec{y})\, \langle n\rangle(\vec{\theta},\vec{y})\, d\vec{\theta}\, d\vec{y} && (34)\\
&\quad - \int \Phi(\vec{\theta},\vec{y})\, n_m(\vec{\theta},\vec{y})\, d\vec{\theta}\, d\vec{y} &&\\
&= \Lambda \int \Phi(\vec{\theta},\vec{y})\, \tau_m(\vec{\theta},\vec{y})\, d\vec{\theta}\, d\vec{y} + \int \Phi(\vec{\theta},\vec{y})\, n_m(\vec{\theta},\vec{y})\, d\vec{\theta}\, d\vec{y} - \bar{B} && (35)\\
&= \Lambda, && (36)
\end{aligned}$$

implying the normalization condition for the filter

$$\int \Phi(\vec{\theta},\vec{y})\, \tau_m(\vec{\theta},\vec{y})\, d\vec{\theta}\, d\vec{y} = 1, \tag{37}$$

and the biasing term

$$\bar{B} = \int \Phi(\vec{\theta},\vec{y})\, n_m(\vec{\theta},\vec{y})\, d\vec{\theta}\, d\vec{y}. \tag{38}$$

At some point, it will be necessary to specify the variance of the noise field. In this work, the number density in the field is assumed to follow a Poissonian distribution. This assumption implies that $\sigma^2_{n^\star} = \sigma^2_n = n_m$ and reduces the information needed from the data, to the average number densities for all positions in the parameter space. The signal strength estimate will fluctuate around its expected value $\langle \Lambda_{est} \rangle = \Lambda$. Its variance is simply $\sigma^2_\Lambda = \langle \Lambda^2_{est} \rangle - \Lambda^2$. Inserting the definition of the signal strength estimate from Equation 32 into the definition of its variance yields:

$$\sigma^2_\Lambda = \left\langle \int d\, \Phi d\Omega \int d'\, \Phi' d\Omega' \right\rangle - \Lambda^2 \tag{39}$$

$$= \int\int \Phi\, \Phi' \langle d\, d' \rangle d\Omega' d\Omega \ - \Lambda^2, \tag{40}$$

The auto correlation in the data $\langle d\, d' \rangle$ can now explicitly be written down:

$$\langle d\, d' \rangle = \left\langle (\Lambda\tau + n^\star) \left(\Lambda\tau' + n^{\star\prime}\right) \right\rangle \tag{41}$$

$$= \Lambda^2 \langle \tau\, \tau' \rangle + \Lambda \langle \tau\, n^{\star\prime} \rangle + \Lambda \langle \tau'\, n^\star \rangle + \langle n^{\star\prime}\, n^\star \rangle. \tag{42}$$

A priori one does not know the variance in the data. The first guess in this work is to put all uncertainties into the mean field. This means that the signal shape needs to be known exactly (no variance) and no correlations between signal shape and noise field exist:

$$= \Lambda^2 \langle \tau \rangle \langle \tau' \rangle + \Lambda \langle \tau \rangle \langle n^{\star\prime} \rangle + \Lambda \langle \tau' \rangle \langle n^{\star\prime} \rangle + \langle n^{\star\prime}\, n^\star \rangle \tag{43}$$

$$= \Lambda^2 \tau_m \tau'_m + \sigma^2_{n^\star} \delta(\Omega - \Omega'). \tag{44}$$

To arrive from Equation 42 at Equation 43 it was first used, that **the variance of the signal shape is zero, meaning the signal is known exactly**. Second, **cross–correlations between signal shape and noise do not exist or can be ignored**. Further, making use of the zero mean condition and statistics of the noise field, discussed in the beginning of this Section, the final expression for the data auto correlation can be found in Equation 44. This corresponds to $\sigma^2_{d^\star} = \sigma^2_{n^\star}$. In this case the variance of the signal strength estimate can be rewritten as:

$$\sigma^2_\Lambda = \int \Phi^2(\vec{\theta}, \vec{y})\, \sigma^2_{n^\star}(\vec{\theta}, \vec{y})\, d\vec{\theta}\, d\vec{y} = \int \Phi^2(\vec{\theta}, \vec{y})\, n_m(\vec{\theta}, \vec{y})\, d\vec{\theta}\, d\vec{y} \tag{45}$$

Of course the fluctuations of the strength estimate will be amplified, if cluster galaxies are present at the position of the search, because they also contribute to the mean field. To account for this, the following is considered. To approximation the fluctuations are assessed by neglecting the contribution from the presence of cluster galaxies. In this case, $\sigma^2_{d^\star} = \sigma^2_{n^\star} = n_m$, meaning that the data is sharing the statistics of the mean field. This implies that the variance of the signal strength estimate is $\sigma^2_{mf} = \int \Phi^2\, n_m d\Omega$. This approximation is not bad, since the expected number density of galaxies from a cluster (which is not known) at a certain location should be small in comparison to the field $\langle d^\star \rangle = \langle \Lambda\tau + n^\star \rangle \approx \langle n^\star \rangle$ on average. The impact of a cluster on the data variance can additionally be approximated. As argued by Bellagamba et al. (2011), it is possible compute a correction term, after the filtering function has been defined. This means, that the filter is constructed using the assumption of no cluster presence in the noise field. Afterwards, the signal strength estimate is computed with $\sigma^2_{d^\star} = \sigma^2_{n^\star} = \Lambda_{est}\tau_m + n_m$, such that the corrected signal strength estimate variance becomes $\sigma^2_{\Lambda,\mathrm{corr}} = \sigma^2_{\mathrm{mf}} + \sigma^2_{\mathrm{cl}}$, with the last term $\sigma^2_{\mathrm{cl}} = \int \Phi^2 \Lambda \tau_m d\Omega$. The σ^2_{cl} term mimics the Poissonian contribution of cluster galaxies to the mean field. The two variances for the estimated strength can be used in two different contexts. The first, σ^2_{mf}, contains the field galaxies only and is therefore well suited to distinct the presence of a cluster from a random fluctuation in the field in terms of signal to noise of the detection. The second, corrected term however is a good approximation of the standard error on the estimate, which propagates to the richness that can be inferred.

5.2 OPTIMAL FILTER DETERMINATION

Matched filtering means that a model in the filter is matched to the signal shape that one expects to find. Optimality has two requirements, first **the filter shall result in an unbiased estimate of the signal if applied to data containing that signal**. Second, **the variance of the estimate shall be minimal**. To enforce both conditions, the following functional for the filter is introduced:

$$L = \sigma^2_\Lambda + \lambda B. \tag{46}$$

Its functional derivative with respect to the filter Φ while keeping the Lagrangian multiplier λ, minimizes the variance:

$$\frac{\delta L}{\delta \Phi} = \frac{\delta \sigma^2_\Lambda}{\delta \Phi} = \int \Phi\, \sigma^2_n d\Omega + \lambda \int \tau_m d\Omega = 0. \tag{47}$$

Solving the above Equation for the filter results in the preliminary filtering function:

$$\Phi(\vec{\theta}, \vec{y}) = -\lambda \frac{\tau_m(\vec{\theta}, \vec{y})}{\sigma^2_n(\vec{\theta}, \vec{y})}. \tag{48}$$

This preliminary filter function can be fixed by inserting it into the filter normalization Equation 37, which is equal to the derivative of the functional L with respect to λ:

$$\frac{dL}{d\lambda} = B = 0. \tag{49}$$

The final result is the optimal matched filter, that is proportional to the signal shape and anti proportional to the variance of the noise:

$$\Phi(\vec{\theta}, \vec{y}) = \frac{\tau^2_m(\vec{\theta}, \vec{y})}{\sigma^2_{n^\star}(\vec{\theta}, \vec{y})} \left[\int \frac{\tau^2_m(\vec{\theta}, \vec{y})}{\sigma^2_{n^\star}(\vec{\theta}, \vec{y})} d\vec{\theta}\, d\vec{y} \right]^{-1} = \frac{\tau^2_m(\vec{\theta}, \vec{y})}{\sigma^2_{n^\star}(\vec{\theta}, \vec{y})} \cdot \Phi_N, \tag{50}$$

Φ_N is here the normalization of the filter. It is also equal to the variance contribution of the field

$$\sigma^2_{\Lambda,\mathrm{mf}} = \left[\int \frac{\tau^2_m(\vec{\theta}, \vec{y})}{n_m(\vec{\theta}, \vec{y})} d\vec{\theta}\, d\vec{y} \right]^{-1} = \Phi_N. \tag{51}$$

Table 7: Limits in the cluster model scaled by κ. The characteristic locations and filter volume limits are shown.

	location	minimum	maximum
radial	0	0	$\kappa_r \cdot R_{200}$
magnitude	$m_\star^{red}, m_\star^{blue}, m_{BCG}$	m_{min}	$m_{Sheldon}$
color	c^{red}, c^{blue}	$\min\limits_{c^{red}-\kappa_c \cdot \sigma_c^{red}, c^{blue}-\kappa_c \cdot \sigma_c^{blue}}$	$\max\limits_{c^{red}+\kappa_c \cdot \sigma_c^{red}, c^{blue}+\kappa_c \cdot \sigma_c^{blue}}$
redshift	z_c	$z_c - \kappa_z \cdot \sigma_z$	$z_c + \kappa_z \cdot \sigma_z$

Together with the correction of the cluster term which needs to be added to the mean field

$$\sigma^2_{\Lambda,\text{cl}} = \Lambda \cdot \int \frac{\tau_m^3(\vec{\theta},\vec{y})}{n_m^2(\vec{\theta},\vec{y})} d\vec{\theta}\, d\vec{y} \left[\int \frac{\tau_m^2(\vec{\theta},\vec{y})}{n_m(\vec{\theta},\vec{y})} d\vec{\theta}\, d\vec{y} \right]^{-2} = \Lambda \cdot \int \frac{\tau_m^3(\vec{\theta},\vec{y})}{n_m^2(\vec{\theta},\vec{y})} d\vec{\theta}\, d\vec{y} \cdot \Phi_N^2, \quad (52)$$

the final corrected variance of the signal strength estimate is $\sigma^2_\Lambda = \sigma^2_{\Lambda,\text{cl}} + \sigma^2_{\Lambda,\text{mf}}$.

5.3 COMMON LIMITS FOR CLUSTER AND FIELD MODELS

The implementation of the filter allows to reduce or increase the volume in which the filter is defined. Specifically, one can choose a value κ for each observable, which sets the limits in which the model number density will be normalized to one. The limits in terms of κ_r, κ_z and κ_c are introduced in Table 7. It summarizes how the characteristic radial R_{200}, color σ_c and redshift σ_z scales are related to the corresponding κ. The data imposes additional limits on the filter. If there are no galaxies above a certain brightness, the filter should know and renormalizes accordingly. Therefore the lower limits on the filter are set to the maximum of the cluster– and model–minimum. Whereas the upper limits are set to the minimum of the cluster– and model–maximum. This volume selection ensures that both cluster– and field– distribution functions are consistently defined.

5.4 AVOIDING CUSPY CORE

At high redshifts fewer galaxies are predicted according to the mass–function. The cluster model responds to this by expecting few clustered galaxies only. If the filter (radial) profile is cuspy however, the signal estimation might be artificially inflated if the location of a single galaxy coincides with the center for the cluster model. In this case, the large weight from the BCG will add up to the strong up weighting by the steep satellite profiles (red and blue galaxies). To avoid too cuspy cores in the satellite profiles, the radial filter is convolved with a low pass filter $f_{\text{res}}(k, k_{\text{res}})$. The modes that need to be suppressed are determined by the scale k_{res}. It is estimated from the mean average separation (MAS) of galaxies in the field. The (spatial) mean number density N_{mf} in $\text{Mpc}^{-}2\ h^2$ is computed in the optical filter limits. The scale is set to $k_{\text{res}} = \frac{1}{3\text{MAS}} = \frac{\sqrt{N_{\text{mf}}}}{3}$. The radial filter is convolved, by transforming into Fourier space, multiplying with the resolution function and transforming back to real space.

5.5 REGULARIZATION TERM

A technical implementation detail of the optimal filter is that the denominator, although a statistical value, which should by no means become zero in theory, can become zero in practice[1]. To avoid numerical problems in the denominator, two number densities are added to the $\sigma_n^2 = n_m$ term. Each of them is normalized to unity in the filter volume, such that the overall contribution to the estimate is expected to be low. The first, is a fixed constant n_0 that corresponds to one galaxy over the filter volume. It offsets the denominator such that zero cannot appear. The second term τ_m is introduced in addition. It regulates the weight, of regions that are strongly emphasized although no cluster signal is expected to be there. This happens, when at some point the field noise is estimated zero, but the cluster model still has an finite density at that point. Combined, the regulated denominator reads $\sigma_n^2 = \tau_m + n_m + n_0$. No significant changes, besides the explained benefits are expected or observed.

5.6 EXAMPLE OF SEVEN POSSIBLE FILTER COMBINATIONS

Given the cluster–τ_m and field–n_m galaxy distributions from Chapters 3 and 4, the filtering function according to Equation 50 can now be composed. The cluster galaxy distribution functions as they are presented here allow seven possible combinations of filters. In principle even more combinations after extending the number of observables (redshift, magnitude and color) is possible. In practice the field galaxy number density estimation will become inaccurate. In the following, seven possible filters are presented together with their density functions/maps for a $M = 5 \times 10^{14} M_\odot$, $z_c = 0.3$ cluster in the r′ band and c_{g-r} color. The limits are chosen according to Section 5.3, whereby the limits for the field galaxies in redshift, magnitude and color are given by a 9 deg^2 simulation of the appropriate MVG according in Section 6.3 in Chapter 6.

Redshift filter has a characteristic width that is the standard deviation in the Gaussian profile. Its intrinsic part is coming from peculiar motion of galaxies towards the cluster center as stated in Section 3.7. It creates a very narrow redshift profile of typically $\sigma_z \approx 0.001$. If the data is coming from a photometric survey, this narrow profile will be smeared by the uncertainties in the redshift measurement. Therefore the intrinsic redshift profile is convolved with an Gaussian, consistent with the mean 1–σ error of the data. Effectively, the Gaussian standard deviations quadratically add up. *Magnitude* filter is a combination of red and blue Schechter–luminosity functions and a Gaussian distribution in BCG magnitude, as stated in 3.5. This approach is somewhat related to but different from that of Postman et al. (1996). The limit for the magnitude distribution is the absolute survey limit magnitude of Sheldon et al. (2009) transformed into apparent magnitude, using proper k-correction. *Color* filter only needs to be subdivided into two population types, namely blue and red. The reason for this is, that the BCG is as-

---

[1] By estimating the field galaxy number density from the data, as summarized in Section 4.2 a cell can for example have no entries.

sumed to behave as a red galaxy. Other possible filters are the combinations of the three. These combinations are redshift and magnitude (*RedMag*), redshift and color (*RedCol*), magnitude and color (*MagCol*) and redshift, magnitude and color (*RedMagCol*). In the following, these seven filters are shown by means of one and two dimensional distribution maps. This implies that all other dimensions are integrated out using the filter limits. This illustration serves the purpose to qualitatively show how the filter responds to the cluster and field galaxy distribution models, knowing both underlying models exactly. The example is constructed with a $M = 5 \times 10^{14} M_{\odot}$ cluster at $z_c = 0.3$ in redshift. The considered band and color are r' and c_{g-r} respectively. The assumed mean error in redshift is measured from CARS according to Chapter 1, Section 2. The mean and covariance values for the MVG are taken from Section 4.1 in Chapter 4.

ONE DIMENSIONAL MAPS

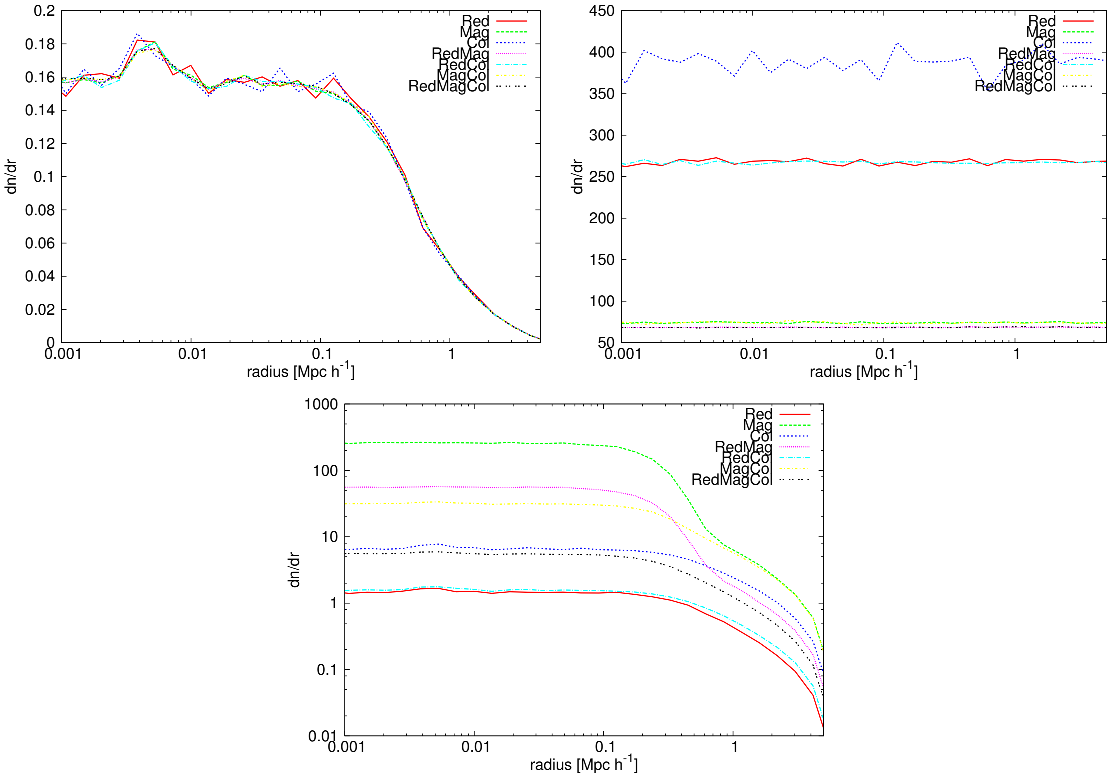

Figure 5: Radial distributions of the seven possible filter combinations based on three observables (see text). The information in all other observables is integrated out in the defined filter volume. On top, cluster signal is shown on the left and field noise on the right. Bottom shows the resulting filters, normalized in the associated volume.

The radial distributions for the cluster signal (top left), field noise (top right) and the resulting filter (bottom) are shown in Figure 5. The bump below 0.01 $\mathrm{Mpc\,h^{-1}}$ is the BCG contribution to the profile. The difference in the field noise is due to the limitations imposed by the filter. As the noise is computed in the filter limits, this reduces the amount of noise in the RedMagCol case dramatically. Color has the least impact on the reduction of field galaxies. This is, because the color range according to Section 5.3 is less restrictive than its shape. The shape of the filter (bottom) is a result of Equation 50, the normalization of the filter follows the Equation 37 with corrections from Section 5.5. As shown in Equation 51, the variance of the signal estimate is proportional to the filter normalization Φ_N. Therefore does the high normalization yield a small signal to noise ratio, because the expected signal remains the same for all filters. Redshift distributions,

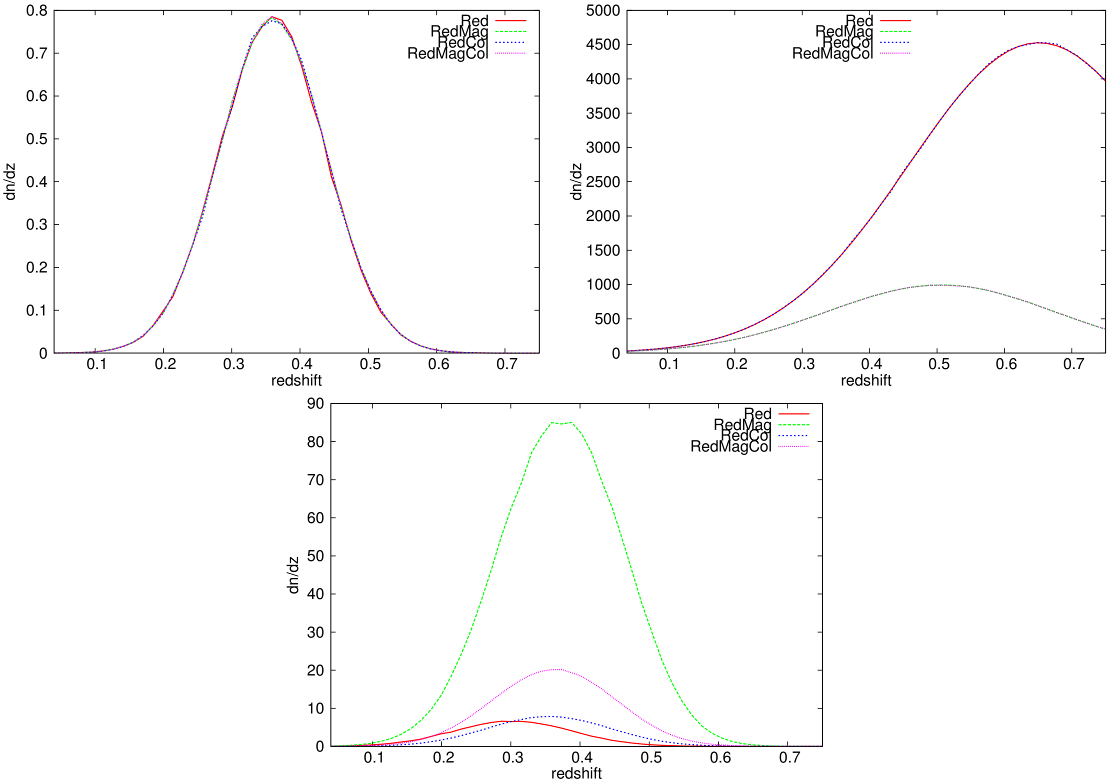

Figure 6: Redshift distributions of the seven possible filter combinations based on three observables (see text). The information in all other observables is integrated out in the defined filter volume. On top, cluster signal is shown on the left and field noise on the right. Bottom shows the resulting filters, normalized in the associated volume.

oriented in the same way as the radial plots are shown in Figure 6. Here one can see clearly, how the noise affects the filter function. Especially in the redshift–filter, the filter–peak shift towards lower redshifts as a result of the steep rising of the field galaxy number density with redshift. Only the use of additional information such as color and magnitude leaves the filter peak in the proper place. Although magnitude–filter on its own is expected to have very high variance of the signal strength estimate, because of the large filter normalization, does the combination three observables combined perform best in this regard. The magnitude distributions are shown in Figure 7. To show the effect of additional observables, the filter is shown on a logarithmic scale. If one had to rely on the magnitude filter only, one would always favor bright galaxies. Not all galaxies are bright, especially those distant galaxies needed most to investigate the past of the universe are very faint. The effect of additional information in terms of color and redshift

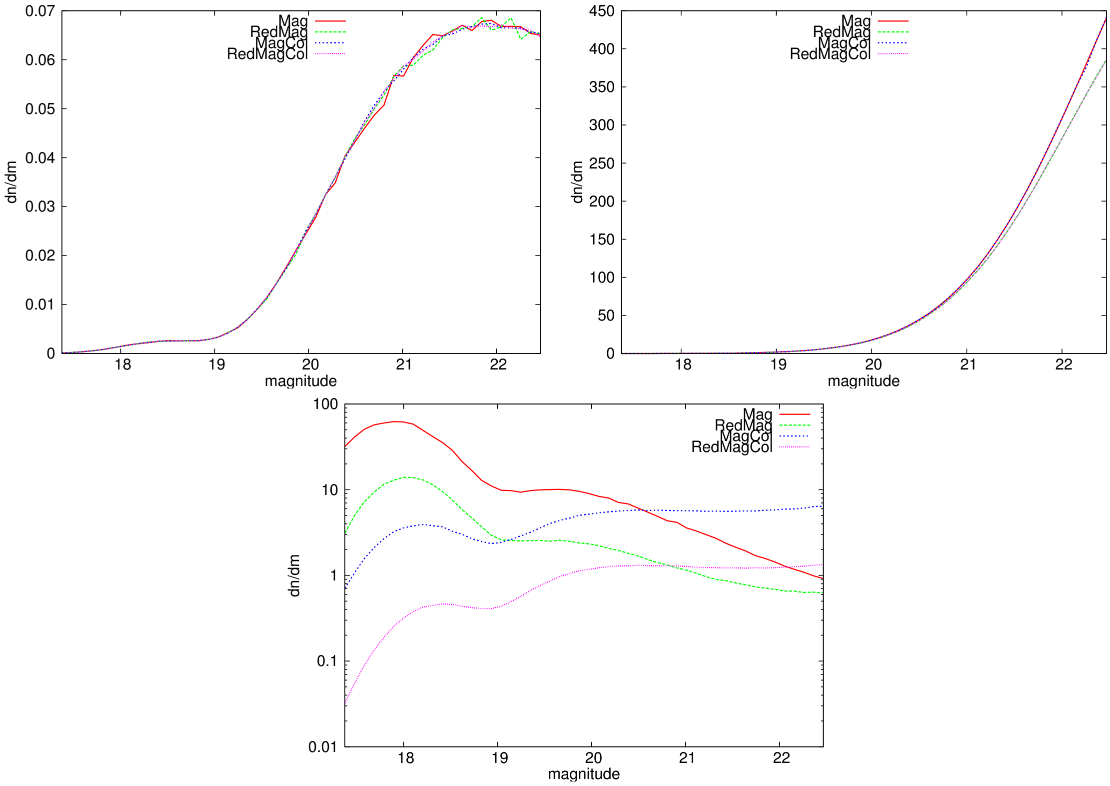

Figure 7: Magnitude distributions of the seven possible filter combinations based on three observables (see text). The information in all other observables is integrated out in the defined filter volume. On top, cluster signal is shown on the left and field noise on the right. Bottom shows the resulting filters, normalized in the associated volume.

is tilting the distribution and corrects the selection function which as seen in the signal (top left), also expects many faint galaxies at redshift 0.36.

Also the color filter alone, shown in Figure 8 can still be improved by combining all observables, even though it does outperform the RedMag filter in terms of the field contribution to variance.

TWO DIMENSIONAL MAPS

Because some correlations are provided by the field galaxies, below also two–dimensional maps of the used distributions are shown. In Figure 9 the distributions in redshift and magnitude are shown. The filter used is the RedMagCol filter that has been integrated in radial and color space. The correlation in the field is seen clearly (top right) and the filter (bottom) responds to this fact. The Gaussian around 18 mag corresponds to the BCG contribution.

Correlations between redshift and color in the field (top right) are shown in Figure 10. The filter (bottom) response to the general trend of field galaxies to have bluer colors with increasing redshift is the suppression of blue colors and relative amplification of red ones.

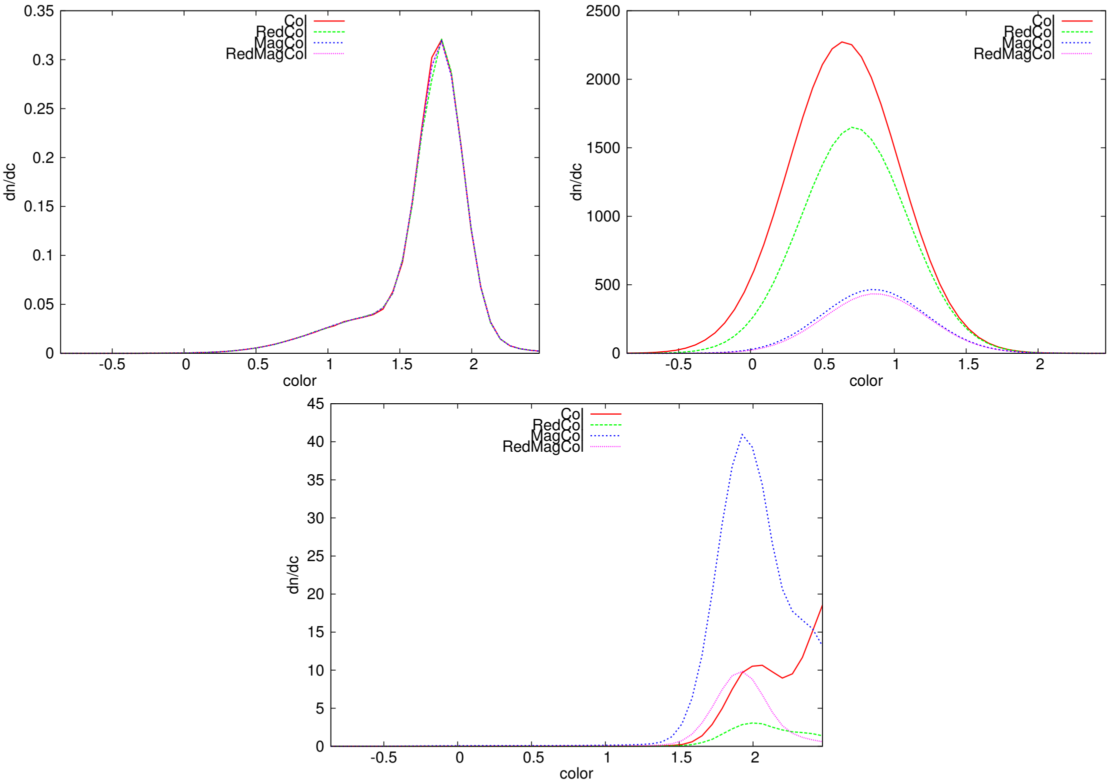

Figure 8: Color distributions of the seven possible filter combinations based on three observables (see text). The information in all other observables is integrated out in the defined filter volume. On top, cluster signal is shown on the left and field noise on the right. Bottom shows the resulting filters, normalized in the associated volume.

Also magnitude and color correlate strongly in the field (top right), as shown in Figure 11. The filter (bottom) response to the general trend of field galaxies to have bluer colors with increasing magnitude is the suppression of colors below 1.4 which is a proximate separation between red and blue galaxies according to the cluster model (top left). The resulting filters can in fact be regarded as cluster distribution divided by field distribution, with a proper normalization (as stated in Equation 37). Specifically, one sees the impact of the field galaxy distribution model on the filter. Regions that are prominent in the field galaxy distribution, i. e. the mean values (redshift 0.6508, color 0.6501 and magnitude 23.6488) of the MVG distribution which was used for these filter initialization are down weighted by the filter. Regions where the cluster distributions are prominent and field galaxy distribution low are emphasized.

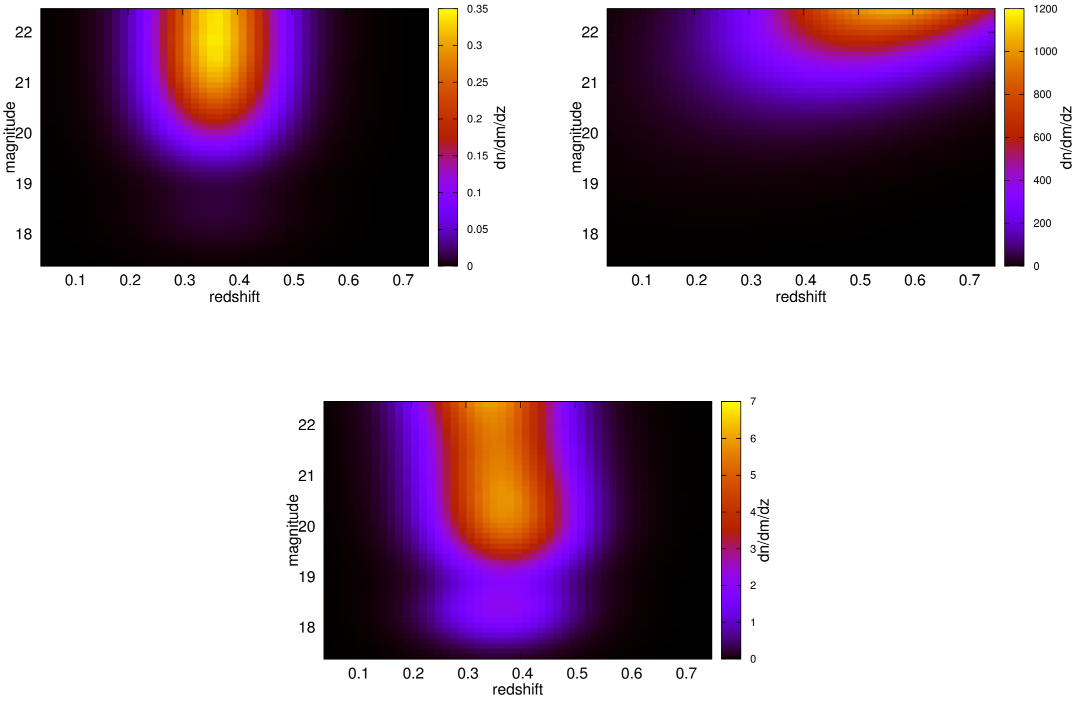

Figure 9: Redshift–Magnitude distribution maps. Cluster– (top left), field– (top right) and filter (bottom) distributions are shown. The remaining dimensions have been integrated out within the filter limits. The Gaussian around 18 mag corresponds to the BCG distribution.

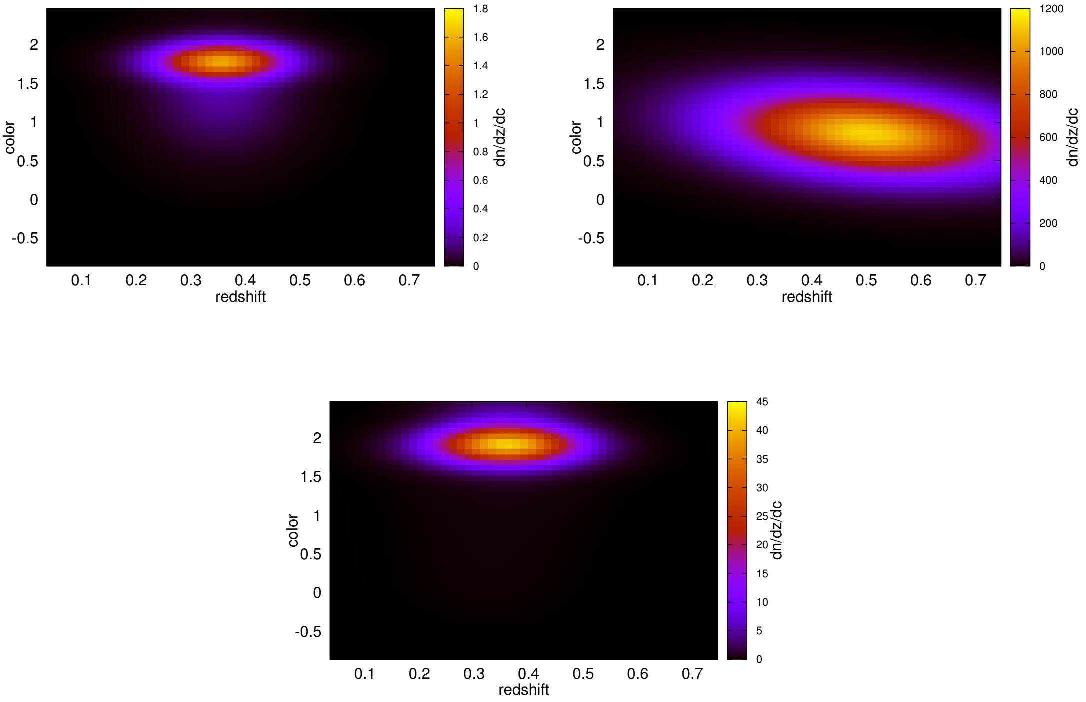

Figure 10: Redshift–Color distribution maps. Cluster– (top left), field– (top right) and filter (bottom) distributions are shown. The remaining dimensions have been integrated out within the filter limits.

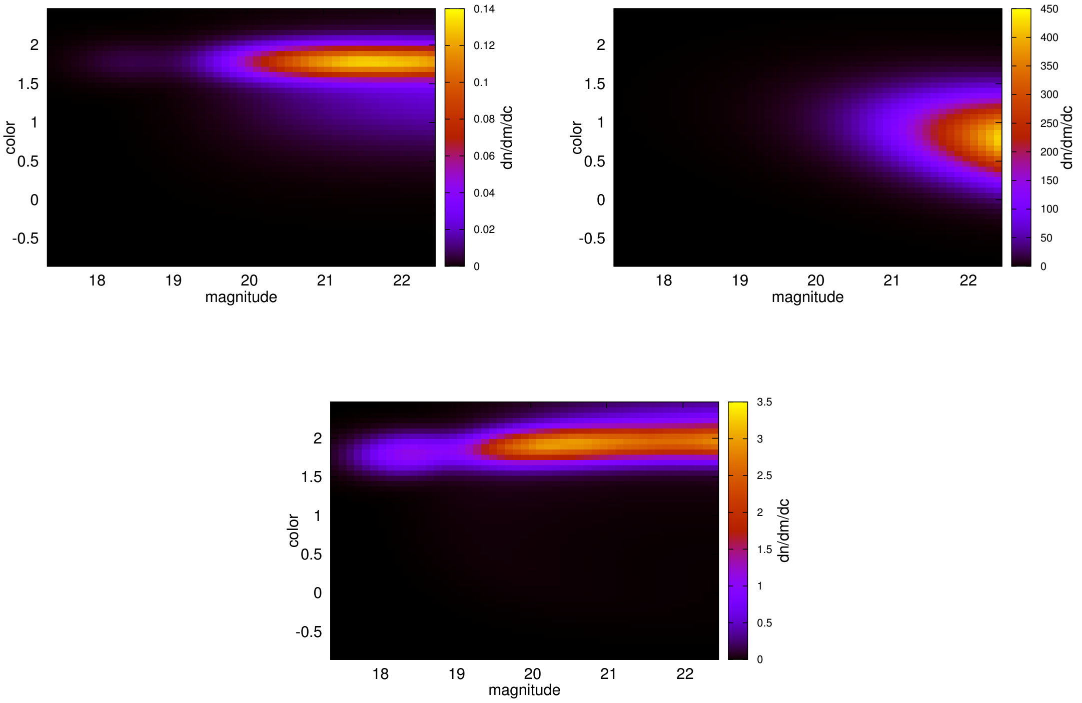

Figure 11: Magnitude–Color distribution maps. Cluster– (top left), field– (top right) and filter (bottom) distributions are shown. The remaining dimensions have been integrated out within the filter limits.

Part II

EVALUATION OF FILTER–PERFORMANCE AND –APPLICATIONS

6

GENERATION OF SYNTHETIC DATA

In the following the tools to test the filter performance, namely simulations of artificial data are described. These simulations serve to verify the proper functionality of the filter as well as predictions which can be tested by means of data drawn from a known distribution. There are three distinct simulations. The first allows to draw random numbers from a mass–function, namely mass and redshift tuples which define the dark–matter halo. It also assigns a random location in right ascension and declination to them in order to maintain the isotropy on large scales. Next, on top of each dark–matter halo, a galaxy cluster in the chosen bands will be placed. Again, the mock cluster needs to preserve the characteristic galaxy distributions that the cluster contains. Lastly, field galaxies are to be simulated. They can be either produced from the data itself, removing the spatial information, or from a known distribution function, such as the MVG.

With these simulations, it becomes feasible to test the density–estimation algorithm from Section 4.2, as done in Section 4.3 in Chapter 4 as well as the functionality and predictive power of filters introduced in Section 5.6 in Chapter 5.

MULTIPLE-DIMENSIONAL CDF MAPPED ON A ONE DIMENSIONAL CDF

The idea of creating realizations from arbitrary distribution functions is presented in some detail in the diploma thesis Gelsin (2011). Here the general idea is summarized. Given certain limits in the space of the distribution function, it can be normalized to the total integral within this volume:

$$\int_{\vec{x}_{min}}^{\vec{x}_{max}} f(x) f_n \, dx = 1 \tag{53}$$

Now the distribution is a probability density function (PDF) which is defined in the selected volume. Further, this volume can be segmented into cells and to each cell a probability can be assigned by integrating the PDF in the cell volume. The probabilities, that at the example of two dimensions can be seen on the right in Figure 15 are contributions to the cumulative distribution function CDF that can be seen in Figure 12. The multi–dimensional CDF is neither unique nor easily invertible in general. This makes it difficult to draw random numbers from such a multi–dimensional CDF. But as the volume is subdivided into cells, one can sum up the cells and create a one–dimensional CDF that is discrete. To draw random numbers from $[0:1]$ is numerically easy, as there are plenty numerical random number generators (GSL[1], TRNG[2] to name at least two) available. The order of cells that are summed up does not matter anymore, because cells that have a larger CDF_i will be hit with a higher probability than those with smaller

---

[1] http://www.gnu.org/software/gsl/

[2] http://numbercrunch.de/trng/

CDF_i. The problem is thus reduced to find the appropriate cell size and determine the cell CDF_i. The intuitively best choice of cell size is such that the distribution within the cells is flat. This guarantees that within the cell, the values are drawn correctly by simply picking D random values from $[0:1]$ and enhancing them with the right space extent: $x^D_{min,i} + dx^D_i * [0:1]^D$. In practice this need an explicit analysis of the distribution and therefore slows down the simulation. As long as the resolution scale in the data does not need to be higher than the cell size, the mock data from this algorithm are sufficiently accurate for the purpose of filtering.

6.1 DARK MATTER HALOS

The simulation is performed within a square field of 3×3 deg^2. The redshift and mass limits are set to $[0.2:1]$ and $[5e13:1e15]M_\odot$ respectively. The mass limits are chosen to account for galaxy groups and big clusters of galaxies.

The mass–function is built upon cosmological parameters as described in Section 1.2. The standard values for this thesis are taken from Section 1.3. The last input choice is the mass–function type. Here the focus is on that from Jenkins et al. (2001) although any from Section 1.2 can be chosen.

Following the procedure described above, the mass function is divided into cells that are labeled in only one dimension. The simulation limits i. e. redshift and mass volume as well as the FOV determines the normalization, that is the final number of resulting dark–matter halos. In the prescribed field, the expectation number of dark–matter halos is 409. Figure 13 shows the location of all these halos on the sky. Figure 12 shows the resulting CDF for the Jenkins mass function plotted against cell id. It has very characteristic features for the mass function if one selects and considers a single block of ≈ 50 cells. This feature is expected, because these cells in one block correspond to different mass bins. The flattening towards growing bin number means that the high mass end of the mass–function is approached. This tail is less probable and therefore flattens for higher masses. The simulation outcome i. e. the dark–matter halo catalog positions in redshift and mass are compared to the predicted distributions. Hereby it is marginalized over the respectively other variable. The $\chi^2/\mathrm{d.o.f.}$ for the mass– and redshift–distributions are 2.09 and 0.66 respectively. The distributions are shown in Figure 14. The predicted mass–function is traced quite well, although the small sample is accompanied by large Poissonian errors. The two dimensional maps are shown in Figure 15. It is immediately apparent that the number of random points results in large error bars because of the small sample. Nevertheless can also be seen that the simulation resembles the expectation within the limits of the Poissonian noise.

6.2 CLUSTER GALAXIES

Cluster galaxies are placed into the dark–matter halos in the following way. Based on the primary parameters mass and redshift of the host halo, secondary parameters come into play. The optical bands, in which the galaxies are observed as well as the profile type and the width imposed by the data, as explained in Section 3.7, Chapter 3. The full distribution function as presented in Section 3.8, Chapter 3 is constructed from and

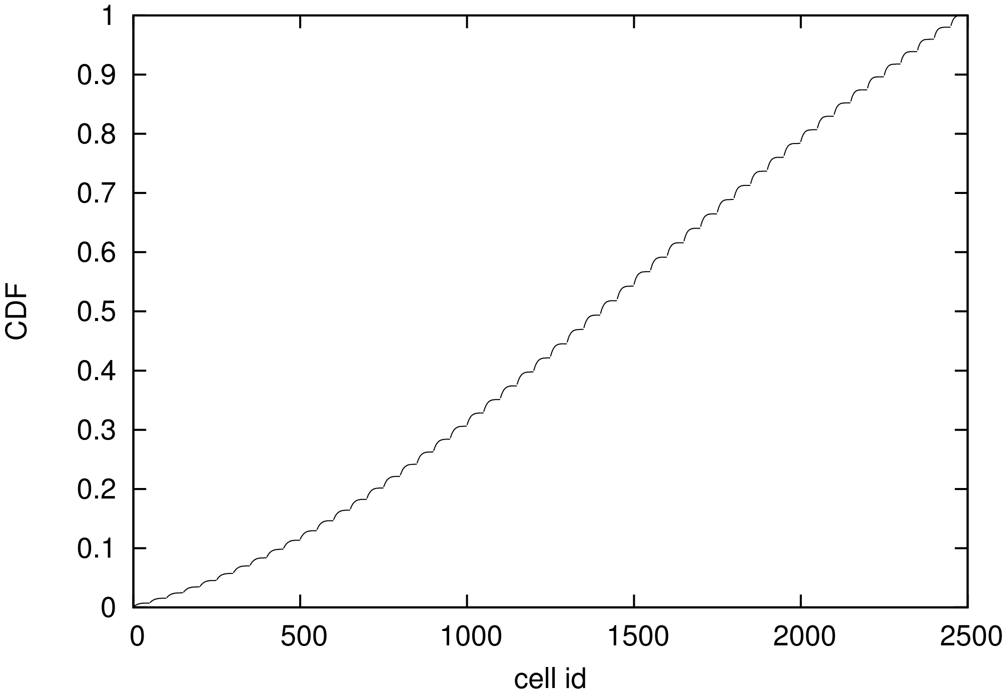

Figure 12: CDF of Jenkins mass–function against cell ids. The number of cells in total is 2500. The cells cover the considered volume. The characteristic look of the function is due to the order of cell computation and summation and is expected.

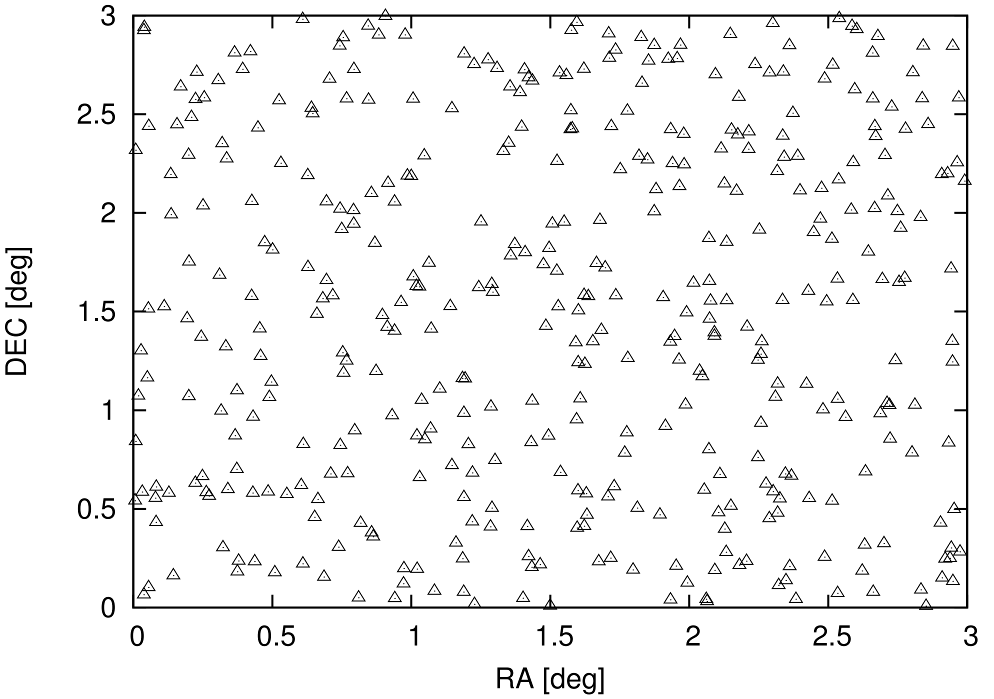

Figure 13: 409 dark matter halos in the 3×3 deg^2 box, randomly picked from the Jenkins mass–function.

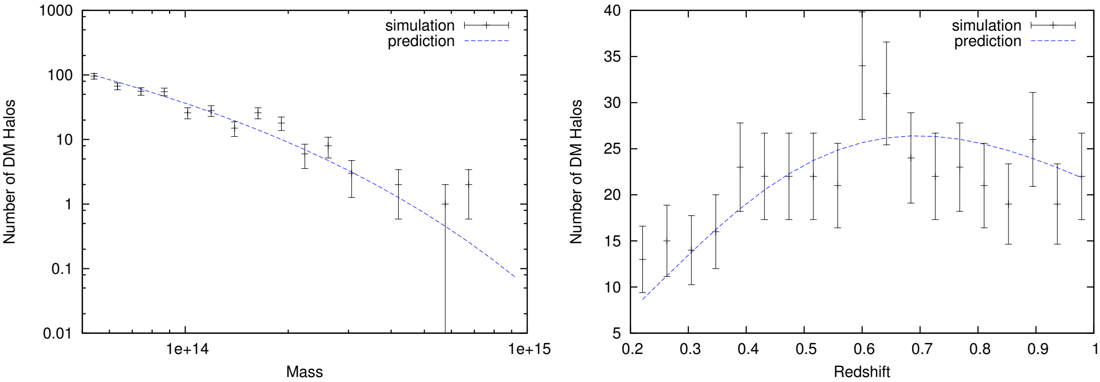

Figure 14: Predicted Jenkins (2001) mass–function marginalized over redshift (left) and mass (right) in blue, versus distribution of simulation data within 20x20 cells in mass and redshift in black. Poissonian error bars provided.

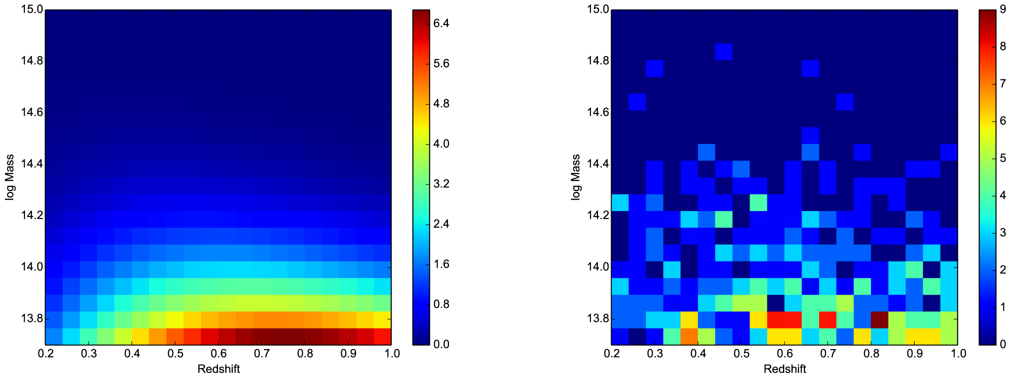

Figure 15: Predicted Jenkins (2001) mass–function (left) and simulation 2d histogram (right). The data is distributed within 20x20 cells in mass and redshift.

rests on these parameters. The final multi–dimensional CDF that is projected on one dimension is based on this distribution function. From it, for each dark–matter halo the appropriate amount of galaxies, which corresponds to its normalizations within the limits declared in Chapter 3 is drawn randomly.

Galaxy Clusters on a Grid

To test the proper functionality of the filter 9 dark–matter halos with masses of $1 \times 10^{14}, 5 \times 10^{14}$ and $1 \times 10^{15} M_{\odot}$ and redshifts 0.3, 0.6 and 0.9 have been placed on a grid of the same field size as in the simulation of dark–matter halos. These redshifts are chosen such that for each redshift a specific combination of bands, specifically the color between these bands is the most appropriate choice, as stated in Section 3.1. The field size for the grid simulation has been chosen to 3×3 deg^2, for all galaxy clusters not to overlap.

Galaxies from Mass–function

The 409 random points from the mass–function as created according to Section 6.1 are not spatially correlated. On top of each of those dark–matter halos, a galaxy cluster is put. This means, that each galaxy cluster has its amount of galaxies distributed in redshift, magnitude and color according to its characteristic properties mass and redshift. According to the cluster model, all the dark–matter halos from the simulation host 36682 cluster galaxies. After removal of galaxies that fall outside of the specified limits 35408 remain. The field, by contrast consists of 556353 galaxies, such that no significant change in the density estimation is expected. This is especially the case because many of the cluster galaxies have statistics comparable to the field, as long as they are in the cluster outskirts.

At the example of one galaxy cluster with mass $M = 1 \times 10^{14} M_{\odot}$ and redshift $z_c = 0.6$ in redshift, observed within the i band with c_{r-i} color information, the simulated cluster is tested against the model. Within the chosen wide limits $\kappa_{\{r,z,c\}} = 5$ (see Section 5.3), the expected number of cluster galaxies is 92. The approach to test the simulated against the true distribution is very similar to the test of the dark–matter simulation from previous section. Because the cluster model is separable, it is sufficient to test each distribution individually. The best bin size is estimated from the cluster simulation within the specified limits. In each bin, the theoretical and the actually achieved number in the simulation are compared in terms of the χ^2–statistic. Table 8 summarizes the results for that example cluster. The resulting distributions can be seen in Figure 16. There, radial (top left), redshift (top right), magnitude (bottom left) and color (bottom right) histograms are plotted. The indicated errors are Poissonian in the corresponding bins. Further, it was explicitly tested that increasing the number of realizations the χ^2 tends towards zero, as expected for identical distributions.

Table 8: χ^2 values for the simulation to model comparison. The reduced χ^2 below one suggests that the simulations do represent the model distribution. The number of degrees of freedom is the amount of bins in the corresponding dimension. This proper bin size has been determined using the IQR approach.

	χ^2	d.o.f.
radial	21.42	36
redshift	27.89	72
magnitude	20.558	69
color	64.09	72

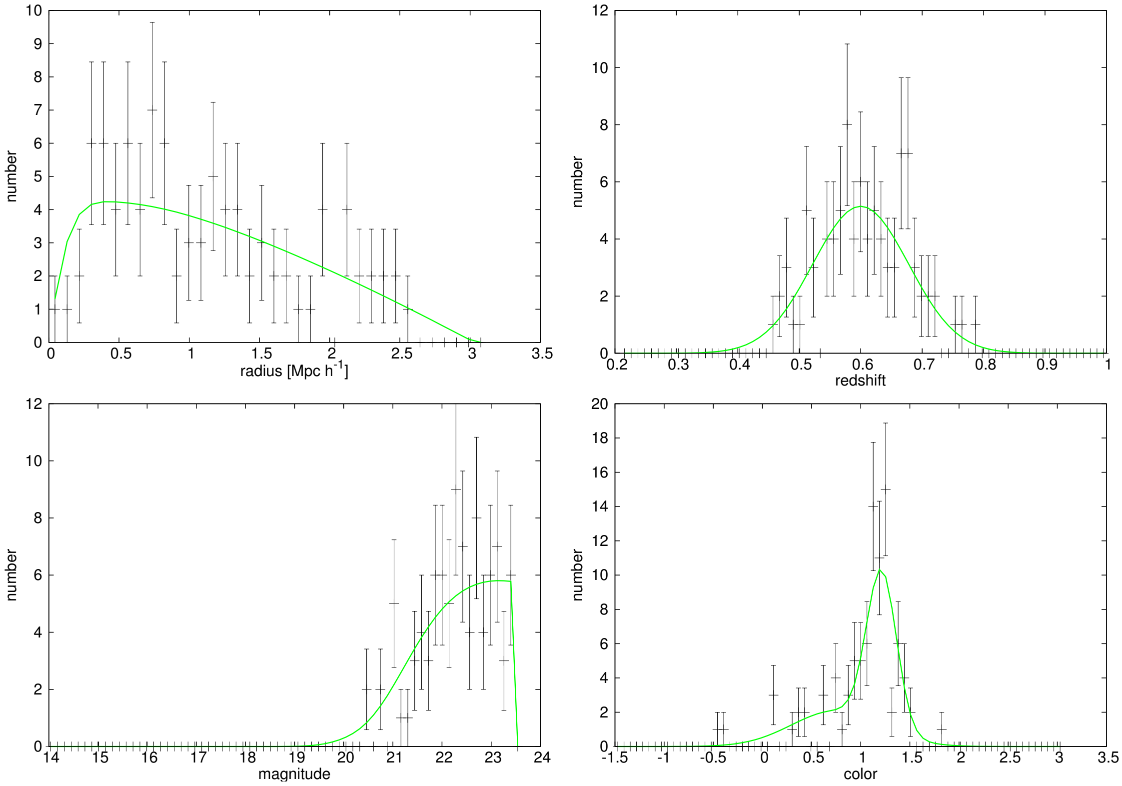

Figure 16: Comparison of model distributions with distributions from the simulation. Here only one example cluster is investigated. Radial (top left), redshift (top right), magnitude (bottom left) and color (bottom right) histograms are plotted. Poissonian errors are associated to each bin.

6.3 FIELD GALAXIES

In Chapter 5, the data has been separated into signal and noise parts. In the previous Section the simulation of 'signal' i. e. cluster galaxies has been discussed. Now the two different approaches from Chapter 4 are used to simulate 'noise' i. e. field galaxies.

To generate a sample of field galaxies according to the properties of an actual catalog, the galaxy properties can be drawn from the catalog itself. If one erases the radial information, i. e. assigns positions in right ascension and declination according to a flat distribution, one removes most of the structures in the catalog. It is allowed to have galaxies with the same optical properties (redshift and magnitudes) as long as their spatial positions are distinct.

In the Multi–Variate Gaussian case, there are routines to generate random numbers numerically. Usually a Cholesky decomposition of the covariance matrix is performed first, then an uncorrelated Gaussian random vector is correlated by projecting the decomposition matrix on the random vector. Here the C++ implementation from the TRNG[1] library has been used.

---

[1] Tina's Random Number Generator Library is available at http://numbercrunch.de/trng/

7

PREDICTIONS FOR SIGNAL TO NOISE MAPS

Suppose the underlying distribution of a data set is known. The variance, i. e. the r.m.s. may then serve as a scale for the percentage of data expected to exceed a certain value. The same principle can be used for data whose distribution is unknown, but the variance and hence the r.m.s. can be estimated. It becomes feasible to define percentages, which quantify the significance of outliers. This scale is usually set to $3\,\sigma$, which corresponds to a signal to noise ratio of 3. For a Gaussian distribution this means that 99.73% of all data have to be within $\pm 3\,\sigma$ region. This argumentation helps to decide if a proposed detection candidate can be considered as a real detection or not. Here two sorts of detection candidates, namely lousy (SN>3) and conservative (SN>5) are used to categorize detections. The detectability of a filter is predicted from mass–function maps on a redshift–mass grid as performed in Section 6.1 Chapter 6. The necessary SN maps are thus predicted on the same grid. This enables to relate SN values to predicted numbers of detections within redshift–mass regions. In this regard, the seven example filters from Section 5.6 Chapter 5 are evaluated on the same redshift–mass grid for their signal to noise. These seven filters depend on mass, redshift, band combination (except the redshift filter) and the underlying field distribution. Two different masses are used at every grid point. One corresponds to the grid point cluster mass, which implies that $\tau_m^{\text{fil}} = \tau_m^{\text{cl}}$. The second has been fixed to $5 \times 10^{14} M_\odot$, which implies that generally $\tau_m^{\text{fil}} \neq \tau_m^{\text{cl}}$. The fixed mass filter is useful in practice because one does not know the true, underlying cluster mass. Hereafter, the two signal estimates are named S^{true} & S^{fix}. They result from numerical integrations of Equation 32. Because of the strong redshift dependence in color and band dependence in general, the results are shown for three band combinations (g, r), (r, i) and (i, z). After having defined the strength estimates, the final ingredient in the SN maps is the noise term. As stated in Section 5.1, the noise term which is used to define the significance of a detections is the filter normalization, namely $N = \sigma_\Lambda = \sigma_{\Lambda,\text{mf}}$. Now, the two different SN ratios: SN^{true} and SN^{fix} can be measured at each grid point for each filter type.

In the following, the signal to noise maps are constructed for the MVG field galaxy distribution from Section 4.1 and for the distribution estimated from CARS data selection according to Section 4.2. The former serves the purpose to classify the agreement with the results from the filter application to the simulations as will be addressed in Section 8.2. This gives insight into the filter performance on a known field. The latter helps to classify the agreement with results to CARS data selection in Section 9.1. With these SN maps, the predicted detectability is fully quantified.

7.1 PREDICTIONS FOR MULTI–VARIATE GAUSSIAN FIELD GALAXY DENSITY

The following Figures show signal to noise maps of the seven filter combinations from Section 5.6, based on the MVG distribution as field galaxy input. The expected signal is

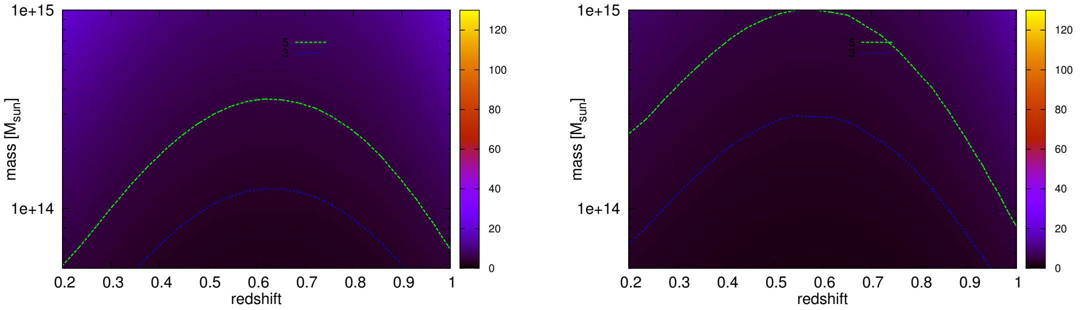

Figure 17: Signal to noise maps from the redshift filter based on MVG is shown for the actual cluster mass (left) and the fixed mass of $5 \times 10^{14} M_{\odot}$ (right). The contours correspond to SN values of 3 (blue) and 5 (teal) respectively. There is no bands dependence in the pure redshift filter. Used limits are $\kappa_r = 5, \kappa_z = 5$ and $\kappa_c = 5$.

somewhat exaggerated, because the cluster limits have been taken large. Namely: $\kappa_r = \kappa_z = \kappa_c = 5$. Such high limits are not realistic, as the galaxy distribution for $\kappa_r \approx 2$ already tends towards that of the mean field. Also the noise term is influenced by the larger limits, but as it enters the SN ratio with a square root, the SN values are artificially enhanced in this synthetic MVG case.

The redshift filter (Fig. 17) is the only example where the observed bands do not add any information to the filter. Thus, other color filters are not shown. The drop in SN around redshift 0.6 is due to the field galaxy density, which is high around this redshift.

The redshift filter has a very wide redshift width of ≈ 0.076 as a result of the estimated photometric redshift in the CARS selection. In principle, better constraints on the redshift would lead to a significant improvement in the redshift filter. But unfortunately, the photometric redshift estimation is not there yet. Despite the large width of the filter, it results in more detections than the single magnitude filter, which is indicated by the lower SN contours in Figures 17 and 18. The best single observable filter is the color filter, which is shown in Figure 19.

Table 9: Optimal redshift ranges for c_{g-r}, c_{r-i} and c_{i-z} colors after evaluation of color–filter.

redshift	color
$0.1 - 0.5$	c_{g-r}
$0.5 - 0.8$	c_{r-i}
$0.8 - 1.0$	c_{i-z}

The resulting SN maps can be seen in Figure 19. The evaluation of all three colors supports a new optimal redshift range for the individual colors. Table 9 summarizes these findings. Although the figures suggest that c_{g-r} is sufficient and performs best over the whole range, this must be treated with care, as will be explained below.

Some quantitative results are shown for redshift and mass binned samples in Tables 11 and 10 respectively.

Table 10: For the synthetic MVG field, the tables show predicted completeness (in %) of detected objects in mass bins. These bins contain either low $M_l = (0.5 - 0.7) \times 10^{14} M_\odot$, medium $M_m = (0.7 - 1) \times 10^{14} M_\odot$ or high $M_h = (1 - 10) \times 10^{14} M_\odot$ mass objects. The corresponding numbers of objects falling in these bins for a 9 deg^2 field are 207, 110.68 and 91.32 respectively. From top to bottom, results from filters with information in the $(r, g), (i, r)$ and (z, i) bands are shown. The filters in the very left column are the 7 possible combinations with the available observables. The subscripts 3 and 5 represent the lousy and conservative detectability threshold in the SN ratio.

	M_l^3	M_m^3	M_h^3	M_l^5	M_m^5	M_h^5
Filters in (r,g)						
Red	26.33	47.05	90.07	1.40	6.37	29.78
Mag	21.01	38.05	72.89	8.97	12.63	28.27
Col	98.56	99.35	100.00	96.73	96.81	98.18
RedMag	47.42	75.01	100.00	14.47	25.59	50.77
RedCol	100.00	100.00	100.00	100.00	100.00	100.00
MagCol	100.00	100.00	100.00	100.00	100.00	100.00
RedMagCol	100.00	100.00	100.00	100.00	100.00	100.00
Filters in (i,r)						
Red	26.33	47.05	90.07	1.40	6.37	29.78
Mag	18.31	33.07	71.51	8.97	12.63	27.26
Col	43.78	58.53	75.80	12.38	20.41	37.64
RedMag	46.27	76.02	100.00	15.58	24.14	53.05
RedCol	100.00	100.00	100.00	56.40	85.90	100.00
MagCol	100.00	100.00	100.00	28.51	54.19	91.36
RedMagCol	100.00	100.00	100.00	84.42	100.00	100.00
Filters in (z,i)						
Red	26.33	47.05	90.07	1.40	6.37	29.78
Mag	19.43	29.00	70.49	8.97	13.65	28.24
Col	32.98	38.39	65.69	22.05	23.47	27.03
RedMag	59.64	95.60	100.00	16.85	30.05	60.92
RedCol	91.45	100.00	100.00	42.48	53.10	83.35
MagCol	68.04	93.52	100.00	41.37	47.46	68.79
RedMagCol	100.00	100.00	100.00	58.37	75.82	100.00

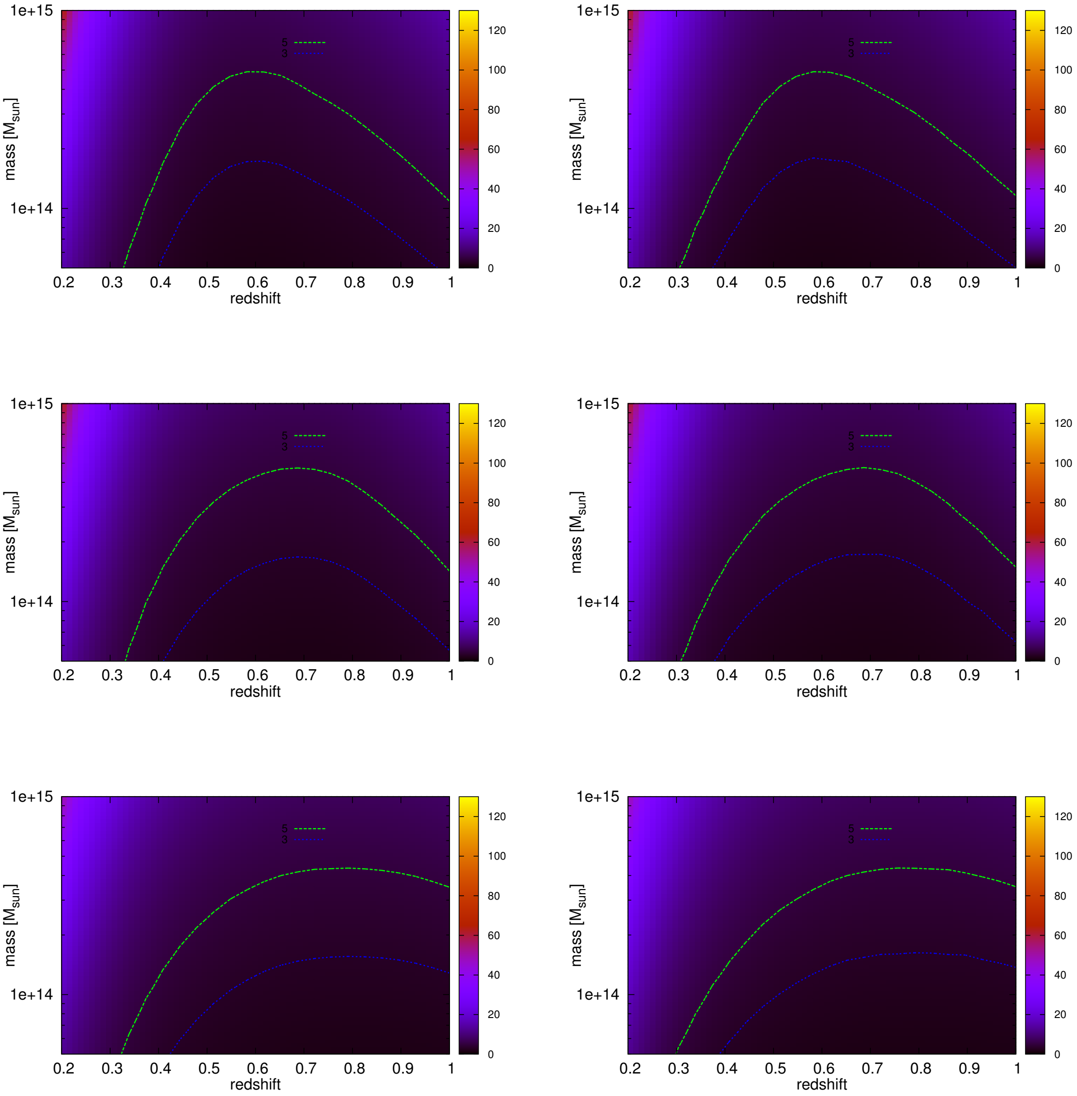

Figure 18: Signal to noise maps from the magnitude filter based on MVG is shown for the actual cluster mass (left) and the fixed mass of $5 \times 10^{14} M_{\odot}$ (right). The contours correspond to SN values of 3 (blue) and 5 (teal) respectively. Used limits are $\kappa_r = 5$, $\kappa_z = 5$ and $\kappa_c = 5$.

Table 11: For the synthetic MVG field, the tables show predicted completeness (in %) of detected objects in redshift bins. These bins contain either low $Z_l = [0.1 - 0.5)$, medium $Z_m = [0.5 - 0.8)$ or high $Z_h = [0.8 - 1]$ redshifts objects. The corresponding numbers of objects falling in these bins for a 9 deg^2 field are 121.39, 191.22 and 96.84 respectively. From top to bottom results from filters with information in the $(r, g), (i, r)$ and (z, i) bands are shown. The filters in the very left column are the 7 possible combinations with the available observables. The subscripts 3 and 5 represent the lousy and conservative detectability threshold in the SN ratio.

	Z_l^3	Z_m^3	Z_h^3	Z_l^5	Z_m^5	Z_h^5
Filters in (r,g)						
Red	72.06	17.69	69.88	21.98	0.95	8.98
Mag	74.84	9.31	45.06	44.59	0.39	3.70
Col	96.94	100.00	100.00	90.13	100.00	100.00
RedMag	94.55	34.39	95.21	61.52	2.69	25.74
RedCol	100.00	100.00	100.00	100.00	100.00	100.00
MagCol	100.00	100.00	100.00	100.00	100.00	100.00
RedMagCol	100.00	100.00	100.00	100.00	100.00	100.00
Filters in (i,r)						
Red	72.06	17.69	69.88	21.98	0.95	8.98
Mag	82.38	9.58	22.30	45.70	0.38	1.37
Col	10.78	79.52	61.66	0.57	39.73	6.24
RedMag	100.00	38.02	79.92	72.73	3.25	13.48
RedCol	100.00	100.00	100.00	57.19	95.54	52.99
MagCol	100.00	100.00	100.00	57.44	57.98	22.72
RedMagCol	100.00	100.00	100.00	94.24	100.00	73.85
Filters in (z,i)						
Red	72.06	17.69	69.88	21.98	0.95	8.98
Mag	85.71	13.90	6.40	47.69	0.79	0.16
Col	6.92	34.36	100.00	0.33	3.93	91.42
RedMag	100.00	56.11	95.21	74.98	5.24	23.61
RedCol	100.00	90.73	100.00	70.92	20.98	100.00
MagCol	97.01	63.48	100.00	60.76	16.00	100.00
RedMagCol	100.00	100.00	100.00	94.55	44.32	100.00

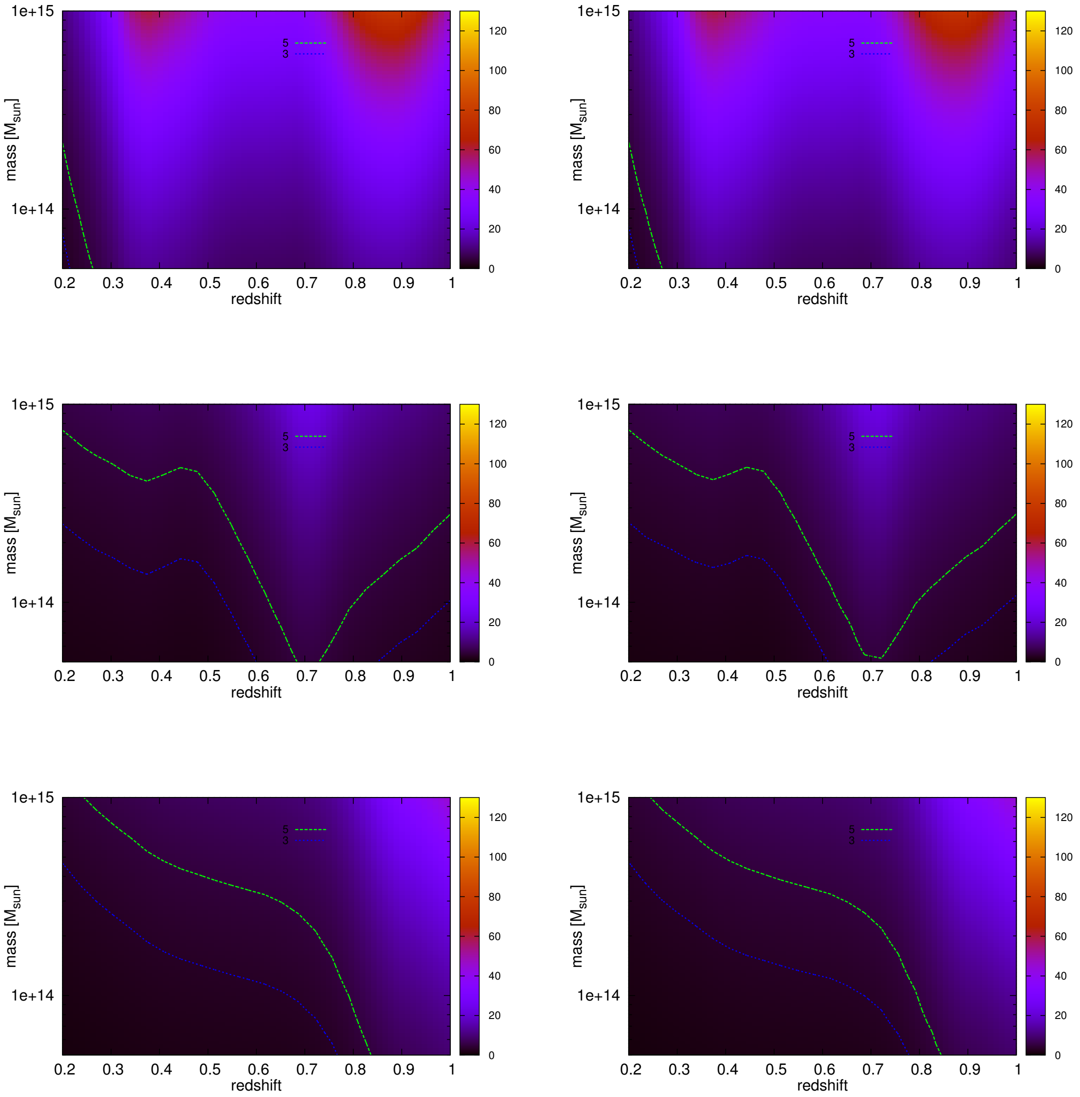

Figure 19: Signal to noise maps from the color filter based on MVG is shown for the actual cluster mass (left) and the fixed mass of $5 \times 10^{14} M_{\odot}$ (right). The contours correspond to SN values of 3 (blue) and 5 (teal) respectively. Used limits are $\kappa_r = 5, \kappa_z = 5$ and $\kappa_c = 5$.

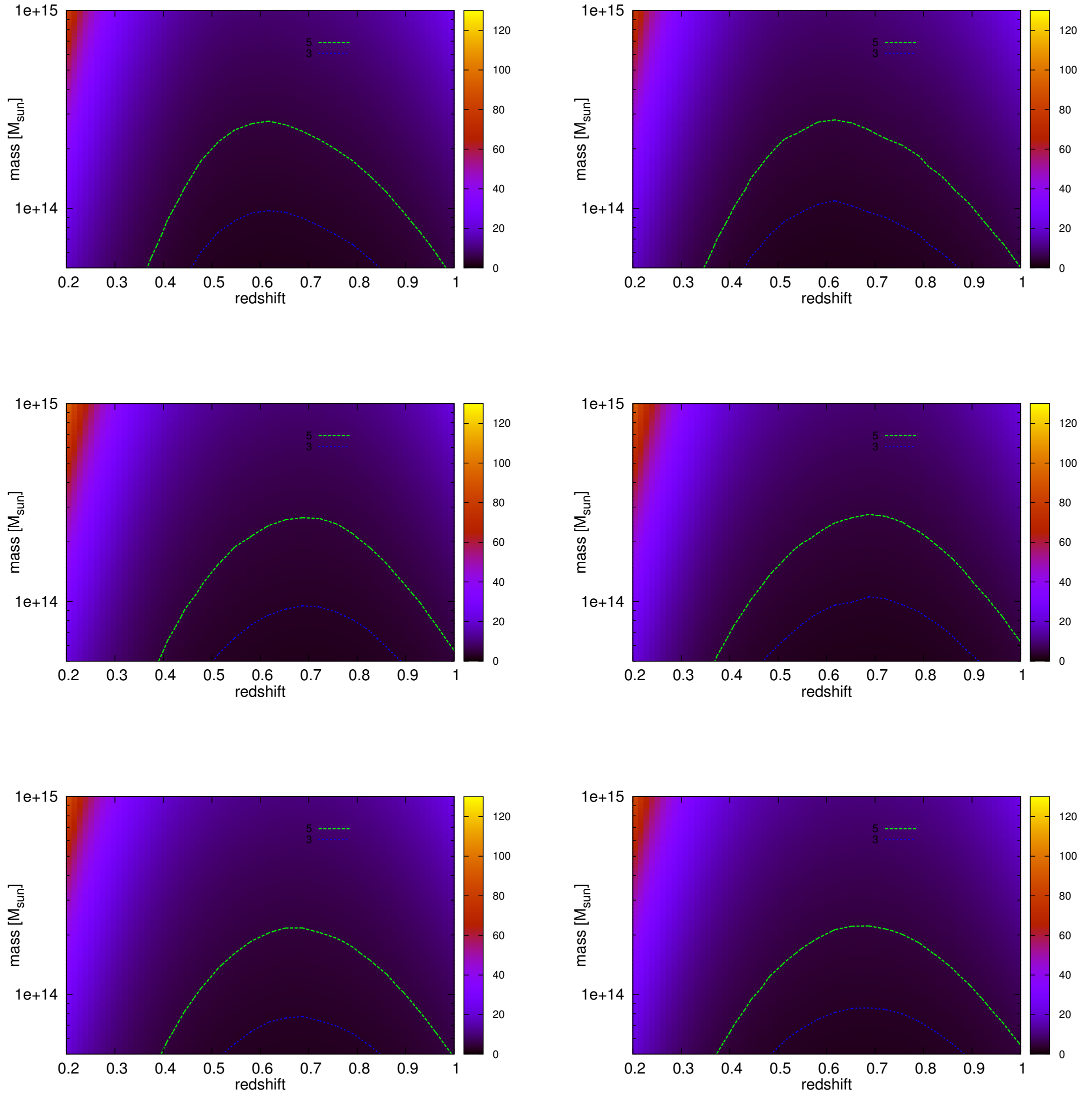

Figure 20: Signal to noise maps from the RedMag filter based on MVG is shown for the actual cluster mass (left) and the fixed mass of $5 \times 10^{14} M_{\odot}$ (right). The contours correspond to SN values of 3 (blue) and 5 (teal) respectively. Used limits are $\kappa_r = 5, \kappa_z = 5$ and $\kappa_c = 5$.

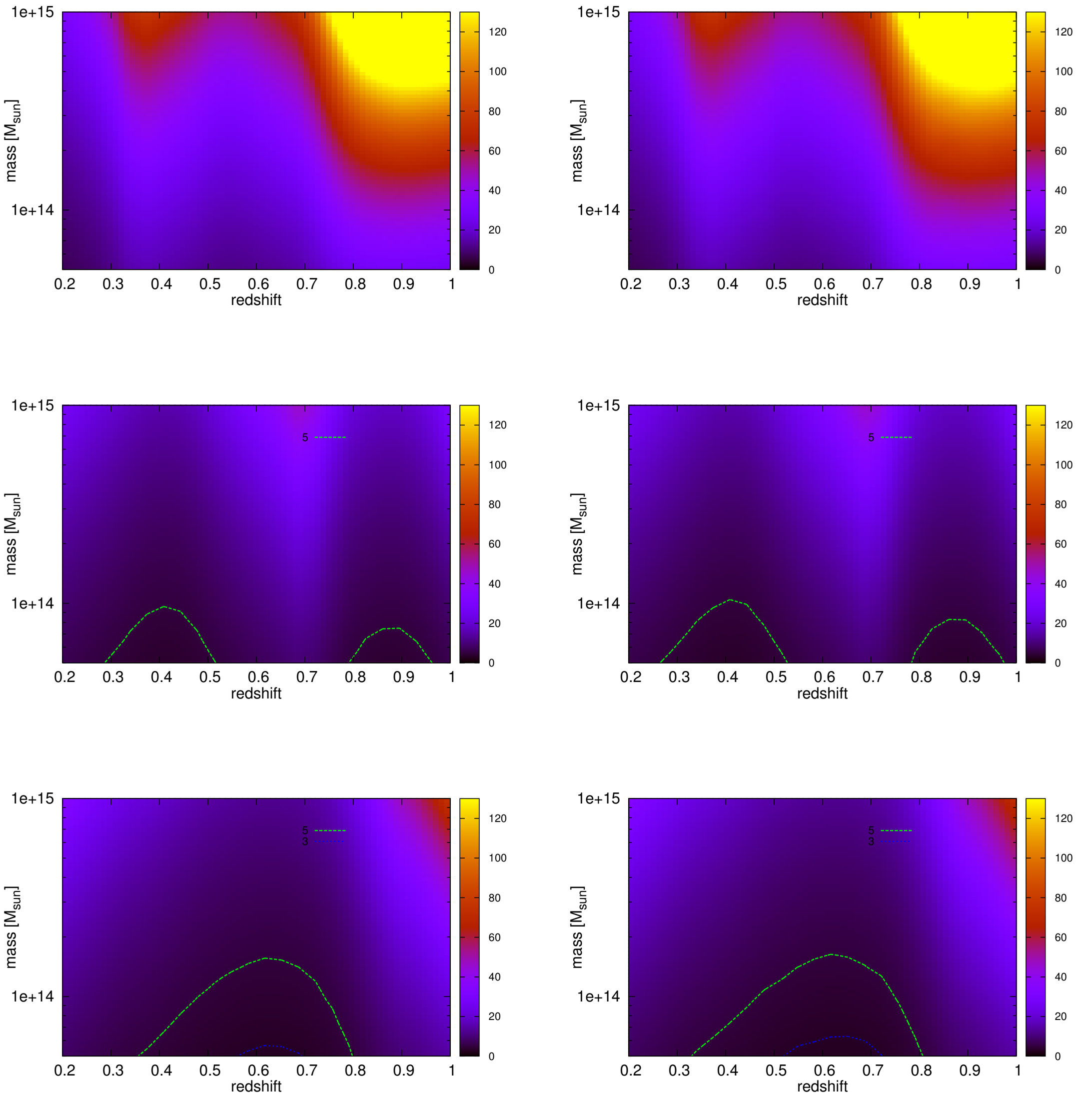

Figure 21: Signal to noise maps from the RedCol filter based on MVG is shown for the actual cluster mass (left) and the fixed mass of $5 \times 10^{14} M_{\odot}$ (right). The contours correspond to SN values of 3 (blue) and 5 (teal) respectively. Used limits are $\kappa_r = 5$, $\kappa_z = 5$ and $\kappa_c = 5$.

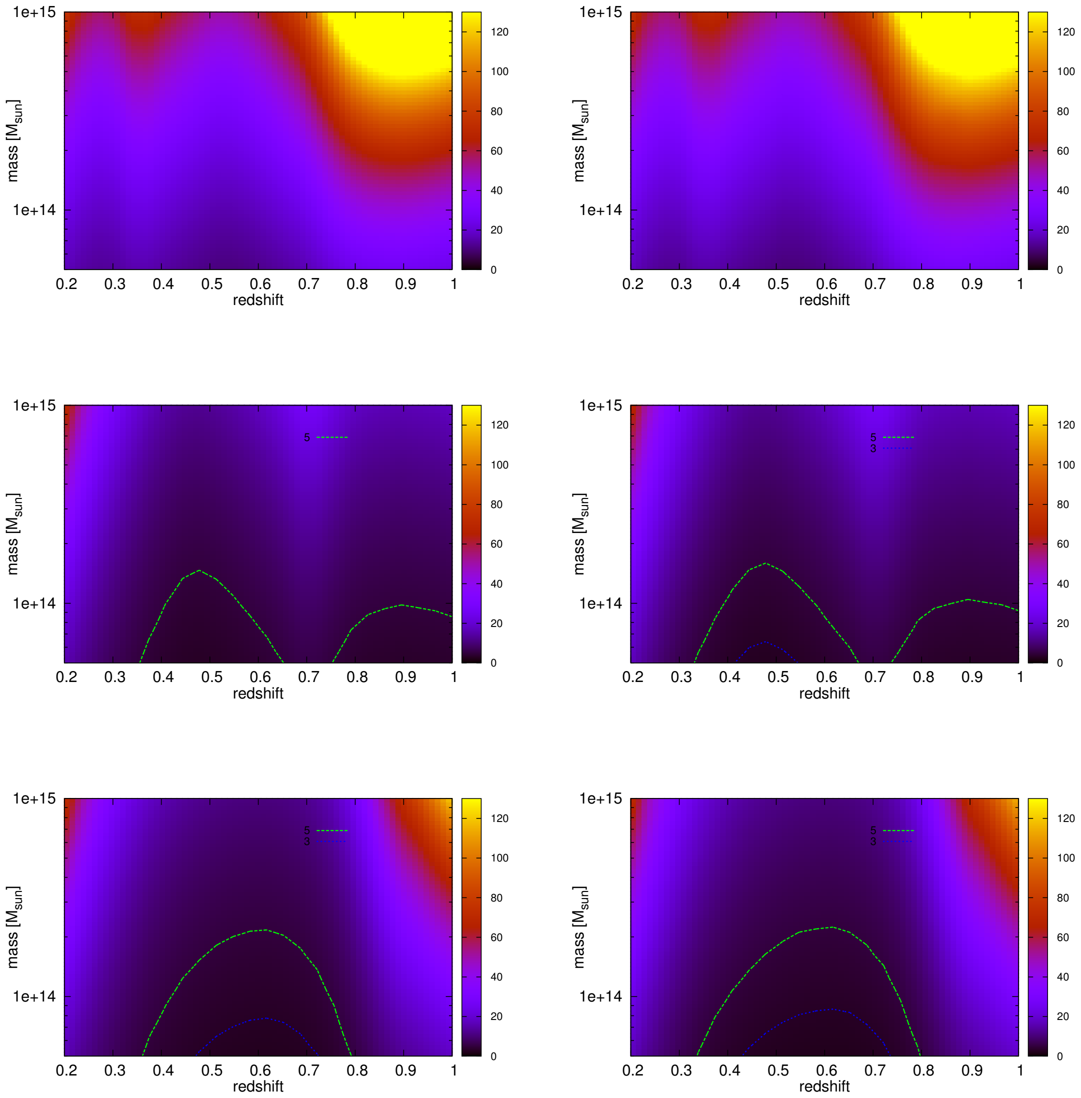

Figure 22: Signal to noise maps from the MagCol filter based on MVG is shown for the actual cluster mass (left) and the fixed mass of $5 \times 10^{14} M_{\odot}$ (right). The contours correspond to SN values of 3 (blue) and 5 (teal) respectively. Used limits are $\kappa_r = 5, \kappa_z = 5$ and $\kappa_c = 5$.

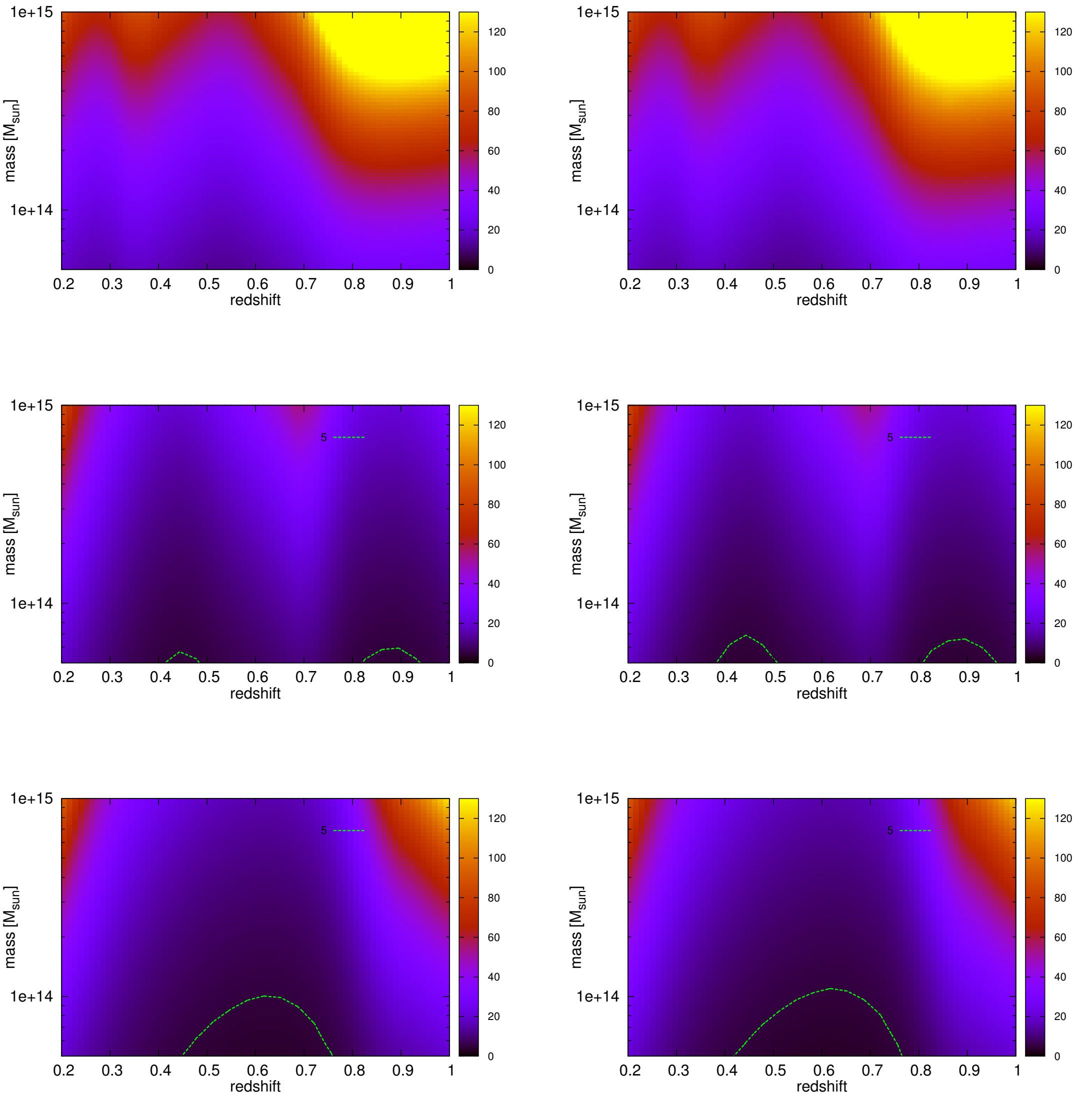

Figure 23: Signal to noise maps from the RedMagCol filter based on MVG is shown for the actual cluster mass (left) and the fixed mass of $5 \times 10^{14} M_\odot$ (right). The contours correspond to SN values of 3 (blue) and 5 (teal) respectively. Used limits are $\kappa_r = 5, \kappa_z = 5$ and $\kappa_c = 5$.

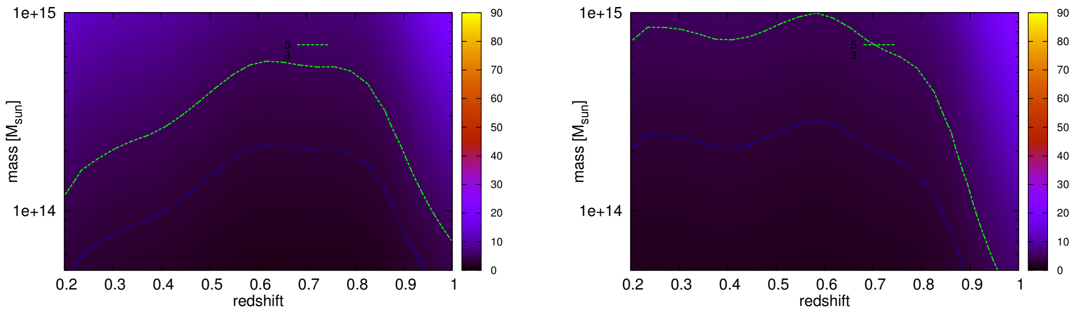

Figure 24: SN maps on a redshift–mass grid from the redshift filter based on the selected CARS catalog. Actual cluster mass (left) and the fixed mass of $5 \times 10^{14} M_{\odot}$ (right) has been used for the filter initialization. The contours correspond to SN values of 3 (blue) and 5 (teal) respectively. The filter limits have been set to $\kappa_r = 1, \kappa_z = 2$ and $\kappa_c = 5$.

7.2 PREDICTIONS FOR FIELD GALAXY DENSITY ESTIMATED FROM CARS W1MOP1 FIELD

Here the signal to noise (SN) maps of the seven filter combination from Section 5.6 are constructed and shown for the density estimated from the selected CARS catalog directly. The filter limits have been adjusted to $\kappa_r = 1, \kappa_z = 2$ and $\kappa_c = 5$, which corresponds realistic volume of galaxy clusters. Quantitative results are shown for redshift and mass binned samples in Tables 13 and 12 respectively. Thereafter, it is expected to find

7.3 CONCLUSIONS

Two important observations could be made in the previous two sections. First, that r, g band combination performs tremendously well. Second, even at high redshifts the signal to noise seems to be very high. Both findings rest on the usage of data that is not complete above a certain magnitude. The (r,g) band filter would perform best, if the galaxy completeness in magnitude would be high in real data. The completeness limit for the r band is roughly 25 mag. Therefore, it is not usable in practice for high redshifts as magnitudes rise above the completeness limit.

Second, the large SN ratios at high redshift are a consequence of the Gaussian redshift drop off for field galaxies. This feature is purely artificial and needs also to be taken into account by reducing the filter limits according to the survey completeness limitations. The distribution in the cluster model is normalized to these larger limits and the filter therefore expects more galaxies than the field alone cannot provide. In theory the signal to noise values are hight, but in practice will the small number of galaxies at this redshift yield low signal to noise ratios. One could avoid the somewhat inaccurate predictions, by applying magnitude completeness cuts in the simulation also. Still, the filter computes the signal to noise values as expected for this synthetic field.

For the W1mop1 field, the relevance of proper colors can be inferred from Table 13. The single color filter achieves high completeness if applied in the proper redshift range.

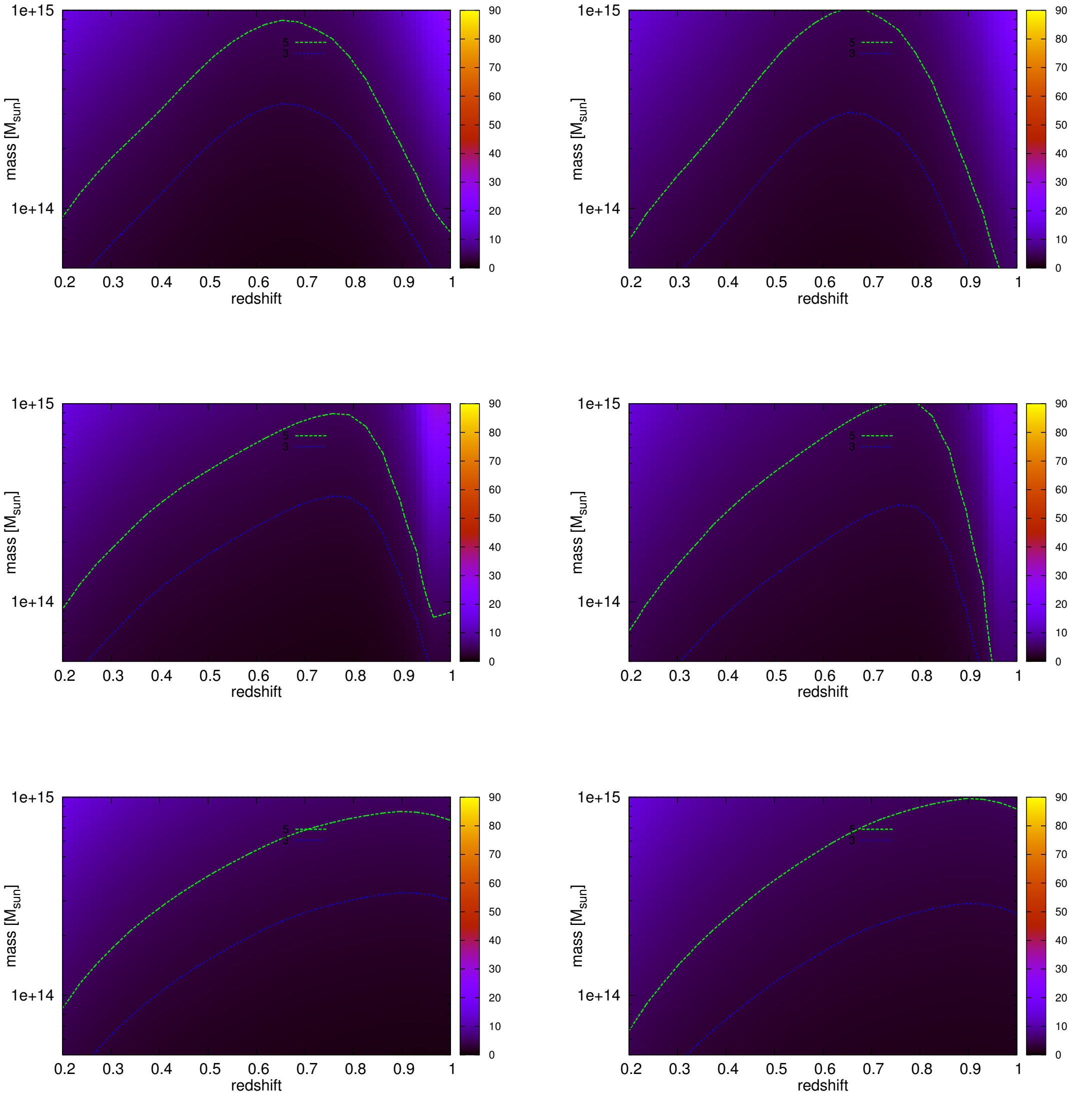

Figure 25: SN maps on a redshift–mass grid from the magnitude filter based on the selected CARS catalog. Actual cluster mass (left) and the fixed mass of $5 \times 10^{14} M_{\odot}$ (right) has been used for the filter initialization. The contours correspond to SN values of 3 (blue) and 5 (teal) respectively. The filter limits have been set to $\kappa_r = 1, \kappa_z = 2$ and $\kappa_c = 5$.

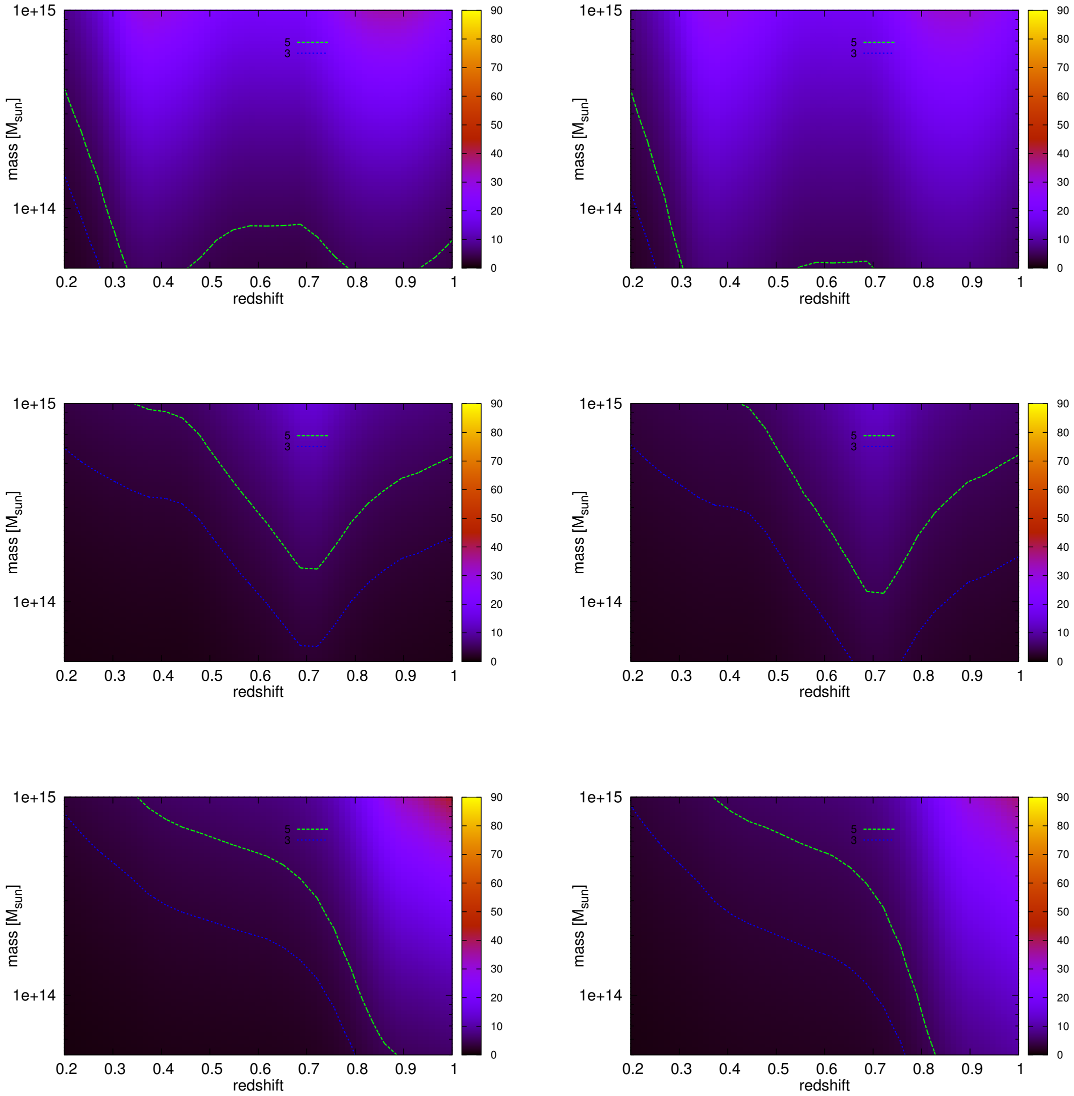

Figure 26: SN maps on a redshift–mass grid from the color filter based on the selected CARS catalog. Actual cluster mass (left) and the fixed mass of $5 \times 10^{14} M_{\odot}$ (right) has been used for the filter initialization. The contours correspond to SN values of 3 (blue) and 5 (teal) respectively. The filter limits have been set to $\kappa_r = 1, \kappa_z = 2$ and $\kappa_c = 5$.

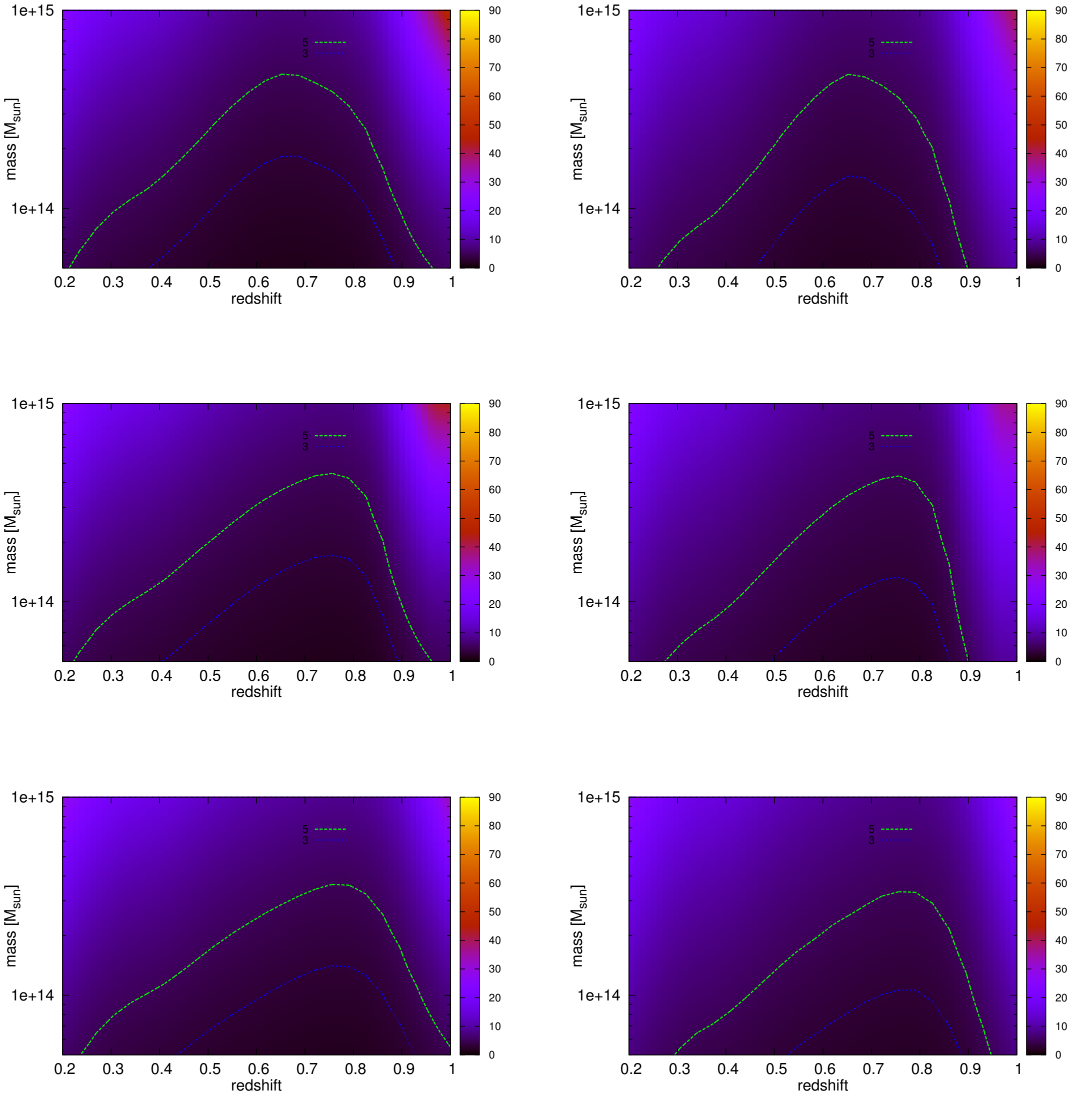

Figure 27: SN maps on a redshift–mass grid from the RedMag filter based on the selected CARS catalog. Actual cluster mass (left) and the fixed mass of $5 \times 10^{14} M_{\odot}$ (right) has been used for the filter initialization. The contours correspond to SN values of 3 (blue) and 5 (teal) respectively. The filter limits have been set to $\kappa_r = 1, \kappa_z = 2$ and $\kappa_c = 5$.

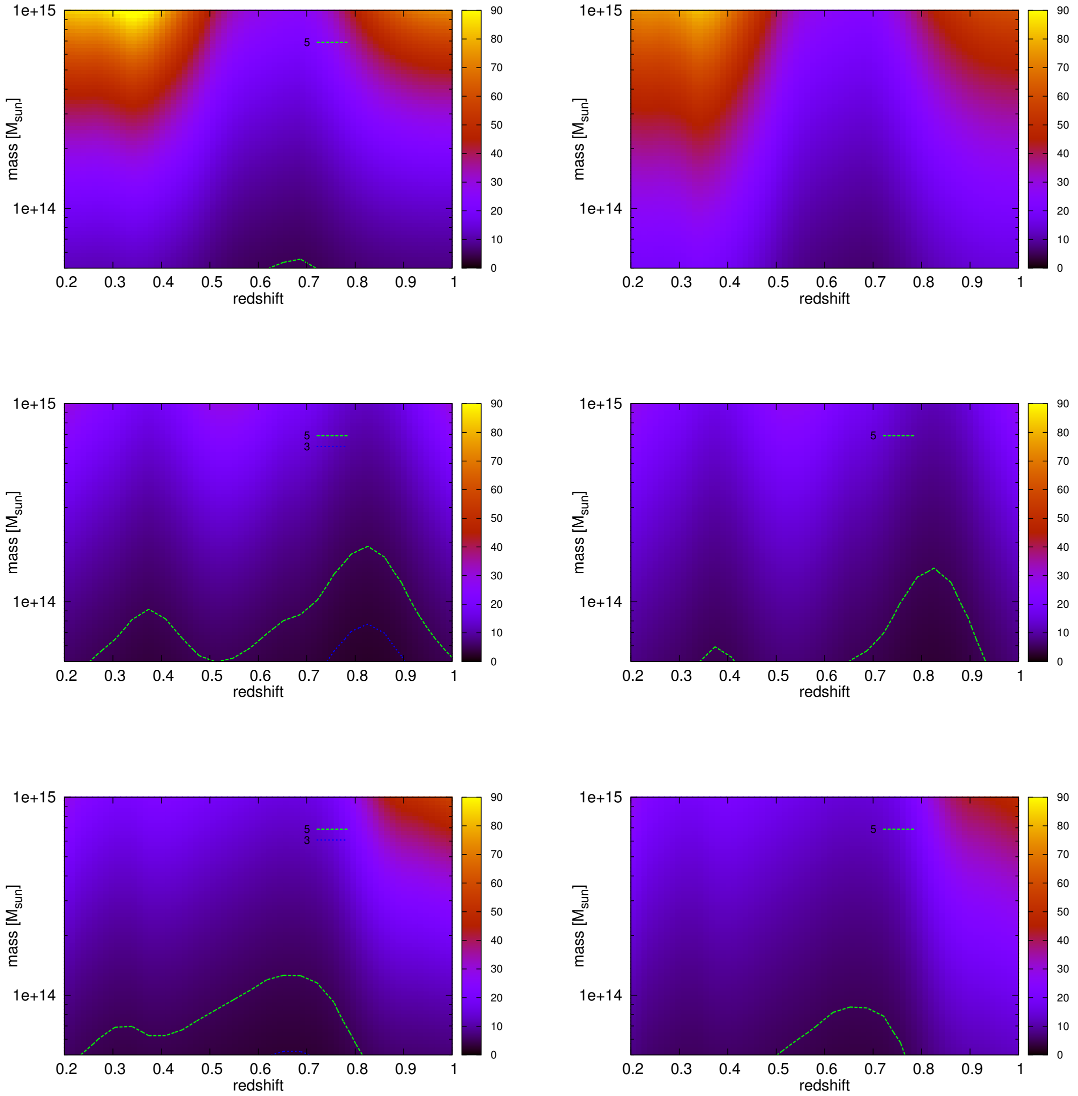

Figure 28: SN maps on a redshift–mass grid from the RedCol filter based on the selected CARS catalog. Actual cluster mass (left) and the fixed mass of $5 \times 10^{14} M_\odot$ (right) has been used for the filter initialization. The contours correspond to SN values of 3 (blue) and 5 (teal) respectively. The filter limits have been set to $\kappa_r = 1, \kappa_z = 2$ and $\kappa_c = 5$.

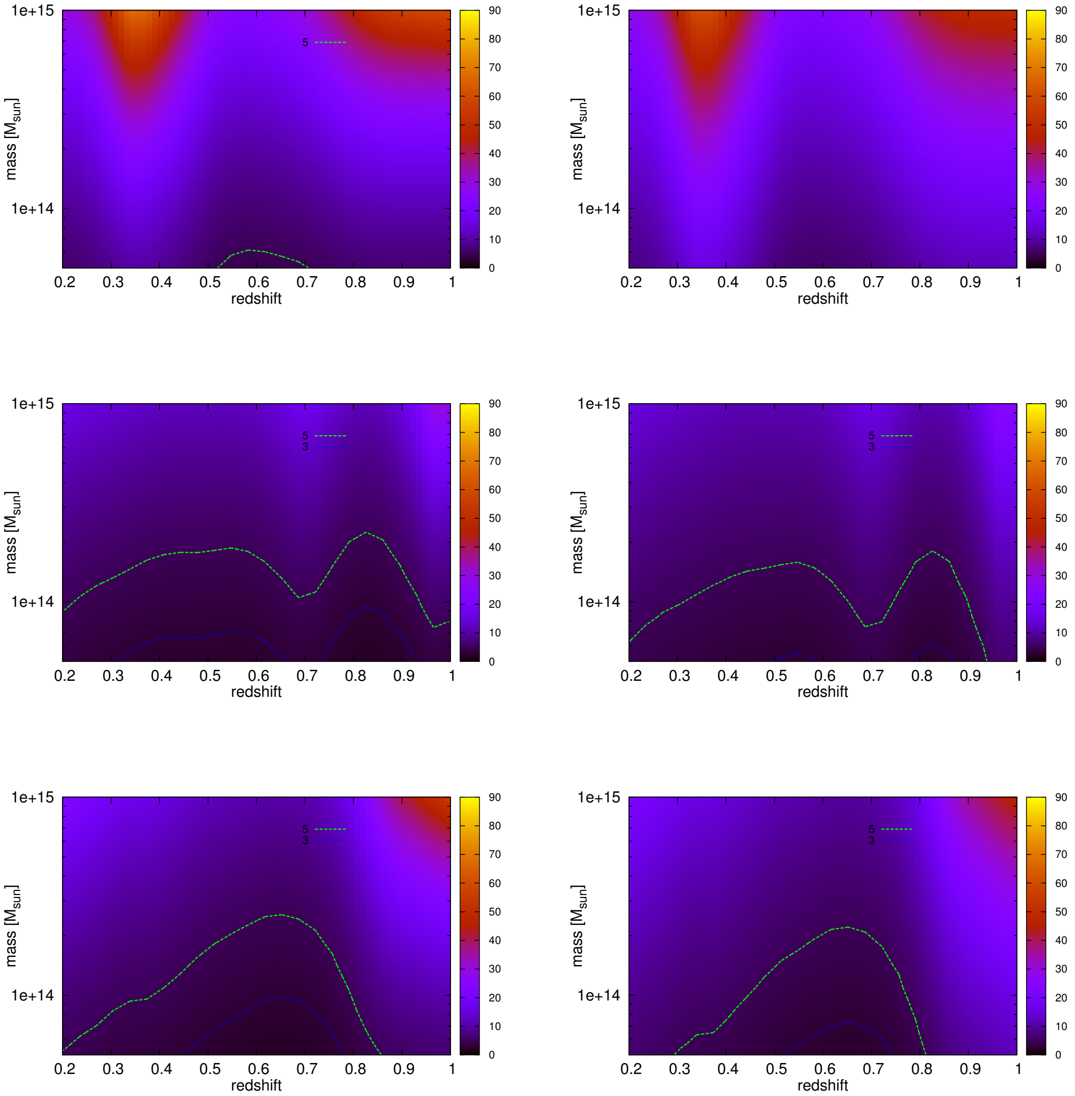

Figure 29: SN maps on a redshift–mass grid from the MagCol filter based on the selected CARS catalog. Actual cluster mass (left) and the fixed mass of $5 \times 10^{14} M_\odot$ (right) has been used for the filter initialization. The contours correspond to SN values of 3 (blue) and 5 (teal) respectively. The filter limits have been set to $\kappa_r = 1, \kappa_z = 2$ and $\kappa_c = 5$.

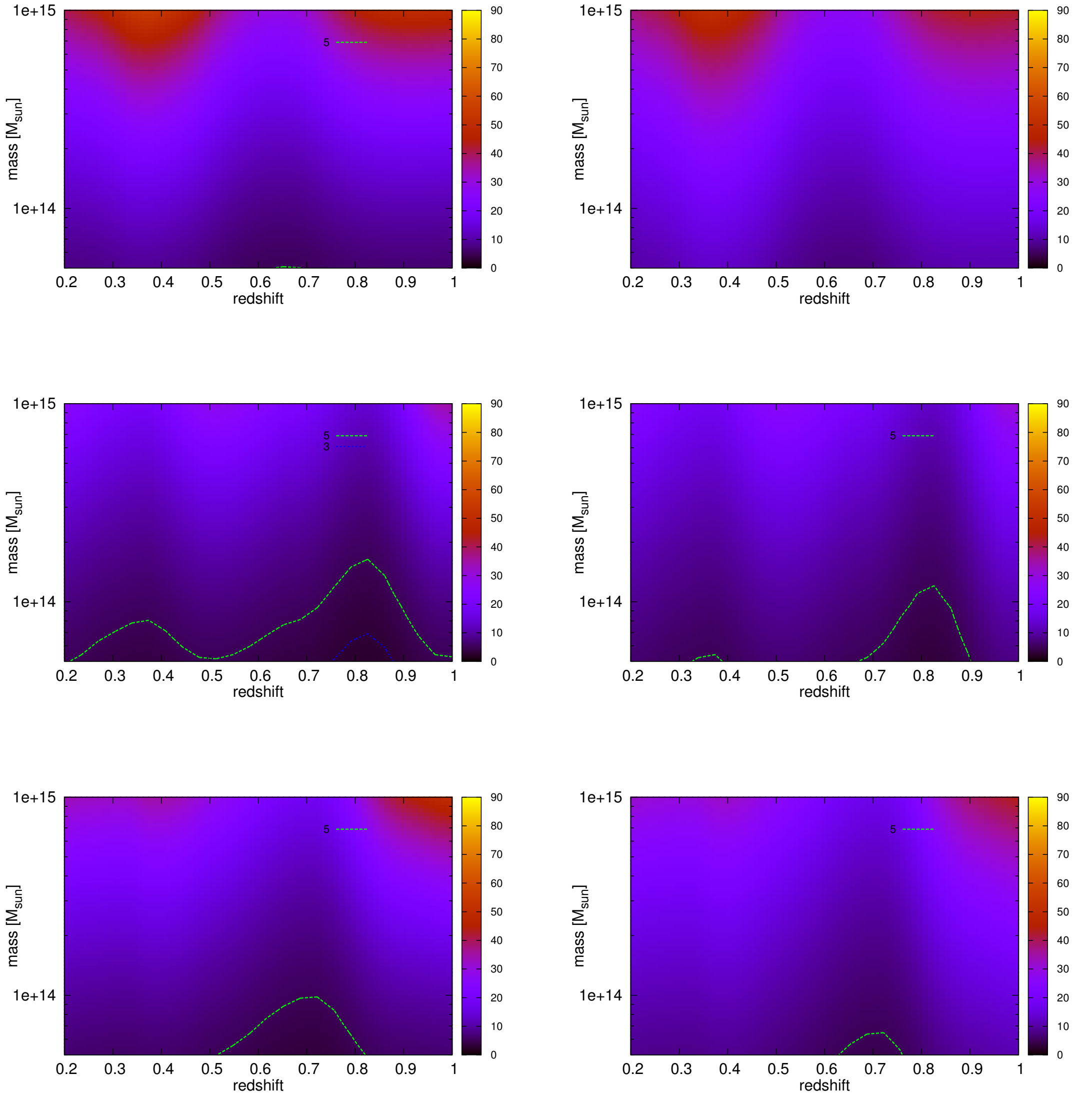

Figure 30: SN maps on a redshift–mass grid from the RedMagCol filter based on the selected CARS catalog. Actual cluster mass (left) and the fixed mass of $5 \times 10^{14} M_{\odot}$ (right) has been used for the filter initialization. The contours correspond to SN values of 3 (blue) and 5 (teal) respectively. The filter limits have been set to $\kappa_r = 1, \kappa_z = 2$ and $\kappa_c = 5$.

Table 12: For CARS data selection, the tables show predicted completeness (in %) of detected objects in mass bins. These bins contain either low $M_l = [0.5 - 0.7) \times 10^{14} M_\odot$, medium $M_m = [0.7 - 1) \times 10^{14} M_\odot$ or high $M_h = [1 - 10] \times 10^{14} M_\odot$ mass objects. The corresponding numbers of objects falling in these bins for a 9 deg^2 field are 207, 110.68 and 91.32 respectively. From top to bottom, results from filters with information in the $(r, g), (i, r)$ and (z, i) bands are shown. The filters in the very left column are the 7 possible combinations with the available observables. The subscripts 3 and 5 represent the lousy and conservative detectability threshold in the SN ratio.

	M_l^3	M_m^3	M_h^3	M_l^5	M_m^5	M_h^5
			Filters in (r,g)			
Red	8.22	21.17	55.92	0.00	1.06	13.91
Mag	9.59	21.32	44.82	0.00	0.47	14.28
Col	95.86	96.81	98.82	47.81	81.78	93.62
RedMag	30.88	46.13	74.75	8.22	14.16	36.33
RedCol	100.00	100.00	100.00	95.61	100.00	100.00
MagCol	100.00	100.00	100.00	82.75	100.00	100.00
RedMagCol	100.00	100.00	100.00	95.61	100.00	100.00
			Filters in (i,r)			
Red	9.89	22.72	55.92	0.00	1.06	13.93
Mag	9.59	17.11	44.12	0.00	2.94	13.16
Col	2.90	16.91	45.17	0.00	0.00	6.98
RedMag	33.24	47.28	77.72	7.52	15.97	40.12
RedCol	79.34	97.89	100.00	16.98	54.38	86.11
MagCol	35.81	90.43	100.00	0.00	2.94	47.81
RedMagCol	84.34	100.00	100.00	16.94	64.96	90.81
			Filters in (z,i)			
Red	8.22	21.17	55.92	0.00	1.06	13.73
Mag	5.36	12.32	40.75	0.00	0.47	10.07
Col	29.28	29.97	40.47	18.42	21.36	21.84
RedMag	32.04	52.43	88.70	3.90	13.34	41.70
RedCol	95.61	100.00	100.00	32.65	60.32	92.72
MagCol	56.58	78.66	100.00	22.03	33.51	60.71
RedMagCol	100.00	100.00	100.00	63.25	81.01	100.00

Table 13: For CARS data selection, the tables show predicted completeness (in %) of detected objects in redshift bins. These bins contain either low $Z_l = [0.1 - 0.5)$, medium $Z_m = [0.5 - 0.8)$ or high $Z_h = [0.8 - 1]$ redshifts objects. The corresponding numbers of objects falling in these bins for a 9 deg^2 field are 121.39, 191.22 and 96.84 respectively. From top to bottom, results from filters with information in the (r, g), (i, r) and (z, i) bands are shown. The filters in the very left column are the 7 possible combinations with the available observables. The subscripts 3 and 5 represent the lousy and conservative detectability threshold in the SN ratio.

	Z_l^3	Z_m^3	Z_h^3	Z_l^5	Z_m^5	Z_h^5
Filters in (r,g)						
Red	38.25	4.68	37.42	6.09	0.16	6.45
Mag	39.49	1.57	34.62	7.53	0.04	4.54
Col	89.13	100.00	100.00	71.51	50.15	95.54
RedMag	79.14	9.62	71.21	25.52	0.67	34.81
RedCol	100.00	100.00	100.00	100.00	95.24	100.00
MagCol	100.00	100.00	100.00	100.00	81.29	100.00
RedMagCol	100.00	100.00	100.00	100.00	95.24	100.00
Filters in (i,r)						
Red	38.25	4.68	42.74	6.09	0.16	6.45
Mag	39.83	2.42	27.05	7.22	0.07	6.64
Col	1.51	30.52	6.06	0.03	3.23	0.21
RedMag	84.89	13.71	65.10	31.07	1.09	31.13
RedCol	100.00	91.62	69.88	62.72	43.27	15.70
MagCol	72.85	66.03	52.70	14.41	9.72	11.26
RedMagCol	100.00	93.18	79.92	63.54	43.76	30.16
Filters in (z,i)						
Red	38.25	4.68	37.42	6.09	0.16	6.26
Mag	45.13	3.59	0.39	7.83	0.14	0.00
Col	1.72	16.72	100.00	0.04	1.62	81.24
RedMag	91.78	22.65	52.49	37.51	2.32	11.37
RedCol	100.00	95.24	100.00	61.34	25.06	100.00
MagCol	94.55	44.02	100.00	35.00	5.33	88.39
RedMagCol	100.00	100.00	100.00	100.00	49.15	100.00

The (g,r) band combination suffers from the magnitude cutting as explained above. The signal to noise rates and hence the completeness rates are thus exaggerated.

Overall does the `RedMagCol` perform best for all ranges. This is not surprising as it takes advantage of information from each observable.

8

APPLICATION OF FILTER TO SIMULATIONS

The most promising (from Ch. 7) of the introduced filters (Sec. 5.6) is applied to the grid simulation and the simulation from a mass–function catalogs. Based on these simulations and limiting parameters $\kappa_r = \kappa_z = \kappa_c = 5$ the filter limits are adjusted as explained in Section 5.3. The filter is initialized at each redshift slice from 0.1 to 1.0 in steps of $dz = 0.05$ steps. The mass in the filter is fixed to $5 \times 10^{14} M_\odot$. At each redshift slice, the filter is then applied to the catalog in the following way. First, the whole field is segmented into cells, which are based on the full width half maximum (FWHM) of the angular filter. The user decides how many cells shall cover the FWHM range. Here, 3 cells within FWHM have been chosen to define the cell size. Each cells lower left corner is now a potential detection candidate. The filter is evaluated at each galaxy within the filter volume around the detection candidate. This is the approximation of the integral in Equation 32, i. e. the biased signal estimate. The map of detection candidates together with their biased signal estimate, detection significance and error of the richness estimation are stored into FITS files.

8.1 APPLICATION TO THE GRID SIMULATION

In fact there are three filters applied to the grid simulation. Each filter is constructed using band combination corresponding to the targeted redshift. The redshifts are plotted from top to bottom in ascending order 0.3, 0.6 and 0.9. This test, serves the purpose to find out if the filter performs as expected. In this test, the filter is expected to find all the simulated clusters if applied to cluster catalogs only, with the right signal strength estimates. Also, is the filter expected to find no clusters if applied to field catalog only. If applied to combination of cluster and field catalogs, the filter shall find all clusters. In Table 14 the expected and measured values (at correct redshift) from the application to field+cluster catalog on the example of the (r,g) filter are juxtaposed. The 1–σ errors ($\sqrt{\Lambda_{est}}\sigma_{cl}$) for the richness estimate are assigned by the filter. The measured richness, variance of the field and the mean background are in good agreement with predicted values. The output map for the (r,g) band combination is shown in Figure 31. Here the population in the field as well as in the clusters has been enlarged by a factor of 10 to investigate if based on better statistics the signal estimate would change significantly. It was confirmed that the richness estimate as well as background and variance are stable. On the left application to field galaxies, on the right to cluster galaxies and at the bottom plot to the combination is shown. As

Table 14: Estimated and expected signal, field variance and mean (r,g filter).

	Expected	Measured
Λ_{est}	388.702	416.578 ±42.95
σ_{fl}^2	68.61	66.67
$\bar{B}$	58.98	57.95

explained in previous Chapter the cluster sizes are somewhat exaggerated by means of high κ_r values which set the cutoff radius.

Estimate of Contamination

Having a catalog with field galaxies only allows for tests of contamination. Therefore, the filter as explained above is applied to the field catalog. Of course does one field not represent the true underlying distribution, but it still helps to estimate how many false positives one has to expect.

On the resulting redshift slices SExtractor[1] (Bertin and Arnouts, 1996), a software to identify and extract sources from FITS files in two dimensional data has been applied. The fixed detection threshold of 2.5 is set to identify detections. Only regions containing more than 9 pixels above the detection threshold are considered detection. The total number of detections in the field galaxy catalog was 159. Table 15 shows the remaining detections for lousy (147 detections) and conservative (15 detections) thresholds. This means, that roughly 16.3 and 1.6 false–positives deg^{-2} are expected for the two thresholds.

Table 15: Detections from (r,g) filter applied to the field without clusters.

	Detections
All	159
SN_{thr} - 3	147
SN_{thr} - 5	15

8.2 APPLICATION TO THE MASS–FUNCTION BASED SIMULATION

Here the *RedMagCol* filter has been applied to the catalog combining cluster and field galaxies from the simulation. Amongst others richness and signal to noise maps are created for each redshift slice. SExtractor is applied to those as explained above. The resulting detections are further divided into those having SN values above 3 and 5. Subsequently all detections above a the SN threshold are tested for the relation to clusters. For this purpose a tube along redshift with the extent of $[0.1 - z : z + 0.1]$ and radius $2 \times R_{200}$ of the detection is defined. If galaxy clusters are found within the tube for a detection, this detection is regarded as candidate. The same procedure is also performed after inverting the roles of detections and clusters. If now detections are found within the tube (here the tube size is fixed by detection, not by the cluster) of the cluster, the cluster is considered detected. The choice for the tube size is based on the fact that most cluster members are located in this region. The elongation of the cluster in redshift has been set to $5 \times \sigma_z (\approx 0.078)$. The range chosen range $\Delta_z = 0.1$ thus covers ≈ 90% of the cluster galaxies. The angular cluster size in the simulation has been set to $r_{cut} = 5 \times R_{200}$. The cutoff radius however, impacts the shape and the normalization of the Plummer-profile. The amount of galaxies for the Plummer profile will thus be different from that of a NFW profile. In both cases most galaxies will be located in a circle of radius $r = 2 \times R_{200}$ though. Table 16 summarizes the purity and completeness rates achieved by correlating detections and clusters within the tube. The filter size $r_{cut} = 5 \times R_{200}$ has been taken very large considering its mass $M_{fil} = 5 \times 10^{14} M_\odot$. It means that the convolution length

---

[1] http://www.astromatic.net/software/sextractor

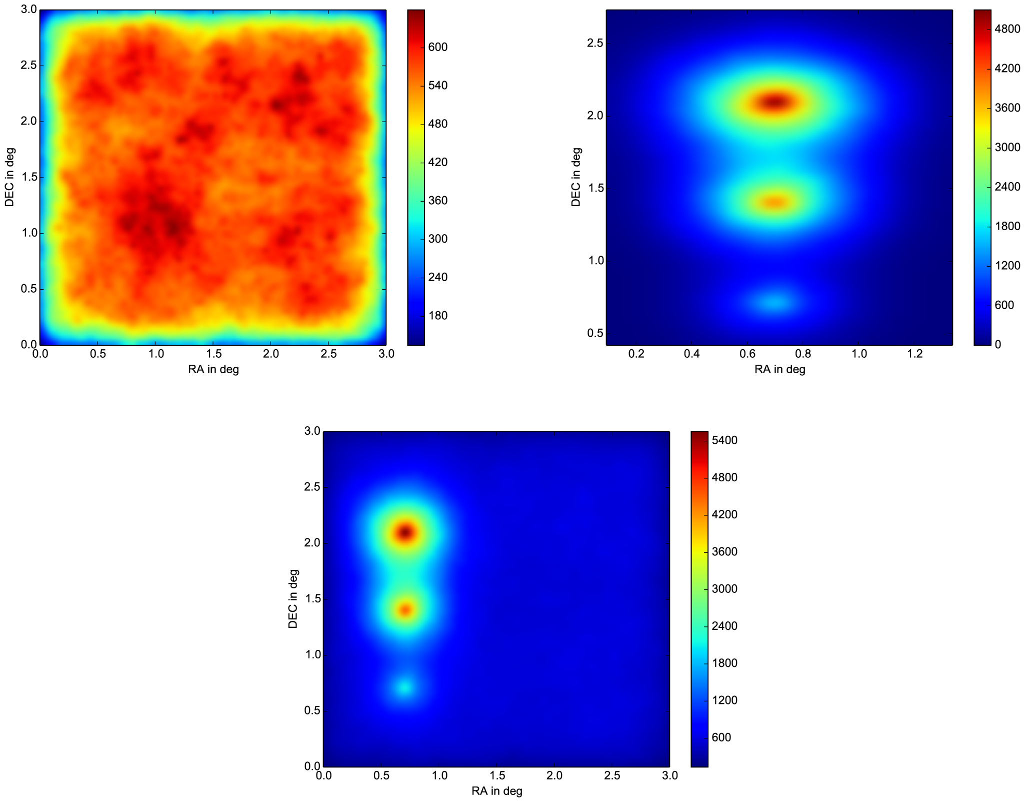

Figure 31: Result of filter in r and g bands applied to field galaxies only (top left), cluster galaxies only (top right) and combination of both (bottom).

is very large, such that many peaks are smoothed out by the filter. The completeness rates are not as expected. Increasing the tube diameter increases the completeness rate as expected, but a correlation length of $5 \times R_{200}$ is unrealistically large.

The Plummer profile has a big impact on the simulation. Because it has some contribution from the profile tail, cluster signals will overlap stronger than for a NFW profile. Therefore the simulation is additionally performed and evaluated for another profile with a smaller cutoff radius. The profile as mentioned in Section 3.4 is taken from Sheldon et al. (2009). This simulation and application run are labeled Sheldon-run. The cluster cutoff in the simulation is set to $r_{\text{cut},2} = 2 \times R_{200}$. The filter size has been reset to $r_{\text{cut}} = 1 \times R_{200}$ using the same cluster model mass as in the Plummer-run. The smaller smoothing length leads to an increase the amount of detections. For the two fixed SN thresholds the purity rate of the Sheldon-run in comparison to the large cutoff Plummer-run decreases to less than 70%. In turn the completeness rate increases to 99% in both 3 and 5 SN threshold cases. The equivalent purity rate in both runs can be achieved by setting the SN threshold in the Sheldon-run to 12. The completeness for these selection reaches 94%.

Table 16: Results from the *RedMagCol* filter application to simulation from the mass–function in the Plummer-run. For two SN thresholds (3 & 5) the number of detections and clusters are show in the first two columns. The purity column stands for all detections that could be related to clusters. The association with clusters takes place by introducing a tube with diameter of $2 \times R_{200}$ and length $[0.1 - z : z + 0.1]$. The parameter R_{200} and z are the characteristics of the detection, specifically of the model cluster used for the detection. Completeness is the number of clusters that could be related to detections. The lowest cluster mass in the simulation is $5 \times 10^{13} M_{\odot}$, the field of view is 9 deg^2 in a redshift range from 0.1 to 1.

	Detections	Clusters	Purity	Completeness
SN – 3	726	409	611 (84.2 %)	244 (59.7 %)
SN – 5	719	409	611 (85.0 %)	244 (59.7 %)

Table 17: Results from the *RedMagCol* filter application to simulation from the mass–function in the Sheldon-run. For two SN thresholds (3 & 5) the number of detections and clusters are show in the first two columns. The purity column stands for all detections that could be related to clusters. The association with clusters takes place by introducing a tube with diameter of $2 \times R_{200}$ and length $[0.1 - z : z + 0.1]$. The parameter R_{200} and z are the characteristics of the detection, specifically of the model cluster used for the detection. Completeness is the number of clusters that could be related to detections. The lowest cluster mass in the simulation is $5 \times 10^{13} M_{\odot}$, the field of view is 9 deg^2 in a redshift range from 0.1 to 1.

	Detections	Clusters	Purity	Completeness
SN – 3	2251	409	1387 (61.6 %)	405 (99.0 %)
SN – 5	1977	409	1374 (69.5 %)	405 (99.0 %)
SN – 12	1295	409	1120 (86.5 %)	388 (94.9 %)

From the application to the grid simulation can be inferred that the filter performs as it should on known distributions, especially when present clusters do not overlap. In particular, the filter predicts the richness accurately within the estimated error. Also the background and variance of the field are predicted correctly. Further can be inferred that the contamination rate for SN above 5 is slightly below 2 deg^{-2}.

The application to simulations based on the mass–function showed that the simulations have to be carried out very carefully. If the profile tails contributes strongly to the amount of cluster galaxies can a too big size of the cluster account for too many overlaps in the field. This results in either too many spurious detections or high incompleteness. The incompleteness results from the definition of an angular correlation length, which must be too large for clusters with flat profile tails.

Using smaller convolution scale in the filter $\kappa_r = 1$, results in more detections that are recognized by SExtractor. As clusters are dense objects witch characteristically steep profiles one should focus on the inner significant region. Because mass relates to R_{200}, a model cluster with fixed mass of $10^{14}\ M_\odot$ shall be considered.

Although it has not been tested, but the same should also apply for the redshift. Such that filter model with $\kappa = 1, 1, 2$ might be tested.

9

APPLICATION OF FILTER TO CARS W1M0P1 FIELD

9.1 APPLICATION

The application to the CARS data requires a special treatment. Because many regions are masked due to bright stars and resulting CCD saturation, it becomes difficult to achieve the proper number density for the field galaxy distribution in the first place. Secondly, the masked regions lower the background term from Equation 38 and increases the variance from Equation 45 in the field. Also the cluster density, measured in clusters $\mathrm{deg}^{-}2$ will be wrong, if not subtracting masked regions from the field size.

To estimate the angular number density correctly, the angular data is divided into pixels and convolved with a Gaussian filter which width is proportional to the mean average separation. Pixels with smaller number density than a defined threshold are masked by assigning the value zero to the pixel. The effective coverage is estimated from the area that has non zero density. Not only does this approach provide a good estimate of the actual number density within the irregular field, it also provides information about the mask regions. In the filter application, the signal estimate can hence be corrected for the masks in terms of coverage correction. The coverage correction term is estimated similar to the approach by Rykoff et al. (2014). Here the angular part of the filter is used to estimate the mask fraction at the specific cluster location. To do so, two integrals are performed using Monte-Carlo integration. The first computes the total radial filter integral in the filter defined region. The second integral is computed in the same region which is also not masked. This is technically achieved by multiplying the spatial filter function $\Phi(\vec{x})$ with a function $S(\vec{x})$ that is zero if $\vec{x} \in A_{\mathrm{mask}}$. The coverage correction is $f_{cc} = \frac{f_{in}}{f_{tot}}$. The biased signal strength estimate Λ^{b}_{est} can therefore be corrected for the mask and biasing factor. This yields the unbiased estimate according to Equation 34:

$$\Lambda^{corr}_{est} = \Lambda^{b}_{est} \cdot f^{-1}_{cc} - \bar{B}. \tag{54}$$

According to predictions from mass–function as computed during simulations (see Ch. 6) in a 1 deg^2 the expected number of clusters with mass exceeding $5 \times M_\odot$ in the redshift range between 0.1 and 1 are 45.44. Because the W1m0p1 field is not entirely covered, as computed by the algorithm only 82% of its area are usable. This reduces the expected number to 37.2. Because contamination will be at least as estimated in Section 8.1 the expected number of detections with $SN > 3$ is 50.56. In addition multiple detections of the same object are expected such that the number of detections anticipated to exceed 50.

The *RedMagCol* filter is applied to the W1m0p1 catalog in the redshift range from 0.1 to 1. The slicing in redshift has been performed with $dz = 0.05$. The filter limits have been adjusted to $\kappa_r = 1, \kappa_z = 2, \kappa_c = 5$ and a mass of $5 \times 10^{13} M_\odot$ chosen. The filter has been applied using the coverage correction term as explained above. The pixel size has been adopted to a third of the FWHL of the angular filter profile.

To the resulting maps SExtractor has been applied. It produced a catalog of 59 detections with SN above 3 and 7 detections with SN above 5. This number agrees well with predictions from the mass–function as stated above. To remove multiple detections of the same object, a merging procedure is applied. In principle it is very similar to the procedure of correlating detections to clusters from the simulation that is explained in the previous Chapter. The tube is chosen to be $[0.1 - z : z + 0.1]$ in redshift and R_{200} in angular space. After applying the reduction procedure 31 detections remain. Four of these reduced candidate detections are shown in Figure 32.

Figure 32: Randomly chosen detection candidates from W1m0p1 CARS field run. Top left: at RA=34.8952, DEC=-5.61616 and z=0.4. Top right: at RA=34.6486, DEC=-5.66582 and z=0.45. Bottom left: at RA=34.6827, DEC=-5.9755 and z=0.5. Bottom right: at RA=34.9125, DEC=-6.38604 and z=0.55.

In Adami et al. (2010) (hereafter, ADAMI) the filter function from Mazure et al. (2007) has been applied to the deep and wide fields of CARS. In particular catalogs for each patch (see Sec. 2) have been released. Here the patch W1m0p1 is investigated. ADAMI propose 36 detections with redshifts ranging from 0.4 to 1.1. The merging procedure from previous Chapter is applied to find matches within both catalogs. 15 of the above 31 reduced detections from the present approach find matches in ADAMI sample. However, only 8 detections from ADAMI can be related to detections from the present optimal match filter run. The mismatch is not surprising, as no scales for the detections in ADAMI have been provided, also no richness estimates. Nevertheless has the test of application of the optimal matched filter succeeded on real data.

Part III

SUMMARY AND CONCLUSIONS

The construction of the optimal matched filter in optical bands required a signal model and a model for the statistics of noise in the data. The signal model scales with mass and redshift of the cluster's host halo and depends on bands in which the observation is made. The noise statistics have been considered Poissonian and two models have been introduced. The first noise model assumes a priori a multi–variate Gaussian distribution of galaxies in the optical observables. The second noise model estimates the field galaxy distribution from the data directly. Both models for the field galaxy distribution assume isotropy of field galaxies. It has been tested that deviations from the estimated density are tolerable based on a χ^2 test. The filter template based on two arbitrary signal and noise models has been introduced and implemented with seven possible distribution functions based on the combination of optical observables in the survey. These seven filters have been tested by investigating the impact of the input signal (cluster galaxies) and noise (field galaxies) model densities on the resulting filter distribution maps. First, the test has been performed with the a priori known field galaxy distribution (MVG). The filters behaved as expected from the cluster and field galaxy distribution maps. Subsequently,s expectation values for the signal-to- noise ratios on a mass-redshift grid have been computed. These maps gave insight into selection functions of each individual filter, especially because the underlying field galaxy distribution is known exactly. For example does the signal-to-noise ratio for the redshift only filter drop in the region where the field galaxy distribution is highest. This means that the a priori known field galaxy distribution impacts the selection function in a qualitatively clear way. The signal-to-noise maps have also been computed for the selected W1m0p1 field in the CARS data. On the redshift-mass grid for the signal-to-noise ratios also a mass–function has been evaluated. Specifically a number of dark–matter halos has been computed in each grid cell. By setting the detection thresholds in signal-to-noise ratio to 3 or 5 enables to predict the expected number of detections in each grid cell. The quantitative evaluation of this prediction favored the combination of the RedMagCol filter. In the last the predicted detection numbers have been tested against simulations. For this purpose a test field of 3×3 deg^2 in size has been constructed. Random number tuples of mass and redshift have been drawn from the mass–function. These tuples represent Dark–matter halos which have been placed randomly into this field. On top of each of these dark–matter halos a galaxy cluster is placed. This means that the expected number of galaxies from that halo is distributed around its center (also in redshift, magnitude and color) based on the cluster galaxy density model for that mass and redshift. Field galaxies have been draw from a MVG and placed randomly in the field. In the simulation there is a clear distinction between cluster and field galaxies. This circumstance is used to compute the expected contamination in the field by applying the chosen filter to the catalog including field galaxies only. The number of false–positive detections is 147 and 15 in the 9 deg^2 field for signal-to-noise thresholds of 3 and 5 respectively. It has been further confirmed that the predicted background and variance in the field agrees with the measured values. The filter has been subsequently applied to the clusters on the grid simulation in which cluster and field galaxies are both present. The clusters are placed in such a distance that there is no overlap between them. The filter is confirmed to measure the right richnesses within the 1–σ errors predicted by the filter. After these basic tests, the filter has been applied to the simulation of galaxy clusters distributed according to the mass–function in the 9 deg^2 field. Because of the peculiarity in the simulation, namely the usage of the Plummer profile with a big cutoff radius for the simulated clusters resulted in big overlaps outside of the central region of clusters. Thereupon a new simulation has been set up to investigate the impact of a too big cutoff scale in the cluster profile. The smaller cutoff in the simulation and the usage of Sheldon profile increased both the purity and the completeness rates. All tests agreed with the expectation. After this findings the filter has been tested on the W1m0p1 field of CARS. It passed the test as for 31 reduced detections 15 could be related to detections from literature.

The conclusion is that the construction of an optimal matched filter which works on optical data succeeded. Its properties in terms of distribution functions and their impact on the resulting weighting function have been investigated and could be comprehended. For any field and combination of observables detectability signal-to-noise predictions can be made with the filter function. It has been verified through simulations that these predictions are trustworthy. After a heuristic analysis of detections in the W1m0p1 CARS field can be confirmed that the filter can already be applied to data.

The following aspects need to be considered, however, when either predictions are made or the filter is applied:

- The cluster extents in terms of the κ values need to be chosen carefully. Especially it can be investigated what the best choice based on simulation is.
- The selection of detections need to be further investigated. In paricular the extraction of over density regions in the richness maps and probable deblending need to be investigated.
- The relation from estimated richness to the halo mass needs to be comprehended. The impact on the signal estimate biasing due to fixed filter mass usage needs to be further examined.
- Galaxy completeness for the limiting magnitude (in the observed band) in the data must be guaranteed in order to not bias the cluster signal estimation. This also holds for predictions from the mass–function.
- In angular space, the borders and masks challenge the signal estimation. When operating with data that contains masked regions a correction to the signal estimate needs to be applied. For CFHTLS masks can be directly read in from FITS files.
- In CARS the photo-z's are biased in respect to spectroscopic sub samples. In CFHTLenS[1] this bias has been removed and the photometric redshift estimation has been improved.

---

[1] http://www.cfhtlens.org/

BIBLIOGRAPHY

G. O. Abell, H. G. Corwin, Jr., and R. P. Olowin. A catalog of rich clusters of galaxies. *ApJ Suppl. Ser.*, 70:1–138, May 1989. doi: 10.1086/191333.

C. Adami, F. Durret, C. Benoist, J. Coupon, A. Mazure, B. Meneux, O. Ilbert, J. Blaizot, S. Arnouts, A. Cappi, B. Garilli, L. Guennou, V. Lebrun, O. Lefèvre, S. Maurogordato, H. J. McCracken, Y. Mellier, E. Slezak, L. Tresse, and M. P. Ulmer. Galaxy structure searches by photometric redshifts in the CFHTLS. *A&A*, 509:A81, January 2010. doi: 10.1051/0004-6361/200913067.

C. Angrick and M. Bartelmann. Triaxial collapse and virialisation of dark-matter haloes. *A&A*, 518:A38, July 2010. doi: 10.1051/0004-6361/201014147.

B. Ascaso, D. Wittman, and N. Benítez. Bayesian cluster finder: clusters in the CFHTLS Archive Research Survey. *MNRAS*, 420:1167–1182, February 2012. doi: 10.1111/j.1365-2966.2011.20107.x.

H. Babcock. The rotation of the andromeda nebula. *Lick Observatory bulletin*, 498, 1939.

M. L. Balogh, I. K. Baldry, R. Nichol, C. Miller, R. Bower, and K. Glazebrook. The Bimodal Galaxy Color Distribution: Dependence on Luminosity and Environment. *ApJ Letters*, 615:L101–L104, November 2004. doi: 10.1086/426079.

M. Bartelmann. Arcs from a universal dark-matter halo profile. *A&A*, 313:697–702, September 1996.

F. Bellagamba, M. Maturi, T. Hamana, M. Meneghetti, S. Miyazaki, and L. Moscardini. Optimal filtering of optical and weak lensing data to search for galaxy clusters: application to the COSMOS field. *MNRAS*, 413:1145–1157, May 2011. doi: 10.1111/j.1365-2966.2011.18202.x.

Fabio Bellagamba. *Testing future weak lensing surveys through simulations of observations*. PhD thesis, UniversitÃ di Bologna, 2012. URL `http://amsdottorato.unibo.it/4762/`.

N. Benítez. Bayesian Photometric Redshift Estimation. *ApJ*, 536:571–583, June 2000. doi: 10.1086/308947.

E. Bertin and S. Arnouts. SExtractor: Software for source extraction. *A&A Supplement*, 117:393–404, June 1996. URL `http://www.astromatic.net/software/sextractor`.

G. Bruzual and S. Charlot. Stellar population synthesis at the resolution of 2003. *MNRAS*, 344:1000–1028, October 2003. doi: 10.1046/j.1365-8711.2003.06897.x.

H. Butcher and A. Oemler, Jr. The evolution of galaxies in clusters. I - ISIT photometry of C1 0024+1654 and 3C 295. *ApJ*, 219:18–30, January 1978. doi: 10.1086/155751.

G. D. Coleman, C.-C. Wu, and D. W. Weedman. Colors and magnitudes predicted for high redshift galaxies. *ApJ Suppl. Ser.*, 43:393–416, July 1980. doi: 10.1086/190674.

F. Dong, E. Pierpaoli, J. E. Gunn, and R. H. Wechsler. Optical Cluster Finding with an Adaptive Matched-Filter Technique: Algorithm and Comparison with Simulations. *ApJ*, 676:868–879, April 2008. doi: 10.1086/522490.

A. Dressler. Galaxy morphology in rich clusters - Implications for the formation and evolution of galaxies. *ApJ*, 236:351–365, March 1980. doi: 10.1086/157753.

A. Einstein. Die Grundlage der allgemeinen Relativitätstheorie. *Annalen der Physik*, 354: 769–822, 1916. doi: 10.1002/andp.19163540702.

P. R. M. Eisenhardt, M. Brodwin, A. H. Gonzalez, S. A. Stanford, D. Stern, P. Barmby, M. J. I. Brown, K. Dawson, A. Dey, M. Doi, A. Galametz, B. T. Jannuzi, C. S. Kochanek, J. Meyers, T. Morokuma, and L. A. Moustakas. Clusters of Galaxies in the First Half of the Universe from the IRAC Shallow Survey. *ApJ*, 684:905–932, September 2008. doi: 10.1086/590105.

T. Erben, H. Hildebrandt, M. Lerchster, P. Hudelot, J. Benjamin, L. van Waerbeke, T. Schrabback, F. Brimioulle, O. Cordes, J. P. Dietrich, K. Holhjem, M. Schirmer, and P. Schneider. CARS: the CFHTLS-Archive-Research Survey. I. Five-band multi-colour data from 37 sq. deg. CFHTLS-wide observations. *A&A*, 493:1197–1222, January 2009. doi: 10.1051/0004-6361:200810426.

D. J. Fixsen. The Temperature of the Cosmic Microwave Background. *ApJ*, 707:916–920, December 2009. doi: 10.1088/0004-637X/707/2/916.

A. Friedmann. Über die Krümmung des Raumes. *Zeitschrift fur Physik*, 10:377–386, 1922. doi: 10.1007/BF01332580.

A. Friedmann. Über die Möglichkeit einer Welt mit konstanter negativer Krümmung des Raumes. *Zeitschrift fur Physik*, 21:326–332, December 1924. doi: 10.1007/BF01328280.

R. R. Gal. Optical Detection of Clusters of Galaxies. In M. Plionis, O. López-Cruz, and D. Hughes, editors, *A Pan-Chromatic View of Clusters of Galaxies and the Large-Scale Structure*, volume 740 of *Lecture Notes in Physics, Berlin Springer Verlag*, page 119, 2008. doi: 10.1007/978-1-4020-6941-3_4.

G. Gamow. *The creation of the universe*. Viking Press, Inc. New York, 1952.

Alexander Gelsin. A multiband approach to detect clusters of galaxies. Master's thesis, Faculty for Physics and Astronomy, at Ruprecht-Karls-University of Heidelberg, Institute for Theoretical Astrophysics, Center for Astronomie (ZAH), November 2011.

M. D. Gladders and H. K. C. Yee. A New Method For Galaxy Cluster Detection. I. The Algorithm. *AJ*, 120:2148–2162, October 2000. doi: 10.1086/301557.

T. Goto, M. Sekiguchi, R. C. Nichol, N. A. Bahcall, R. S. J. Kim, J. Annis, Ž. Ivezić, J. Brinkmann, G. S. Hennessy, G. P. Szokoly, and D. L. Tucker. The Cut-and-Enhance Method: Selecting Clusters of Galaxies from the Sloan Digital Sky Survey Commissioning Data. *AJ*, 123:1807–1825, April 2002. doi: 10.1086/339303.

S. M. Hansen, E. S. Sheldon, R. H. Wechsler, and B. P. Koester. The Galaxy Content of SDSS Clusters and Groups. *ApJ*, 699:1333–1353, July 2009. doi: 10.1088/0004-637X/699/2/1333.

J. Hao. Optical galaxy cluster detection across a wide redshift range. 2009.

J. Hao, T. A. McKay, B. P. Koester, E. S. Rykoff, E. Rozo, J. Annis, R. H. Wechsler, A. Evrard, S. R. Siegel, M. Becker, M. Busha, D. Gerdes, D. E. Johnston, and E. Sheldon. A GMBCG Galaxy Cluster Catalog of 55,424 Rich Clusters from SDSS DR7. *ApJ Suppl. Ser.*, 191:254–274, December 2010. doi: 10.1088/0067-0049/191/2/254.

A. P. Hearin, A. R. Zentner, J. A. Newman, and A. A. Berlind. Mind the gap: tightening the mass-richness relation with magnitude gaps. *MNRAS*, 430:1238–1246, April 2013. doi: 10.1093/mnras/sts699.

H. Hildebrandt, T. Erben, K. Kuijken, L. van Waerbeke, C. Heymans, J. Coupon, J. Benjamin, Bonnett, and et al. . CFHTLenS: improving the quality of photometric redshifts with precision photometry. *MNRAS*, 421:2355–2367, April 2012. doi: 10.1111/j.1365-2966.2012.20468.x.

G. Hinshaw, D. Larson, E. Komatsu, D. N. Spergel, C. L. Bennett, J. Dunkley, M. R. Nolta, M. Halpern, R. S. Hill, N. Odegard, L. Page, K. M. Smith, J. L. Weiland, B. Gold, N. Jarosik, A. Kogut, M. Limon, S. S. Meyer, G. S. Tucker, E. Wollack, and E. L. Wright. Nine-year Wilkinson Microwave Anisotropy Probe (WMAP) Observations: Cosmological Parameter Results. *ApJ Suppl. Ser.*, 208:19, October 2013. doi: 10.1088/0067-0049/208/2/19.

D. W. Hogg. Data analysis recipes: Choosing the binning for a histogram. *ArXiv e-prints*, July 2008.

D. W. Hogg, D. J. Eisenstein, M. R. Blanton, N. A. Bahcall, J. Brinkmann, J. E. Gunn, and D. P. Schneider. Cosmic Homogeneity Demonstrated with Luminous Red Galaxies. *ApJ*, 624:54–58, May 2005. doi: 10.1086/429084.

E. Hubble. A Relation between Distance and Radial Velocity among Extra-Galactic Nebulae. *Proceedings of the National Academy of Science*, 15:168–173, March 1929. doi: 10.1073/pnas.15.3.168.

A. Jenkins, C. S. Frenk, S. D. M. White, J. M. Colberg, S. Cole, A. E. Evrard, H. M. P. Couchman, and N. Yoshida. The mass function of dark matter haloes. *MNRAS*, 321: 372–384, February 2001. doi: 10.1046/j.1365-8711.2001.04029.x.

A. L. Kinney, D. Calzetti, R. C. Bohlin, K. McQuade, T. Storchi-Bergmann, and H. R. Schmitt. Template Ultraviolet to Near-Infrared Spectra of Star-forming Galaxies and Their Application to K-Corrections. *ApJ*, 467:38, August 1996. doi: 10.1086/177583.

B. P. Koester, T. A. McKay, J. Annis, R. H. Wechsler, A. Evrard, L. Bleem, M. Becker, D. Johnston, E. Sheldon, R. Nichol, C. Miller, R. Scranton, N. Bahcall, J. Barentine, H. Brewington, J. Brinkmann, M. Harvanek, S. Kleinman, J. Krzesinski, D. Long, A. Nitta, D. P. Schneider, S. Sneddin, W. Voges, and D. York. A MaxBCG Catalog of 13,823 Galaxy Clusters from the Sloan Digital Sky Survey. *ApJ*, 660:239–255, May 2007a. doi: 10.1086/509599.

B. P. Koester, T. A. McKay, J. Annis, R. H. Wechsler, A. E. Evrard, E. Rozo, L. Bleem, E. S. Sheldon, and D. Johnston. MaxBCG: A Red-Sequence Galaxy Cluster Finder. *ApJ*, 660: 221–238, May 2007b. doi: 10.1086/512092.

E. Komatsu, K. M. Smith, J. Dunkley, C. L. Bennett, B. Gold, G. Hinshaw, N. Jarosik, and et al. Seven-year Wilkinson Microwave Anisotropy Probe (WMAP) Observations: Cosmological Interpretation. *ApJ Suppl. Ser.*, 192:18, February 2011. doi: 10.1088/0067-0049/192/2/18.

G. Lemaître. Un Univers homogène de masse constante et de rayon croissant rendant compte de la vitesse radiale des nébuleuses extra-galactiques. *Annales de la Société Scientifique de Bruxelles*, 47:49–59, 1927.

Y.-S. Loh, E. Ellingson, H. K. C. Yee, D. G. Gilbank, M. D. Gladders, and L. F. Barrientos. The Color Bimodality in Galaxy Clusters since z ˜ 0.9. *ApJ*, 680:214–223, June 2008. doi: 10.1086/587830.

M. Maturi, M. Meneghetti, M. Bartelmann, K. Dolag, and L. Moscardini. An optimal filter for the detection of galaxy clusters through weak lensing. *A& A*, 442:851–860, November 2005. doi: 10.1051/0004-6361:20042600.

A. Mazure, C. Adami, M. Pierre, O. Le Fèvre, S. Arnouts, P. A. Duc, O. Ilbert, V. Lebrun, B. Meneux, F. Pacaud, J. Surdej, and I. Valtchanov. Structure detection in the D1 CFHTLS deep field using accurate photometric redshifts: a benchmark. *A&A*, 467: 49–62, May 2007. doi: 10.1051/0004-6361:20066379.

J. F. Navarro, C. S. Frenk, and S. D. M. White. The Structure of Cold Dark Matter Halos. *ApJ*, 462:563, May 1996. doi: 10.1086/177173.

M. Oguri. A cluster finding algorithm based on the multiband identification of red sequence galaxies. *ArXiv e-prints*, July 2014.

F. Pace, M. Maturi, M. Bartelmann, N. Cappelluti, K. Dolag, M. Meneghetti, and L. Moscardini. Statistical properties of SZ and X-ray cluster detections. *A& A*, 483:389–400, May 2008. doi: 10.1051/0004-6361:200809550.

P. J. Peebles and B. Ratra. The cosmological constant and dark energy. *Reviews of Modern Physics*, 75:559–606, April 2003. doi: 10.1103/RevModPhys.75.559.

A. A. Penzias and R. W. Wilson. A Measurement of Excess Antenna Temperature at 4080 Mc/s. *ApJ*, 142:419–421, July 1965. doi: 10.1086/148307.

Planck Collaboration, P. A. R. Ade, N. Aghanim, C. Armitage-Caplan, M. Arnaud, M. Ashdown, F. Atrio-Barandela, J. Aumont, C. Baccigalupi, A. J. Banday, and et al. Planck 2013 results. XVI. Cosmological parameters. *A&A*, 571:A16, November 2014. doi: 10.1051/0004-6361/201321591.

H. C. Plummer. On the problem of distribution in globular star clusters. *MNRAS*, 71: 460–470, March 1911.

M. Postman, L. M. Lubin, J. E. Gunn, J. B. Oke, J. G. Hoessel, D. P. Schneider, and J. A. Christensen. The Palomar Distant Clusters Survey. I. The Cluster Catalog. *AJ*, 111:615, February 1996. doi: 10.1086/117811.

W. H. Press and P. Schechter. Formation of Galaxies and Clusters of Galaxies by Self-Similar Gravitational Condensation. *ApJ*, 187:425–438, February 1974. doi: 10.1086/152650.

M. Redlich, K. Bolejko, S. Meyer, G. F. Lewis, and M. Bartelmann. Probing spatial homogeneity with LTB models: a detailed discussion. *A&A*, 570:A63, October 2014. doi: 10.1051/0004-6361/201424553.

A. G. Riess, A. V. Filippenko, P. Challis, A. Clocchiatti, A. Diercks, P. M. Garnavich, R. L. Gilliland, C. J. Hogan, S. Jha, R. P. Kirshner, B. Leibundgut, M. M. Phillips, D. Reiss, B. P. Schmidt, R. A. Schommer, R. C. Smith, J. Spyromilio, C. Stubbs, N. B. Suntzeff, and J. Tonry. Observational Evidence from Supernovae for an Accelerating Universe and a Cosmological Constant. *AJ*, 116:1009–1038, September 1998. doi: 10.1086/300499.

H. P. Robertson. Kinematics and World-Structure. *ApJ*, 82:284, November 1935. doi: 10.1086/143681.

E. Rozo, E. S. Rykoff, B. P. Koester, T. McKay, J. Hao, A. Evrard, R. H. Wechsler, S. Hansen, E. Sheldon, D. Johnston, M. Becker, J. Annis, L. Bleem, and R. Scranton. Improvement of the Richness Estimates of maxBCG Clusters. *ApJ*, 703:601–613, September 2009. doi: 10.1088/0004-637X/703/1/601.

E. Rozo, E. Rykoff, B. Koester, B. Nord, H.-Y. Wu, A. Evrard, and R. Wechsler. Extrinsic Sources of Scatter in the Richness-mass Relation of Galaxy Clusters. *ApJ*, 740:53, October 2011. doi: 10.1088/0004-637X/740/2/53.

E. S. Rykoff, B. P. Koester, E. Rozo, J. Annis, A. E. Evrard, S. M. Hansen, J. Hao, D. E. Johnston, T. A. McKay, and R. H. Wechsler. Robust Optical Richness Estimation with Reduced Scatter. *ApJ*, 746:178, February 2012. doi: 10.1088/0004-637X/746/2/178.

E. S. Rykoff, E. Rozo, M. T. Busha, C. E. Cunha, A. Finoguenov, A. Evrard, J. Hao, B. P. Koester, A. Leauthaud, B. Nord, M. Pierre, R. Reddick, T. Sadibekova, E. S. Sheldon, and R. H. Wechsler. redMaPPer. I. Algorithm and SDSS DR8 Catalog. *ApJ*, 785:104, April 2014. doi: 10.1088/0004-637X/785/2/104.

P. Schechter. An analytic expression for the luminosity function for galaxies. *ApJ*, 203: 297–306, January 1976. doi: 10.1086/154079.

M. I. Scrimgeour, T. Davis, C. Blake, J. B. James, G. B. Poole, L. Staveley-Smith, S. Brough, M. Colless, C. Contreras, W. Couch, S. Croom, D. Croton, M. J. Drinkwater, K. Forster, D. Gilbank, M. Gladders, K. Glazebrook, B. Jelliffe, R. J. Jurek, I.-h. Li, B. Madore, D. C. Martin, K. Pimbblet, M. Pracy, R. Sharp, E. Wisnioski, D. Woods, T. K. Wyder, and H. K. C. Yee. The WiggleZ Dark Energy Survey: the transition to large-scale cosmic homogeneity. *MNRAS*, 425:116–134, September 2012. doi: 10.1111/j.1365-2966.2012.21402.x.

E. S. Sheldon, D. E. Johnston, M. Masjedi, T. A. McKay, M. R. Blanton, R. Scranton, R. H. Wechsler, B. P. Koester, S. M. Hansen, J. A. Frieman, and J. Annis. Cross-correlation Weak Lensing of SDSS Galaxy Clusters. III. Mass-to-Light Ratios. *ApJ*, 703:2232–2248, October 2009. doi: 10.1088/0004-637X/703/2/2232.

R. K. Sheth and G. Tormen. Large-scale bias and the peak background split. *MNRAS*, 308:119–126, September 1999. doi: 10.1046/j.1365-8711.1999.02692.x.

V. M. Slipher. The Lowell Observatory. *Publications of the Astronomical Society of the Pacific*, 39:143, April 1927. doi: 10.1086/123696.

R. A. Sunyaev and I. B. Zeldovich. Intergalactic gas in clusters of galaxies, the microwave background, and cosmology. *Astrophysics and Space Physics Reviews*, 1:1–60, 1981.

J. Tinker, A. V. Kravtsov, A. Klypin, K. Abazajian, M. Warren, G. Yepes, S. Gottlöber, and D. E. Holz. Toward a Halo Mass Function for Precision Cosmology: The Limits of Universality. *ApJ*, 688:709–728, December 2008. doi: 10.1086/591439.

A. G. Walker. On milne's theory of world-structure. *Proceedings of the London Mathematical Society*, s2-42(1):90–127, 1937. doi: 10.1112/plms/s2-42.1.90. URL `http://plms.oxfordjournals.org/content/s2-42/1/90.short`.

Fred J Williams, Arthur B & Taylor. *Electronic Filter Design Handbook.* McGraw-Hill., 1995.

F. Zwicky. Die Rotverschiebung von extragalaktischen Nebeln. *Helvetica Physica Acta*, 6: 110–127, 1933.

ACKNOWLEDGMENTS

During my studies I have been kindly hosted in a idyllic place called Northeim. Its population is fluctuating but the silly jokes are constant. Without this shelter any work would have been more difficult and gray. I want to thank Christan the mayor of Northeim for being inspiring and helpful throughout my stay. Also, I want to thank Matthias R. and Björn M.S. who were not less helpful and inspiring and sometimes even as funny as the mayor. In the last months of the PhD project I have been also kindly hosted by Maren and Kris. I appreciate their company and help very much. I also enjoyed every moment with my goddaughter Mila who although very small imprinted a huge smile on my face every time I saw her. It was and is a lot of fun being part of the MB research group. Even if times are hard its support is guaranteed. I therefore want to thank the whole group. In particular I want to thank all encouragement and support during my stay at the hospital. People who you can always rely on are rare, but the over density of them within this group is significant. I want to thank Matteo who supervised me during the project. Besides discussions on the topic, also climbing and skiing with you and Jelena was a lot of fun. I am very grateful to my parents who support me in all situations as much as they can. I want also to thank my sister who probably does not even know how much she taught me in live. I am really grateful to my fiancee Romy, for all the adventures that we already had and will have in future. Finally I want to thank Matthias B. Without him many of the experiences during the last years would not have been made. I thank him very much for the big opportunity, for his support and inspiration.

COLOPHON

This document was typeset using the typographical look-and-feel `classicthesis` developed by André Miede. The style was inspired by Robert Bringhurst's seminal book on typography *"The Elements of Typographic Style"*. `classicthesis` is available for both LaTeX and LyX:

http://code.google.com/p/classicthesis/

Final Version as of 30th March 2015 (`classicthesis` version 4.1).